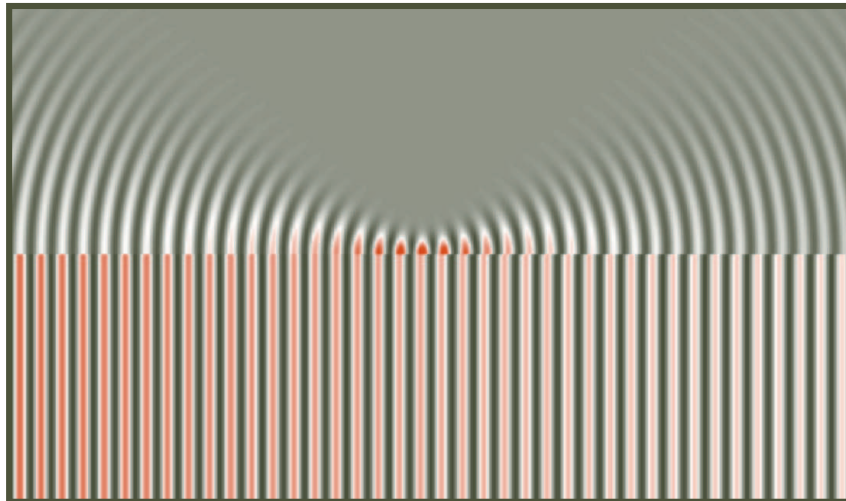# Investigation of plasmonic structures for use as sensors and signal processing devices

Tobias Birr

Investigation of plasmonic structures for use as sensors and signal processing devices

Von der Fakultät für Mathematik und Physik
der Gottfried Wilhelm Leibniz Universität Hannover
zur Erlangung des akademischen Grades

Doktor der Naturwissenschaften
- Dr. rer. nat. -

genehmigte Dissertation
von

Tobias Birr

Master of Science in Technischer Physik
geboren am 10.10.1986 in Hamburg

2017

Referent: Prof. Dr. Carsten Reinhardt
Korreferent: Prof. Dr. Boris N. Chichkov
Tag der Disputation: 01. Juni 2017

Kurzzusammenfassung

In der modernen Technologielandschaft bietet Licht ein mannigfaltiges Anwendungsspektrum. Es verspricht unter Anderem optische Datenverarbeitung und einen neuen Grad an Präzision für Datendetektierende oder Strukturenproduzierende Geräte. Ein kritischer Gesichtspunkt ist hierbei, wie in vielen anderen industriellen Sparten, die Miniaturisierung. In diesem Aspekt liefert diese Doktorarbeit die Untersuchung von Oberflächen Plasmon-Polaritonen (OPP) zur Nutzung in Sensoranwendungen, als auch dem Datentransport in Wellenleitern und der Datenprozessierung in plasmonischen Logikgattern mit Dimensionen im Mikrometerbereich. Die Sensoranwendung sowie die plasmonischen Strukturen sind dabei im selben experimentellen System verordnet.

Zur Untersuchung der OPP wurde ein Leckstrahlungsmikroskop genutzt, welches dahingehend erweitert wurde, dass es die Möglichkeit von phasen- und zeitaufgelösten Messungen von propagierenden OPP bietet. Weiterhin konnte damit die optische Fourier Transformation des untersuchten Systems direkt aufgezeichnet werden, um Änderungen der Propagationseigenschaften der OPPs direkt messen zu können. Dies wurde im Theoretischen durch die Nutzung der Transfermatrixmethode und direkten zeit- und phasenaufgelösten Berechnungen des elektrischen Feldes der OPP unterstützt. Für die Herstellung der untersuchten Strukturen war diese Arbeit an der Entwicklung einer neuartigen, schnellen und flexiblen Lithographiemethode im low-cost Bereich beteiligt.

Die Arbeit untersucht zunächst die Variation der Phase von propagierenden OPP durch eine Änderung des umgebenden Mediums, als auch einer intrinsischen Phasenänderung durch den Gouy-Phase-Shift, auftretend beim Fokussieren von OPP. Dabei enthält diese Arbeit die erste experimentelle Demonstration eines zweidimensionalen Gouy-Phase-Shifts für optische Wellenlängen. Weiterhin untersucht diese Arbeit die Möglichkeit das plasmonische Analogon eines antiresonant reflektierenden Wellenleiters für Sensorzwecke zu nutzen. Als letzten Punkt untersucht diese Arbeit die Nutzung von dielektrischen Strukturen zur Wellenleitung von OPP Grundmoden und der gleichzeitigen Eignung zur logischen Prozessierung der geleiteten Moden aufgrund von Phasenunterschieden. Daraus folgt schließlich die experimentelle Demonstration der Funktionsfähigkeit eines optischen logischen Halbaddierers.

Schlagwörter: Plasmonische Sensoren, optische Logik-Bauelemente, Gouy-Phase-Shift, zeit-/phasenaufgelöste Leckstrahlungsmikroskopie

Abstract

Light has manifold applications in modern technology. Amongst others it promises optical computation, and sensing and producing devices with new high levels of accuracy. One critical subject to this, as in many industrial sectors, is the miniaturization. In this aspect this thesis will investigate the use of surface plasmon-polaritons (SPPs) to conduct sensing of information as well as the transport and processing of information in micrometer sized plasmonic logic devices. The sensing process and the logic devices in this thesis are investigated within the same experimental system.

For the investigation of the SPPs a leakage radiation microscope was used and extended with the ability of time and phase resolved measurements of propagating SPPs. Further, it was used to directly image the optical Fourier transformation of the investigated system for direct measuring of the change of propagation properties of SPPs. This was supported theoretically with the transfer matrix method and direct calculations of the time and phase resolved electric field distribution. For fabrication of the investigated structures this thesis took part in the development of a new low-cost, fast, and flexible lithographic method.

The thesis first investigates the variation of the phase of free propagating SPPs due to a change of the effective index through changing the surrounding media, as well as intrinsic phase changes through the Gouy phase shift by focusing of SPPs. Thereby this thesis gives the first experimental demonstration of the two dimensional Gouy phase shift in the optical regime. Further, it investigates sensing properties in the plasmonic counterpart to an antiresonant-reflecting optical waveguide. At last, it investigates the use of dielectric structures as single mode SPP waveguides and their ability to conduct direct logic signal processing using phase-differences switching and operation. This is concluded with the experimental demonstration of the functionality of a pure optical logic half-adder.

Keywords: PLASMONIC SENSING, OPTICAL LOGIC DEVICES, GOUY-PHASE-SHIFT, TIME/PHASE RESOLVED LEAKAGE RADIATION MICROSCOPY

Contents

Introduction

In 1902, Robert Williams Wood imaged an unexpected pattern of dark and bright regions in the reflection spectra of diffraction gratings on top of speculum metal [1, 2]. He did not know the origin of this phenomenon, but reported thereby the first experimental observation of surface plasmon-polaritons (SPP). The first atempt of an explanation was given by John William Strutt, the 3rd Baron Rayleigh, in 1907 [3] with his "On the Dynamical Theory of Gratings". Although, this was refined in 1941 by Ugo Fano [4], it was only in 1968, when Andreas Otto [5] and later in the same year Erwin Kretschmann and Heinz Raether [6] analysed and reported the actual excitation of SPPs, that a full description of the phenomenon was possible. Within this research, they found that SPPs offer the ability to bind optical fields to structures with dimensions down to one magnitude below the wavelength [7], enabling optical signal guiding and processing in small structures compared to the used wavelength. Beside this, they found that the properties of SPPs are very sensitive to the purity of the materials used and to the adsorption of contaminants on the samples.

Especially the ability to confine optical fields to sub-wavelength structures indicate interesting applications of SPPs as future computing devices, since this would not only drastically increase the available information bandwidth, but it would also help to overcome interconnect delays and heat generation associated with conventional integrated electronic circuits [8]. Different types of SPP waveguide concepts, enabling confined SPP guiding for data transport applications, such as channel plasmon-polaritons [9, 10], metal-insulator-metal structures [11], metal strips and nanowires [12], and dielectric-loaded SPP waveguides [13–15] have been proposed and investigated. Alternative schemes include long-range surface plasmon-polaritons [16–18], nanoparticle chains [19–22], and periodically structured metal surfaces, exhibiting bandgaps for SPPs [23–25].

However, these approaches have certain disadvantages with regard to the fabrication process, e.g. the mentioned nanowire structures are formed by chance, and precise slot waveguide fabrication requires expensive and time consuming ion beam lithography. This thesis engages here: The focus of the presented work will be on optical lithographically fabricated dielectric structures over extended metal layers for use as SPP waveguide systems, with the ability to perform optical signal processing. To carry this out, optical logic gates were chosen, since the main component of signal processing devices in today's electronics

are also electric logic gates [26], offering the possibility to directly port concepts from electronics to plasmonics. In this context a lithography method for cost efficient and flexible fabrication of any desired dielectric structure, which was developed in the scope of this work, will be introduced and discussed. Further, basic sensing abilities of free propagating and confined SPPs on the same metal layers as were used for signal processing structures, will be shown. Additionally, the first measurement of the Gouy phase shift, an inherent change of the phase when a converging beam passes its focus, for surface plasmon-polaritons in the optical spectrum, will be presented.

For the realization of all-optical logic elements with guided SPPs, two physical phenomena can be used: linear interference effects and non-linear processes [27–35]. Their theoretical investigation and experimental realization have recently been the subject of scientific literature. This employs semiconductor optical amplifier, four-wave mixing, photonic crystal structures, microring resonators, and spatial filtering [36–40]. Most of the former all-optical realizations of logic gates required either high laser intensities or bulky experimental setups. A much simpler implementation of logic devices, already allowing a high degree of integrability has been proposed using surface plasmons in nanowire networks [41]. The latter is based on SPP interference, which offers the advantage of rather low electromagnetic fields, avoiding excessive heating of the plasmonic structures. A disadvantage of this approach is that only randomly generated structures could be used.

The dielectric SPP waveguide structures, used in this thesis, circumvented this disadvantage since they are lithographically processable and thus, the desired structures can be directly fabricated. For low-cost, fast and flexible fabrication, this work took part in the development of a new lithographic method.

To mathematically gain access to SPPs, first the basic principles as derived by Raether [42] will be introduced as well as a brief introduction to the response of metal to light. To put the basic principles into a context with the experimental conditions, the transfer matrix method will be shown. As this enables a reasonable grasp of the concept of leakage radiation, which is the main experimental method, it will be discussed in more detail. Furthermore, the propagation properties of SPPs, as are described with a two dimensional approach of the Gaussian beam, will be presented. Since pulsed laser sources are used, laser pulses and their autocorrelation will be discussed, too. Finally, logic gates and their Boolean truth tables will be introduced in the last section of the theoretical part of this thesis.

The experimental methods will comprise first the newly developed lithographic approach. This technique consists of standard microscope technology which is employed to demagnify a chromium photomask, placed in the image plane of a microscope, into its object plane. The photomask, in turn, is built by demagnifying a printed transparency by a factor of ten onto a glass substrate, coated with an opaque metal film. One main focus lies in the ability for cost efficient and flexible generation of the structures. Another key aspect in the experimental methods will be the leakage radiation microscopy, as this is the main measuring concept, used in this thesis. For this work, this well described

technique [14, 15, 43, 44] is extended with a Michelson interferometer to enable spatial and temporal detuning of two replicas of the incident laser beam, and one Mach-Zehnder interferometer for phase and time resolved imaging of the leakage radiation.

In the results and discussion part, it will be shown first how to alternate the phase of propagating SPPs by increasing the effective refractive index of the SPPs through adding thin polymer layers to the plasmonic system, or exploiting the Gouy phase shift. Following this, dielectric waveguide structures for all optical switching to perform the integrated evaluation of given phase shift will be presented. Finally, the combination of these structures to a more complex logic device, an optical half-adder, will be presented.

Theory of surface plasmon-polaritons and their investigation by leakage radiation microscopy

2.1 Basic principles of the properties of SPP at multiple interfaces

A major part of this thesis concerns surface plasmon-polaritons. In general they are coherent charge density oscillations in the electron system bound to the surface of a metal.

The quantization of these coherent electron oscillations in general is called *plasmon.* Plasmons are distinguished into two classes: Oscillations within the volume of a medium are called bulk-plasmons. When they take place at the interface of two media, they are called surface-plasmons.

If electromagnetic fields propagates through a metal, they will induce this charge density oscillations of the electron system. The oscillations, in turn, will also induce electromagnetic fields. Therefore the fields and oscillations are coupled. This coupled state is called *polariton.*

The whole phenomenon is thus a combination of *plasmons* and *polaritons.* Occurring at the surface of a metal this is called *surface plasmon-polariton (SPP).*

2.1.1 The semi-infinite approach

To describe the dependence between the wave vector of SPPs and their vacuum wavelength λ –the dispersion relation– a simple system can be considered: Two infinite extended half spaces consisting of a dielectric medium and metal (the semi-infinite approach). In this case, the SPP dispersion relation is [42]:

$$k_{\mathsf{SPP}}(\lambda) = k_0(\lambda)\sqrt{\frac{\varepsilon_{\mathrm{d}}(\lambda)\varepsilon_{\mathrm{m}}(\lambda)}{\varepsilon_{\mathrm{d}}(\lambda) + \varepsilon_{\mathrm{m}}(\lambda)}}. \tag{2.1}$$

Here, $k_0 = 2\pi/\lambda$ is the vacuum wave vector of light and $\varepsilon_{\mathrm{d,m}} = \varepsilon'_{\mathrm{d,m}} + \mathrm{i}\,\varepsilon''_{\mathrm{d,m}}$ are the complex relative dielectric functions (ε_{r}) of the metal and the dielectric. Since the investigated media in this thesis are not magnetic, the permeability is supposed to be 1
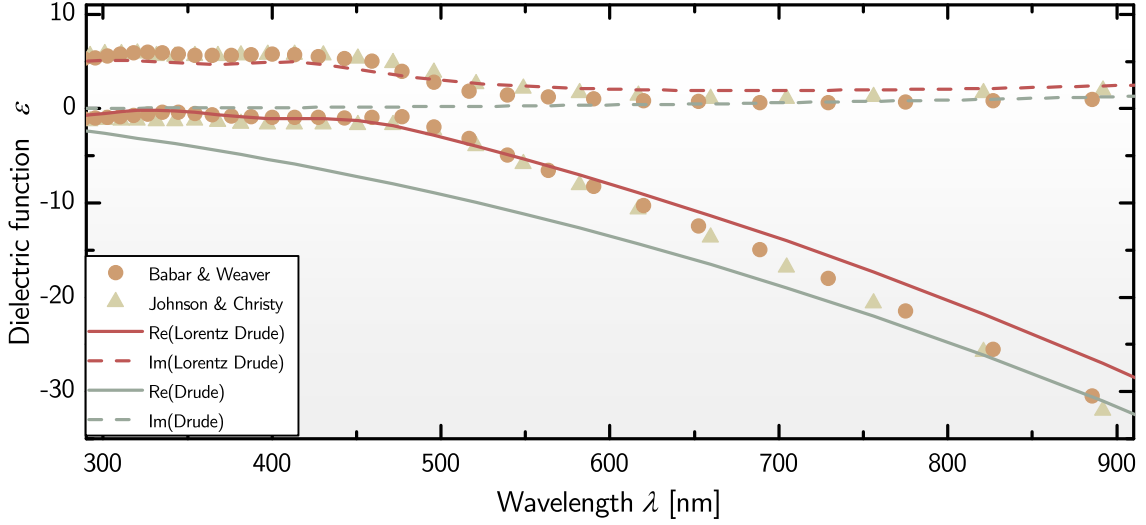
Figure 2.1: Plot of the Drude and the Lorentz-Drude approach for the dielectric function of Gold. The parameters for the functions were taken from [45]. The real and the imaginary part are the solid and dashed lines, respectively. For comparison, experimental data obtained from Johnson & Christy [46] and Babar & Weaver [47] are added as triangles and circles, respectively. It can be seen, that the Drude model itself already delivers valid values for the near-infrared region, whereas the Lorentz-Drude approach fits very well to the experimental data over the whole spectrum.

$(\mu_{\mathrm{r}} = 1)$. Therefore the refractive index

$$n = \sqrt{\varepsilon_{\mathrm{r}} \cdot \mu_{\mathrm{r}}}$$

can be expressed in its complex form as

$$\boxed{\begin{aligned} n_{\mathrm{d,m}} &= n'_{\mathrm{d,m}} + \mathrm{i}\, n''_{\mathrm{d,m}} \\ &= \sqrt{\varepsilon'_{\mathrm{d,m}} + \mathrm{i}\, \varepsilon''_{\mathrm{d,m}}}. \end{aligned}}$$

Eq. 2.1 yields in a complex wave vector $k_{\mathrm{SPP}} = k'_{\mathrm{SPP}} + \mathrm{i}k''_{\mathrm{SPP}}$, where the imaginary part incorporates the intrinsic propagation losses of the SPP. With the wave vector k_{SPP}, the wavelength λ_{SPP} and propagation length L_{SPP} of propagating SPPs can be calculated as [42]:

$$\boxed{\begin{aligned} \lambda_{\mathrm{SPP}} &= \frac{2\pi}{k'_{\mathrm{SPP}}} \\ L_{\mathrm{SPP}} &= \frac{1}{2\,k''_{\mathrm{SPP}}}. \end{aligned}}$$

In the simplest case, one of the media is a metal whereas the second medium is vacuum, where the dielectric function can be assumed to be 1 in every case. Eq. 2.1 then simplifies to

$$k_{\mathsf{SPP}}(\lambda) = k_0(\lambda)\sqrt{\frac{\varepsilon_m(\lambda)}{1 + \varepsilon_m(\lambda)}}, \tag{2.2}$$

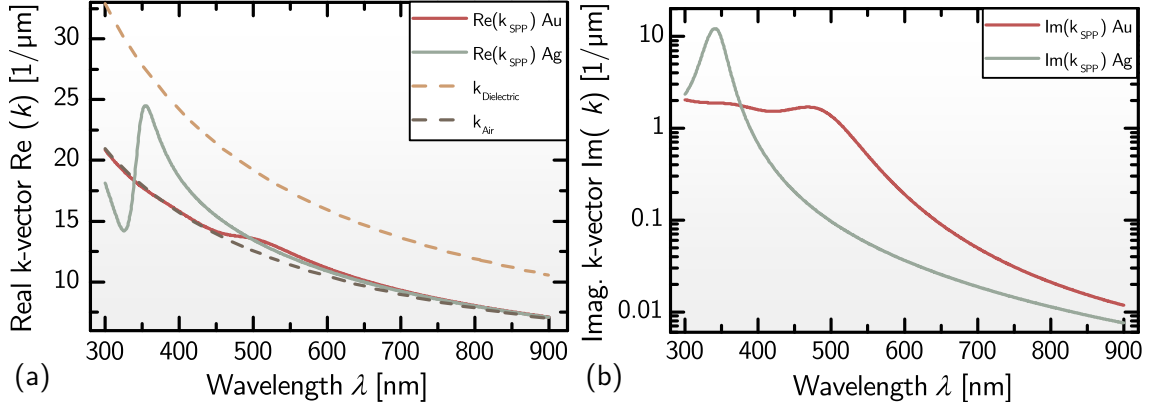Figure 2.2: **(a)** Real and **(b)** imaginary part of the wave vector of gold and silver in the semi-infinite approach, respectively. The light line of air and a standard microscope cover glass as dielectric medium is added to depict the magnitude of the SPP wave vector in comparison of free propagating light. It can be seen that the wave vector of SPPs for wavelength above 373 nm for gold and 340 nm for silver is greater than the respective wave vector of light in air, but the damping (imaginary k-vector) is considerably higher at these wavelengths. The respective wave vector of light in the cover glass is greater than that of the SPPs.

where the only frequency dependence origins from the dielectric function of the metal.

2.1.2 The Lorentz-Drude model

A commonly used expression for the wavelength dependent complex dielectric function of metal $\varepsilon(\lambda)_{\mathrm{m}}$ is the Lorentz-Drude model [45, 48]

$$\boxed{\varepsilon(\lambda)_{\mathrm{m,LD}} = \varepsilon(\lambda)_{\mathrm{D}} + \varepsilon(\lambda)_{\mathrm{L}}.}$$

(2.3)

This approach consists of two addends, $\varepsilon(\lambda)_{\mathrm{D}}$ and $\varepsilon(\lambda)_{\mathrm{L}}$, where the first one represents the response for a free electron gas whereas the second term describes the intra and inter band transitions in the metal due to an external field [49]:

$$\varepsilon(\lambda)_{\mathrm{D}} = 1 - \frac{2\pi c_0}{\lambda_{\mathrm{p}}^2} \left(\frac{2\pi c_0}{\lambda^2} + \frac{i\,\Gamma_0}{\lambda} \right)^{-1}$$

$$\varepsilon(\lambda)_{\mathrm{L}} = \sum_{j=1}^{m} f_j \frac{2\pi c_0}{\lambda_{\mathrm{p}}^2} \left(\left[\frac{2\pi c_0}{\lambda_{\mathrm{j}}^2} - \frac{2\pi c_0}{\lambda^2} \right] + \frac{i\,\Gamma_j}{\lambda} \right)^{-1},$$

where, c_0 is the speed of light in vacuum, m is the amount of electrons bound to valence states at the metal ions, f_j the contribution amplitude of each bound electron and λ_j the wavelength of their oscillation. Γ_0 and Γ_j are the damping of the free electrons due to the mean free path length of the free and the lifetime of the bound states, respectively. λ_{p} is the wavelength of the plasma oscillation $\omega_{\mathrm{p}} = \sqrt{n_{\mathrm{e}}\,e^2/\varepsilon_0\,m_{\mathrm{e}}}$ in the metal with n_{e} the electron density, e the elementary charge, ε_0 the permittivity of vacuum and m_{e} the electron mass.

Even though the Lorentz-Drude approach consists of a response function for the free electron gas (ε_D), which is the Drude model, and for the semiquantum Lorentz result of an insulator (ε_L) [45], this describes the dielectric function very well [50, 51].

To visualize this correlation, the Drude and the Lorentz-Drude models are plotted together with data obtained experimentally for the dielectric function of gold in Fig. 2.1. Here is clearly visible that especially for the imaginary part, the Drude model in itself is already valid in the near-infrared region, whereas the Lorentz-Drude approach offers good overlap to the experimental data for the whole visible and near-infrared spectrum. With the given dielectric function for a metal in Eq. 2.3, the SPP dispersion relation of Eq.2.2 can be plotted, as is shown in Fig. 2.2(a) and Fig. 2.2(b) for the real and imaginary part, respectively. It can be seen that SPPs on both metals have a larger wave vector than free propagating light in air for the whole visible and near-infrared spectrum. Only below 373 nm for gold and 340 nm for silver is the opposite the case, although here damping effects through the imaginary part of the wave vector are relatively high. This means, that L_SPP is there below one wavelength. Thus, light can not couple directly from air to propagating SPPs. Further it is visible in Fig. 2.2(b), that except for wavelengths below 340 nm, silver incorporates lower losses than gold. Damping effects decrease significantly for both metals in the near-infrared region. For this reason, SPP experiments, especially on gold, take place preferably at longer wavelengths.

2.1.3 Excitation methods for SPPs

Another depicted dispersion relation in Fig. 2.2(a) is the one of light in a microscope cover glass, which is used as substrate in this thesis. There, the wave vector is in any case greater than that of the SPPs at an air/metal interface. In a system where the metal is sandwiched between air and a dielectric, the light in this dielectric would have a wave vector k_d, where the parallel to the metal layer orientated wave vector component would be $k_\parallel = k_\mathrm{d} \sin\theta$. As k_d is greater than k_SPP, $k_\parallel$ can be easily matched to k_SPP by tilting the laser beam by an appropriate angle θ_SPP to fulfil the relation

$$\boxed{k_\parallel = k_\mathrm{d} \sin\theta_\mathrm{SPP} = k_\mathsf{SPP},} \tag{2.4}$$

and to excite SPPs in the metal layer as shown in Fig. 2.3(b). This mechanism was introduced by Kretschmann and Raether and is the main principle in the Kretschmann configuration for excitation of SPPs [6]. In this approach, the SPPs can be obtained as a Lorentz shaped dip in the reflection spectra of the laser beam used [52]. Since the angle θ_SPP of this dip is greater than the angle of total internal reflection in glass, it can not be achieved with substrates offering a dielectric/air interface, which is parallel to the metal film. For this reason, the Kretschmann configuration uses a prism shaped substrate. Another technique to avoid parallel interfaces between two media with different refractive index is the use of immersion oil optics.

The reverse process can also take place: propagating SPPs at an air/metal interface
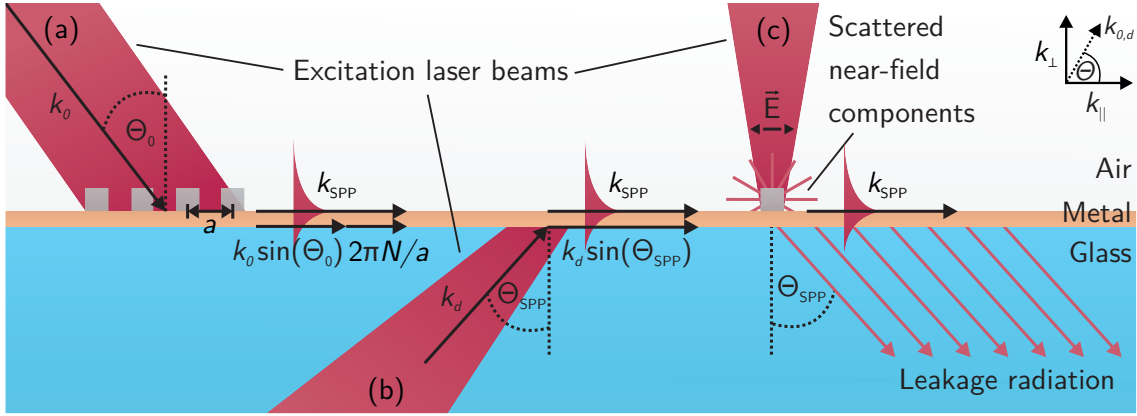
Figure 2.3: Illustration of the three SPP excitation methods mentioned with the associated wave vectors and angles. **(a)** Excitation of SPPs utilising a grating with lattice period a, **(b)** excitation of SPPs by the Kretschmann method, and **(c)** excitation of SPPs through scattered near-field components. The leakage radiation depicted can occur in every excitation scheme.

can couple to optical modes of an underlying substrate with higher refractive index. This phenomenon is called leakage radiation and will be discussed in Sect. 2.2.

As already shown in Eq. 2.4, for successful excitation $k_\parallel$ has to be matched to k_{SPP}. A generalised expression of this equation is

$$k_\parallel = k_0 \sin\left(\theta_0\right) + \Delta k_\parallel = k_{\text{SPP}} \tag{2.5}$$

with k_0 the wave vector in air and θ_0 the incident angle of the beam.

It has been shown that light with this incident angle hitting a grating with lattice period a can have wave vectors $k_\parallel = k_0 \sin\left(\theta_0\right) \pm 2\pi N/a$ (N is an integer) [42]. An easy comparison shows that a grating can thus serve to match the wave vector of light to the wave vector of SPPs with $\Delta k_\parallel = 2\pi N/a$ to fulfil Eq. 2.5 [42] as depicted in Fig. 2.3(a).

A third excitation method is the use of single localized scatterers, as single ridges are. In this case, the additional wave vector components $\Delta k_\parallel$ are provided via scattered near-field components [19] which is shown in Fig. 2.3(c).

2.2 Leakage radiation

The ability to couple light into SPPs at an air/metal interface in the Kretschmann configuration works because k_{SPP} and $k_{\parallel}$ in the dielectric are matched by tilting the incident light by θ_{SPP} to fulfil $k_{\parallel} = k_{\text{d}} \sin \theta_{\text{SPP}} = k_{\text{SPP}}$ (Eq. 2.4). In any SPP system, independent from the excitation scheme, the reverse effect can take place too, when this relation can be fulfilled: Propagating SPPs from the air/metal interface can couple to light with an angle θ_{SPP} in the substrate. This outcoupled light is called *leakage radiation (LR)*. This is illustrated in the right part of Fig. 2.3. In the matching condition above, k_{d} can be expressed with the refractive index of the dielectric n_{d} as

$$k_{\text{d}} = k_0 \, n_{\text{d}}.$$

Thereby, the condition of Eq. 2.4 can be rewritten as

$$\boxed{\begin{aligned} k_{\text{SPP}} &= k_0 \, n_{\text{d}} \sin \theta_{\text{SPP}} \\ &= k_0 \, n_{\text{eff,SPP}}. \end{aligned}} \tag{2.6}$$

In this relation, $n_{\text{eff,SPP}}$ is the effective refractive index (in the latter referred to as effective index) of the SPPs, which directly connects the vacuum wave vector k_0 with the SPP wave vector k_{SPP}.

This implies that the propagation parameters of SPPs, and thus the plasmonic system, can be characterised with the angle of the reflection dip in the Kretschmann configuration [52] as well as with the angle of LR [43].

As discussed earlier, the angle of leakage radiation is greater than the angle of total internal reflection. Thus, for imaging of LR, immersion optics have to be used. This can be done for example with leakage radiation microscopy, which will be introduced in Sect. 3.3, as well as the possibility of direct access to the LR angle – and thus the effective index of SPPs – via implementation of a $4f$-telescope.

2.3   The transfer matrix method

As described above, plasmonic systems can be characterised by the angle and the width of a reflection dip as it would occur in the Kretschmann configuration.

2.3.1 The Fresnel equations

The fractions of the reflected (and transmitted) *amplitudes* (these are the reflectance r and transmittance t) of light at the interface of two infinite extended half spaces can be calculated with the Fresnel equations [42]. These are for perpendicular (s) and parallel (p) polarized light, passing the interface of the media i and j [53]

$$t^{\mathrm{s}}(i,j,\theta) = \frac{2\,k_{\perp}(i,\theta)}{k_{\perp}(i,\theta) + k_{\perp}(j,\theta)} \qquad\qquad r^{\mathrm{s}}(i,j,\theta) = \frac{k_{\perp}(i,\theta) - k_{\perp}(j,\theta)}{k_{\perp}(i,\theta) + k_{\perp}(j,\theta)}$$

$$t^{\mathrm{p}}(i,j,\theta) = \frac{2\,n_i\,n_j\,k_{\perp}(i,\theta)}{n_j^2\,k_{\perp}(i,\theta) + n_i^2\,k_{\perp}(j,\theta)} \qquad r^{\mathrm{p}}(i,j,\theta) = \frac{n_j^2\,k_{\perp}(i,\theta) - n_i^2\,k_{\perp}(j,\theta)}{n_j^2\,k_{\perp}(i,\theta) + n_i^2\,k_{\perp}(j,\theta)}$$

where $n_{i,j} = n'_{i,j} + \mathrm{i}\,n''_{i,j}$ is the complex refractive index of the respective medium. In these equations, the wave vector is split into its perpendicular ($k_{\perp}$) and parallel ($k_{\parallel}$) components relative to the interface. They are linked trigonometrically with

$$k_{\perp}(i,\theta) = \sqrt{k_0^2\,n_i^2 - k_{\parallel}(i,\theta)^2},$$

where k_0 is the wave vector in vacuum and n_i the refractive index of the i-th medium. The parallel component of the wave vector is

$$k_{\parallel}(i,\theta) = k_0\,n_i\,\sin\theta_i.$$

The reflection R and transmission T distribution of the intensity of the light can then be obtained with the square of the absolute value

$$R^{\mathrm{s,p}}(i,j,\theta) = |r^{\mathrm{s,p}}(i,j,\theta)|^2 \qquad\qquad T^{\mathrm{s,p}}(i,j,\theta) = |t^{\mathrm{s,p}}(i,j,\theta)|^2.$$

However, the investigated SPPs in this thesis propagate in fact on – in regard to the wavelength – thin metal films between glass and air and not the interface of two infinite large half spaces. In some cases, the metal films are additionally covered with another thin polymer layer. This implies multiple interfaces and also interference effects when the layer thicknesses are in the range of the coherence length of the light, which has to be considered. A very useful approach to handle this multilayer systems is the transfer matrix method (TMM).

2.3.2 Transfer matrix method

This method uses the Fresnel equations to describe the reflection and transmission at single interfaces with matrices and expands them to a larger but finite number of interfaces by
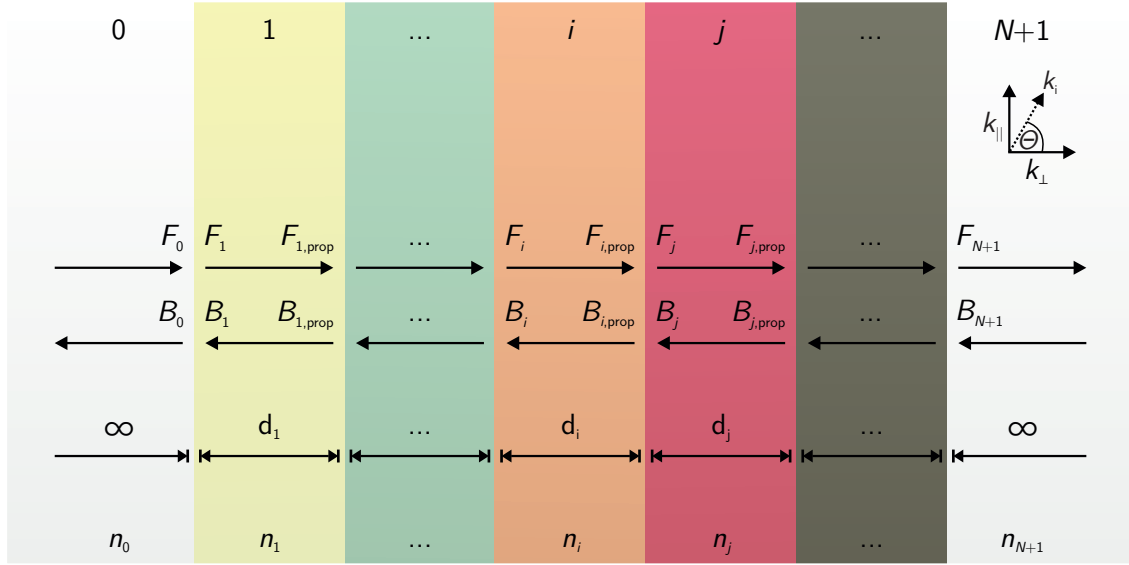
Figure 2.4: Outline of the transfer matrix method: In a multilayer system with $N + 2$ layers of thickness d_i, the forward (F) and backward (B) propagating waves are considered. Propagation effects $F_i \rightarrow F_{i,\mathrm{prop}}$ for each layer, and the reflectance and transmittance at each interface are calculated in single matrices. The overall reflection and transmission is then described by the matrix product of all matrices.

calculating the matrix product of the matrices from each interface. This process is depicted in Fig. 2.4 with the respective forward (F_i) and backward (B_i) propagating waves in each medium i with thickness d_i and refractive index n_i. It is assumed that a system of N layers is sandwiched between two infinite extended half spaces of the media 0 and $N + 1$ in which the light waves are emitted and detected respectively. Thus a system of N layers will be described by a stack of $N + 2$ media. For one single interface between medium i and j, the amplitudes F and B of the light waves before and behind the interface are linked with the matrix $\mathbf{T}$, consisting of the Fresnel equations with

$$\begin{pmatrix} F_i^{\mathrm{s,p}} \\ B_i^{\mathrm{s,p}} \end{pmatrix} = \frac{1}{t^{\mathrm{s,p}}(i,j,\theta)} \begin{pmatrix} 1 & r^{\mathrm{s,p}}(i,j,\theta) \\ r^{\mathrm{s,p}}(i,j,\theta) & 1 \end{pmatrix} \begin{pmatrix} F_j^{\mathrm{s,p}} \\ B_j^{\mathrm{s,p}} \end{pmatrix} = \mathbf{T}_{i,j}^{\mathrm{s,p}} \begin{pmatrix} F_j^{\mathrm{s,p}} \\ B_j^{\mathrm{s,p}} \end{pmatrix}.$$

This is valid, as written above, for s- and p-polarisation states, depending which Fresnel equation is used. Thus, for a better readability, the indication of which polarisation is meant will be omitted in the following. As already mentioned, interference effects within the layer have to be considered when its thickness d_i is in the range of the coherence length of the used light. This is implemented by an additional propagation matrix $\mathbf{P}$

$$\begin{pmatrix} F_{i,\mathrm{prop}} \\ B_{i,\mathrm{prop}} \end{pmatrix} = \begin{pmatrix} e^{-\mathrm{i}\,d_i\,k_{\perp,i}} & 1 \\ 1 & e^{\mathrm{i}\,d_i\,k_{\perp,i}} \end{pmatrix} \begin{pmatrix} F_i \\ B_i \end{pmatrix} = \mathbf{P}_i \begin{pmatrix} F_i \\ B_i \end{pmatrix}.$$

The combination of both matrices yield in

$$\begin{pmatrix} F_{i,\text{prop}} \\ B_{i,\text{prop}} \end{pmatrix} = \mathbf{P}_i \, \mathbf{T}_{i,j} \begin{pmatrix} F_j \\ B_j \end{pmatrix},$$

where the result of the matrix product $\mathbf{P}_i \, \mathbf{T}_{i,j}$ is the transfer matrix for one interface.

For a multilayer system the transition matrix is then simply the matrix product of every interface

$$\mathbf{M} = \mathbf{T}_{0,1} \prod_{i=1}^{N} \mathbf{P}_i \, \mathbf{T}_{i,i+1}$$

and thus the propagation of the whole layer stack is described by

$$\begin{pmatrix} F_0 \\ B_0 \end{pmatrix} = \mathbf{M} \begin{pmatrix} F_{N+1} \\ B_{N+1} \end{pmatrix} = \begin{pmatrix} M_{11} & M_{12} \\ M_{21} & M_{22} \end{pmatrix} \begin{pmatrix} F_{N+1} \\ B_{N+1} \end{pmatrix}. \tag{2.7}$$

To calculate the reflection and transmission of the whole system, it is assumed that $B_{N+1} = 0$. This simplifies Eq. 2.7 to

$$F_0 = M_{11} \, F_{N+1} \qquad\qquad\qquad B_0 = M_{21} \, F_{N+1}.$$

The reflectance is now the ratio between the backward and the forward propagating waves in front of the first interface

$$r = \frac{B_0}{F_0} = \frac{M_{21}}{M_{11}}$$

and the transmittance is the ratio between the forward propagating waves behind the last interface and in front of the first interface

$$t = \frac{F_{N+1}}{F_0} = \frac{1}{M_{11}}.$$

The reflection and transmission is again the respective square of the absolute value ($R = |r|^2, T = |t|^2$).
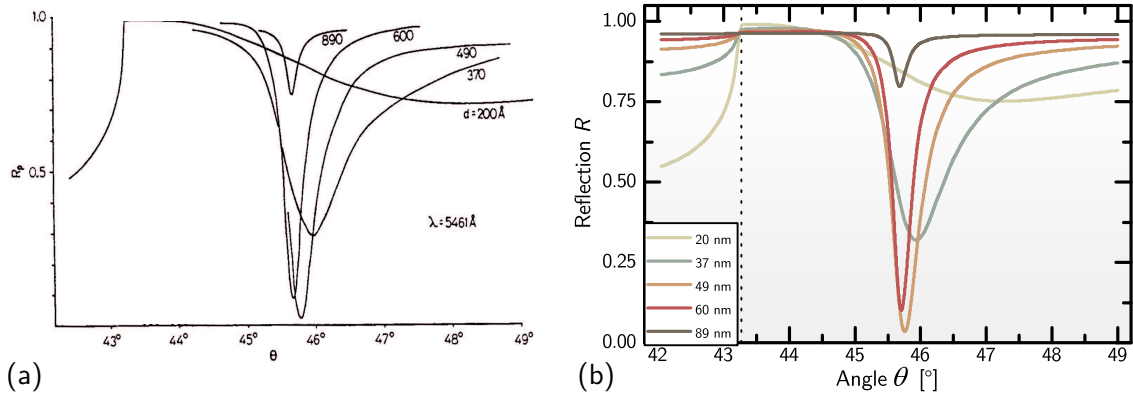
Figure 2.5: **(a)** Reflection spectra of silver layers with different thicknesses underneath an incoupling prism shown by Raether as Fig. 2.9 in [42]. **(b)** Calculations for the same system performed with the transfer matrix method. A very good correlation between both methods can be seen. In both graphs the angle of total internal reflection is clearly obtainable at 43.25 °(marked with a dotted line), in front of the respective reflection minimum, which represents θ_{SPP}.

As already mentioned, SPPs can be excited when a laser beam is targeting a thin metal layer sandwiched between air and another dielectric with an appropriate angle θ_{SPP}. Amongst others, this was described by Raether in his book [42] for a three layer system consisting of silver films with different thicknesses between a prism and air. For this, the Fresnel equations for a three layer system were used. In this thesis, the same calculations for the same system were performed by the TMM to validate its functionality. The comparison of these results with Raethers original published data are shown in Fig. 2.5 and prove a very high accuracy of the TMM. The calculations were conducted in Maple and the used code is shown exemplary in Appendix A.1.

2.3.3 Comparison of the TMM and the semi-infinite approach

In addition, Fig. 2.5 demonstrates that the TMM, in combination with Eq. 2.4, is able to calculate k_{SPP} – and therefore the dispersion relation – for any multilayer system in which LR occurs. To put this into a context with the semi-infinite approach from Eq. 2.1 in Sect. 2.1, dispersion relations were calculated for gold and silver films of different thicknesses with both approaches. The wavelength range was chosen to match with the used laser sources. This comparison is shown for gold in Fig. 2.6(a), where it can be seen, that both dispersion relations coincide very well at layer thicknesses above 20 nm. To examine this in a more sophisticated manner the proportion of the difference from the TMM to the semi-infinite approach is shown in Fig. 2.6(b) for gold and silver, respectively. As indicated with the dotted lines, the difference is already lower than 1 % for layer thicknesses greater than 36 nm for gold and 30 nm for silver. This implies that for systems without additional polymer layer on top of the metal, and metal thicknesses in the range of 50 nm, the dispersion relation can safely taken from the semi-infinite approach.
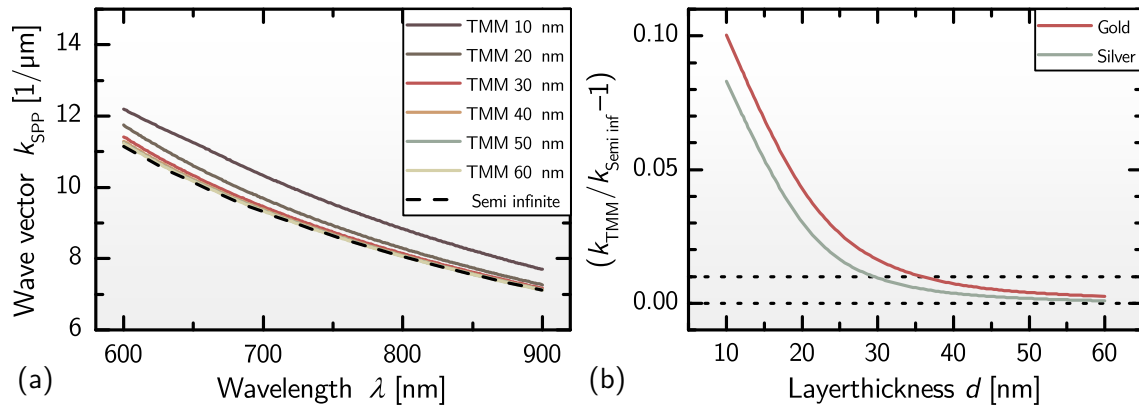
Figure 2.6: **(a)** Dispersion relation of SPPs on gold layers with different thicknesses calculated with the TMM, in comparison with the dispersion relation calculated with the semi-infinite approach. **(b)** Ratio of the difference from the TMM dispersion relation to the semi-infinite dispersion relation for gold and silver. It can be seen, that the difference is already below 1% for $30\,\text{nm}$ thick silver and $36\,\text{nm}$ thick gold layers.

2.4 Free propagating SPP beams

One part of this work deals with free propagating SPPs on plane metal layers. These are either plane SPP waves or focused SPP beams. The plane waves will be used to show how SPPs can be affected by additional thin polymer layers on top of the metal. The focused SPP beams will be employed to present a different but very important effect: the Gouy phase shift. This is a longitudinal phase shift for light waves passing through the focal point with respect to the phase front of collimated light beams [54, 55]. It will be discussed in detail in Sect. 4.1.2.

Both the plane and the focused kinds of SPP beams are excited by focusing laser beams on single polymer ridges with dimensions below the wavelength. In this configuration, the SPP beam resembles a two dimensional projection of the initial laser beam [56, 57]. This implies two things: First, because the incident laser beam in this thesis is of Gaussian shape, the resulting SPP beam has to be considered as a two dimensional Gaussian beam. Second, because of the Gaussian shape of the incident laser, it offers a distinct wave front curvature as a function of the distance from the focus. Therefore, the SPP beam can be focused or collimated to a plane wave by altering the distance of the laser beam focus with respect to the polymer ridge at the sample [56, 57].

2.4.1 Plane waves

When the focus of the exciting laser beam is far away from the metal layer, the wave front curvature can be neglected and the paraxial SPP beam can be treated as a simple plane wave:

$$E_{\mathrm{Plane}}(z,t) \propto \exp\left(\mathrm{i}\,\omega\,t - \mathrm{i}\,k_{\mathrm{SPP}}\,z\right), \tag{2.8}$$

where ω is the angular frequency of the light, t is the time and z is the propagation direction. The distribution in the perpendicular directions of z can be neglected in this case, because the SPP beam diameter is much larger than the imageable field of view of the sample.

2.4.2 Gaussian focus

For the case where the SPP beam is focused, however, the field distribution perpendicular to z cannot be neglected. Since then the SPP beam is of Gaussian shape, the expression for this distribution can be derived from the Huygens-Fresnel integral [58]. With the beam waist in the focus w_0, the Rayleigh length $z_{\mathrm{R}} = n\,\pi\,w_0^2/\lambda_{\mathrm{SPP}}$ and the wave vector $k_{\mathrm{SPP}} = 2\,\pi/\lambda_{\mathrm{SPP}}$, the resulting equation can be written as

$$E_{\mathrm{Gauss}}(\mathbf{r},z,t) \propto f(z)\,\exp\left(\mathrm{i}\,\omega\,t - \mathrm{i}\,k_{\mathrm{SPP}}\,z - \frac{\mathbf{r}^2}{w_0^2\left(1 - \frac{\mathrm{i}\,z}{z_{\mathrm{R}}}\right)}\right).$$

The differences of the expression for the two or three dimensional case are the radius with $\mathbf{r}_{2D}^2 = x^2$ and $\mathbf{r}_{3D}^2 = (x^2 + y^2)$, and the normalisation factor

$$f(z)_{2D} = \sqrt{\frac{1}{1 - \dfrac{\mathrm{i}\,z}{z_{\mathrm{R}}}}} \qquad\qquad f(z)_{3D} = \frac{1}{1 - \dfrac{\mathrm{i}\,z}{z_{\mathrm{R}}}}.$$

which is dependent on the propagation distance

2.4.3 Gouy phase shift

On the propagation axis ($\mathbf{r}$=0), this factor $f(z)$ is the only difference to a plane SPP wave. When $f(z)_{3D}$ is expressed with Euler's formula ($z = |z|\exp\mathrm{i}\varphi_z$) of complex values (for the derivation see Appendix A.2)

$$\begin{aligned}
f(z)_{3D} &= \frac{1}{1 - \dfrac{\mathrm{i}\,z}{z_{\mathrm{R}}}} \\
&= \frac{1}{\sqrt{1 + \left(\dfrac{z}{z_R}\right)^2}}\,\exp\left(\mathrm{i}\arctan\left(\frac{z}{z_{\mathrm{R}}}\right)\right),
\end{aligned} \qquad (2.9)$$

an additional phase shift of $\varphi = \arctan z/z_{\mathrm{R}}$, when passing the focus, can be seen. This phenomenon is called the *Gouy phase shift* [54,55] and can be explained with the uncertainty relation: since the convergent waves have a finite spatial extent when passing a caustic, the wave vector has to consist of a superposition of transversal and longitudinal components. Feng and Winful stated in [59] that this yields in the relation $(\Delta k_x)_m (\Delta x)_m = m + 1/2$ (m is the order of the laser beam mode) for each transversal dimension of the beam. This leads to a shift of

$$\varphi_{\mathrm{Gouy,2D}} = \frac{1}{2}\arctan\left(\frac{z}{z_{\mathrm{R}}}\right). \qquad (2.10)$$

for two dimensional beams, as SPPs are, for the ground mode of the laser. Following [60], this is in perfect accordance with Eq. 2.9:

$$\frac{1}{1 - \dfrac{\mathrm{i}\,z}{z_{\mathrm{R}}}} = \frac{1}{\sqrt{1 + \left(\dfrac{z}{z_R}\right)^2}}\,\exp\left(\mathrm{i}\arctan\left(\frac{z}{z_{\mathrm{R}}}\right)\right)$$

$$\Downarrow$$

$$\sqrt{\frac{1}{1 - \dfrac{\mathrm{i}\,z}{z_{\mathrm{R}}}}} = \sqrt{\frac{1}{\sqrt{1 + \left(\dfrac{z}{z_R}\right)^2}}}\,\exp\left(\frac{\mathrm{i}}{2}\arctan\left(\frac{z}{z_{\mathrm{R}}}\right)\right).$$

2.5 Laser pulses

The laser beam for excitation of SPPs was generated by means of a titan:sapphire oscillator, which could be set into continuous wave and mode-locked operation.

In the latter, about 10^5 spectral modes, Gaussian distributed around one central wavelength, are superposed in the laser cavity, yielding through Fouriers theorem in an ultrashort wave packet. The shape of this package is the Fourier transformation of the spectral shape of the modes, which is again a Gaussian distribution. It can be mathematically described by [61, 62]

$$E_{\mathrm{pulse}}(z,t) = \exp\left(-2\log 2\left(\frac{t - z/v_{\mathrm{g}}}{\tau}\right)^2\right), \tag{2.11}$$

where τ is the temporal full width at half maximum (FWHM) and v_{g} the group velocity of the pulse. This is connected to the dispersion relation $\lambda(k)$ with $v_{\mathrm{g}} = \partial\lambda/\partial k|_{k0}$ meaning that it can be different from the phase velocity $v_{\mathrm{p}} = \lambda/k$. Since the pulse is a superposition of different wavelengths, the phase velocity implies that the pulse can spread spatially and temporally while propagating through dispersive media, because parts with different wavelength offer different velocities. This phenomenon is described by the group velocity dispersion (GVD) $\mathrm{GVD} = \partial^2\lambda/\partial k^2|_{k0}$.

However, since $\lambda(k)$ can be approximated to be linear for every investigated medium in this thesis and the examined propagation distances are rather short, this pulse spreading effect can be safely neglected in the evaluation of the results.

Nevertheless, the optical setup which will be introduced in Sect. 3.3, contains enough dispersive media to considerably spread the laser pulse before excitation of the SPPs. To compensate this, a countervailing amount of negative group velocity dispersion is inserted into the pulse by an additional prism pair in the beam path.
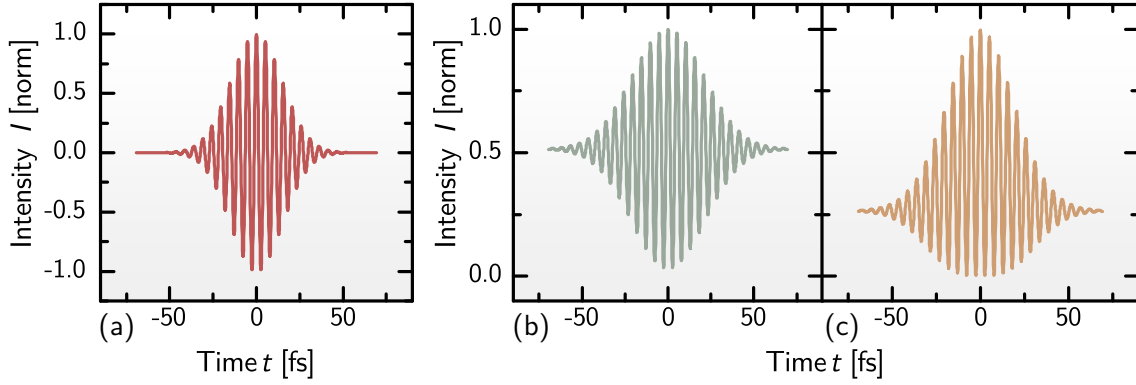
Figure 2.7: **(a)** Comparison of a plane wave laser pulse (product of Eq. 2.8 and 2.11 at $z = 0$, $\lambda = 1.6\,\mu m$ and $\tau = 25\,fs$) **(b)** with its field (Eq. 2.12) and **(c)** interferometric (Eq. 2.13) autocorrelation.

2.6 Autocorrelation

One experiment which will be discussed in Sect. 4.3.1 offered the opportunity to let two SPP pulses, which were excited with two replicas of the same laser pulse, interfere coherently with each other. This interference took place directly in the junction point of two crossing waveguides. Thus, the recorded interference intensity was constant over the time. This effect can be mathematically described by the autocorrelation of those two SPP pulse replicas

$$A_{\text{Field}}(\tau) = \int_{-\infty}^{+\infty} E_{\text{SPP}}(t) E_{\text{SPP}}^{*}(t - \tau) dt, \tag{2.12}$$

where $E_{\text{SPP}}(t)$ is the complex electric field of the SPP (e.g. for pulsed plane waves the product of Eq. 2.8 and 2.11) and $E_{\text{SPP}}^{*}(t)$ is its complex conjugate. Since in this case the field of the pulse interferes, A_{Field} is called the *field autocorrelation.*

It has to be noted that this autocorrelation do not provide information about pulse stretching effects so that it can not be related to the actual pulse length.

To obtain the real pulse length, one would have to implement non-linear effects to yield an autocorrelation signal which is $\propto I^2 = |E^2|^2$. Even with a detector that has a response time which is much longer than the actual pulse length, the signal would then be

$$I_{\text{Interferometric}}(\tau) = \int_{-\infty}^{+\infty} \left| (E(t) + E^{*}(t - \tau))^2 \right|^2 dt. \tag{2.13}$$

This is the *interferometric autocorrelation.*

But as mentioned above, only A_{Field} was measured in this work. The $I_{\text{Interferometric}}$ was merely added for reasons of comparison and to establish that this is the only autocorrelation where the actual pulse length can be determined. This comparison of the pulse, the field and the interferometric autocorrelation is shown in Fig. 2.7.
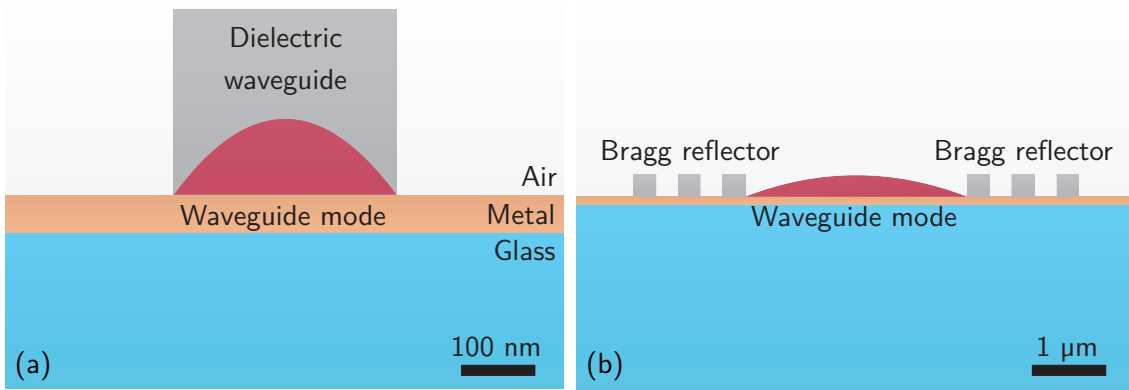
Figure 2.8: **(a)** Scheme of a dielectric-loaded SPP waveguide, where the waveguide mode is confined within the dielectric structure because of its higher refractive refractive index. **(b)** Scheme of a plasmonic analogue to an antiresonant-reflecting optical waveguide where the waveguide mode is confined between two periodically placed dielectric waveguides, forming a Bragg reflector.

2.7 Waveguides

Beside free propagating SPPs, this thesis concerns confined SPP propagation. This was achieved by two approaches: First the use of dielectric waveguide structures, confining the SPPs by their –in contrast to the surrounding– higher refractive index [63, 64]. An illustration of this concept is shown in Fig. 2.8(a). The second approach employed a periodic sequence of dielectric ridges embedding a region of the plain metal surface a few micrometer wide. The periodicity was chosen to model Bragg reflectors, which confined the SPPs within the region between the dielectric ridges by forming the plasmonic equivalent of an antiresonant-reflecting optical waveguide (ARROW) [65–67]. This concept is shown in Fig. 2.8(b). While the first method confines the SPP mode to dimensions below the wavelength [68], the ARROW waveguide confines the SPP mode to rather large areas, but offers much higher propagation length and provides a direct accessibility of the plasmonic field [67].

2.7.1 Finite element method

In both cases the effective index $n_{\mathrm{SPP,wg}}$, which connects the wave vector in the waveguide $k_{\mathrm{SPP,wg}}$ with the wave vector in vacuum k_0 by $k_{\mathrm{SPP,wg}} = n_{\mathrm{SPP,wg}} \cdot k_0$, was found with the finite element method. In this case, the cross section of the waveguide structure is taken and divided into several unit cells. In each cell, the magnetic and electric field vectors are calculated by solving a functional of the partial differential equation [68, 69]

$$\nabla_{x,y}\vec{E} + \left(\varepsilon\, k_0^2 - k_{\mathrm{SPP,wg}}^2 \right) \vec{E} = 0,$$

while the continuity condition for parallel components of the electric and magnetic fields and the perpendicular components of the electric and magnetic flux densities has to be
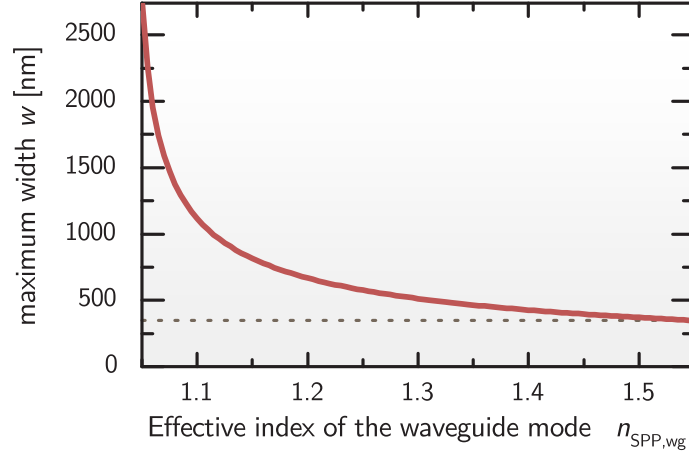
Figure 2.9: Plot of the maximal width of dielectric-loaded SPP waveguides for single mode guiding, depending on the effective index of the guided mode. For the calculation, Eq. 2.14 was used. It was assumed that the SPPs were excited with 800 nm light and the effective index of the guided mode has to be proportional to the waveguide height, it has to be greater than the effective index of free propagating SPPs ($n_{\mathrm{SPP,free}} = 1.04$) and it can not be higher than the refractive index of the waveguide material, which is 1.52 for 800 nm (cf. Sect. 3.3). For eye-guidance, an additional dotted line was plotted at 350 nm, to visualize the expected waveguide width for single mode operation in all cases.

satisfied. In this work the finite element calculations were conducted with the software FEMSim from RSoft.

2.7.2 Single mode condition

In this thesis however, all waveguides were used in single mode operation. When the effective index of a dielectric-loaded waveguide $n_{\mathrm{SPP,wg}}$ is found for a distinct height of the waveguide, the maximal width w, to prevent multi mode SPP guiding, can be determined with [68]

$$w = \frac{\pi}{k_0 \sqrt{n_{\mathrm{SPP,wg}}^2 - n_{\mathrm{SPP,free}}^2}}, \tag{2.14}$$

where $n_{\mathrm{SPP,free}}$ is the effective index of free propagating SPPs on the metal layer. This relation was plotted in Fig. 2.9 with the assumptions that the SPPs are excited with light with 800 nm wavelength, that the effective index of the guided mode is proportional to the waveguide height, that it has to be greater than the effective index of free propagating SPPs ($n_{\mathrm{SPP,free}} = 1.04$), and that it can not be higher than the refractive index of the waveguide material, which is 1.52 for 800 nm (cf. Sect. 3.3). In this graph it is clearly visible that the width of SPP waveguides can be as wide as few micrometers when the layer thickness is not too high. Nevertheless, to achieve single mode guiding for every waveguide height, it has only to be smaller than 350 nm. Thus this width was used for all dielectric-loaded SPP waveguides.

A	B	AND		A	B	OR		A	B	XOR
0	0	0		0	0	0		0	0	0
1	0	0		1	0	1		1	0	1
0	1	0		0	1	1		0	1	1
1	1	1		1	1	1		1	1	0

(a)   (b)   (c)

A	NOT
0	1
1	0

(d)

Figure 2.10: **(a)** Truth table for an AND, **(b)** OR, **(c)** XOR, and **(d)** NOT gate, in Boolean algebra respectively. The input states are in the columns labelled "A" and "B" and the output state in the column labelled with the gate name.

In the case of the ARROW waveguide, the structural dimensions for single mode operation were evaluated directly with the finite element method.

2.7.3 Finite-Difference Time-Domain simulations

To correlate the experimentally obtained intensity patterns of propagating SPP modes in complex waveguide structures to theoretic values, finite-difference time-domain (FDTD) simulations [70–72] were carried out.

These numerical calculations are comparable to the finite element method. The structure is modelled in a suitable environment and also divided into several unit cells. The Maxwell-equations are then solved for every unit cell and their boundaries, while again the continuity condition for parallel components of the electric and magnetic fields and the perpendicular components of the electric and magnetic flux densities has to be satisfied.

2.7.4 Logic gates

A major part of this thesis deals with the possibility to process plasmonic signals within dielectric structures. Logic gates were chosen as processing devices. This is because they are already the building blocks of today's digital signal processing with electronics [26].

Logic gates are devices that generally connect the *true* or *false* states of two inputs with the *true* or *false* state of one output. More generally, *true* or *false* are 1 or 0. In this case, different connections of these states can be described with Boolean algebra [73]. This connects the state of the output with three basic operations between both inputs: The conjunction, the disjunction and the negation. These are logic AND, OR and NOT operations respectively. The connection can depicted in tables where the states of both input and the resulting state of the output is shown. These tables are called truth tables. They are shown for the case of the AND, OR and NOT operations in Fig. 2.10. It can be seen in Fig. 2.10(a) that the AND gate (the conjunction) delivers a 1 state at the output

A	B	c (AND)	s (XOR)
0	0	0	0
1	0	0	1
0	1	0	1
1	1	1	0

Figure 2.11: Truth table of a half-adder, consisting of one AND and one XOR gate.

only for the case that both inputs are at a 1 state. This is different for the OR gate (the disjunction) shown in Fig. 2.10(b), where only one 1 state at the inputs is enough to deliver a 1 state at the output. The exclusive disjunction is shown as XOR gate in Fig. 2.10(c), where the output is only in a 1 state when only one input gives a 1 state. The NOT gate (the negation) in Fig. 2.10(d) delivers the simple inverse of the input state to the output.

2.7.5   Half-Adder

To show the cascadability of these devices, a half-adder [26] was chosen where one AND and one XOR gate are connected. A half-adder adds the amount of inputs with a 1 state and delivers their sum as binary number at the outputs, which are named sum (s) and carry (c). The respective truth table is shown in Fig. 2.11.

However, it has to be mentioned that the Boolean algebra connects states expressed in 1 and 0. Nevertheless it can be applied for *true* and *false* states as well. The *true* and *false* states of the actual intensity in the logic devices discussed later in Sect. 4.3.2 will be named as *on* and *off* states for better readability. Furthermore, the actual intensity in the logic devices suffers from propagation losses and is therefore much lower at the outputs than at the inputs. This can be neglected however, since the signal contrast of *on* and *off* states can be arbitrarily chosen to any value that is actually measurable and even in today's electronics the signal levels are also maintained with input and output stages, not with the actual processing device [26].

Experimental methods for fabrication of plasmonic systems and their investigation by leakage radiation microscopy
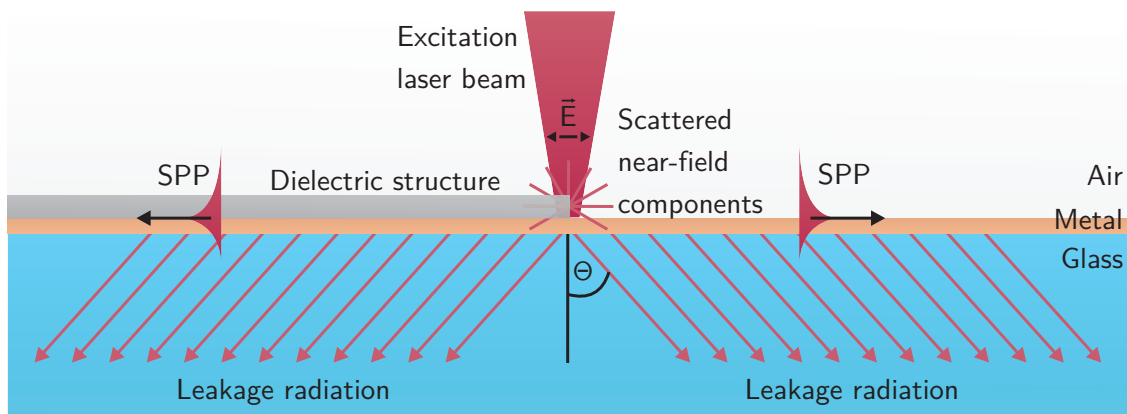

Figure 3.1: General schematic diagram of the investigated structures. A standard microscopic cover glass is coated with a thin layer of metal. Dielectric structures are generated lithographically on top of the metal. SPPs are then excited via focusing a p-polarised laser beam on the edge of the structure. They can propagate either confined within the dielectric structure, as depicted on the left side, or unconfined at the metal/air interface. While propagating, the SPPs can couple to leakage radiation modes in the glass. The angle θ of the leakage radiation is defined by the effective index of the propagating SPPs (cf. Eq. 2.6).

All the investigated structures in this thesis consist in principle of the same system: dielectric structures with sub wavelength dimensions on thin metal films over standard microscopic cover glasses. This system, along with the leakage radiation as the main physical phenomenon, used for investigation of the SPPs, is depicted in Fig. 3.1. The following chapter will introduce the used technologies to generate the metal films, as well as a newly developed process to generate the desired sub wavelength structures. For investigation of the SPPs, leakage radiation microscopy was used. To adapt this well known approach to the actual needs for evaluation of the samples, it was extended with a Michelson interferometer for spatial and temporal adjustment of the excitation laser spots

and a Mach Zehnder interferometer to enable time and phase resolved imaging.

3.1 Fabrication of thin layers

As explained before, this thesis concern SPPs, which are propagating on thin metal films whether free or confined in suitable dielectric structures, which were fabricated lithographically from thin layers. Therefore there was the need to fabricate thin metal films and thin dielectric layers within the scope of this thesis.

3.1.1 Spin coating

The dielectric layers can be easily generated via spin coating. In this technique the dielectric is dissolved in a solvent. The sample to be coated is fixed on a rotating chuck, and the liquid containing the dielectric material is pipetted onto the sample. Then the chuck is set to rotate, spinning off the excess liquid while the solvent evaporates. Thus, a thin film of the dielectric material will remain on the sample, where the thickness is defined by the rotation speed and viscosity of the initial liquid [74]. After spin coating the sample can be pre baked on a hot plate to evaporate residue solvent and improve adhesion of the layer.

3.1.2 Coating of metal layers

The metal coating of glass is a well established process [75]. In this thesis, two techniques were used: sputtering and thermal evaporation. In both processes, the object to be coated is placed within a hermetically sealed chamber which was then evacuated.

Sputtering

In a sputtering process, the evacuated chamber is filled with a process gas, normally a noble gas, in which a radio frequency (RF) field lights an ion plasma. The ion plasma ejects material through a collision cascade from a target, in this case gold, which is then deposited on the sample. The growing rate of the deposition can be determined with the remaining pressure in the chamber and the parameters of the RF field [75].

Thermal evaporation

In a thermal evaporation process, the process chamber is evacuated to a remaining pressure in the range of $10^{-4}-10^{-6}\,\mathrm{Pa}$. Metal, placed in a crucible, is then heated to its boiling point. Thus the metal will evaporate into the evacuated chamber and condense on the sample. In this process the deposition rates are mainly set by the temperature of the liquid metal [75].

The actual yielded layer thicknesses after the coating processes were verified with measuring the transmission spectrum of the layers and fitting this to the calculated transmission of the TMM, as described in Chap. 2.3.

3.2 Fabrication of dielectric structures for SPP waveguiding and excitation

Already established techniques for the fabrication of sub wavelength structures consist mainly of lithographic approaches. In these processes, thin polymer layers are treated either with deep ultra violet radiation or particle beams as electron or ion beams. These techniques already reach resolutions below 5 nm [76]. But the processes are very complex and the machines can easily cost 100 M€ [77]. In addition, the mask has to be generated vie electron- or ion beam scanning, a very expensive process [77]. For small lot sizes, manufacturers offer the possibility to acquire wafer space on "multi project wafers". There, individual processed blocks already cost a few tens of thousands of Euros [78]. On the other hand, there are very cost efficient approaches with proximity mask lithography at optical wavelengths. But in these processes, the masks used only reach resolutions on the micrometer scale [79]. Cost efficient systems, enabling flexible generation of sub wavelength structures are therefore still unavailable.

To overcome this gap, one area of this thesis was to take part in the development of a new projection lithographic process. This technology engages a standard microscope to project masks from the image plane to the object plane of the microscope objectives. Proof of principles of this technology were already reported by Kawata et al. [80] and, later, Love et al. [81], offering structural sizes down to 200 nm.

Two experimental contributions of this thesis for this new process were the cost efficient fabrication of projection masks needed and an evaluation of the influence of the quality of the used microscope objective.

3.2.1 Microscope projection photolithography

The general process of this developed approach is to create the required structures on a computer and print their black-and-white image onto polymer transparencies. These were then projected with 10 times demagnification onto intermediate chromium photo masks, which were, in turn, used as mask in the microscope based projection photolithography device, to generate structures with sizes regarding the demagnification of the used microscope objective.

First demagnification step

The optical demagnification of the transparencies, as illustrated in Fig. 3.2(a), was performed using illumination at a wavelength of 407 nm from a high-power LED source. The structures were imaged onto a chromium-covered BK7 glass substrate with 25 mm diameter and 1 mm thickness which was coated with positive-tone photoresist. After illumination, the photoresist was developed, where the illuminated areas were dissolved in an aqueous basic solution. The chromium layer with a thickness of 100 nm was subsequently etched, producing the intermediate mask. A further lens was placed behind the projection
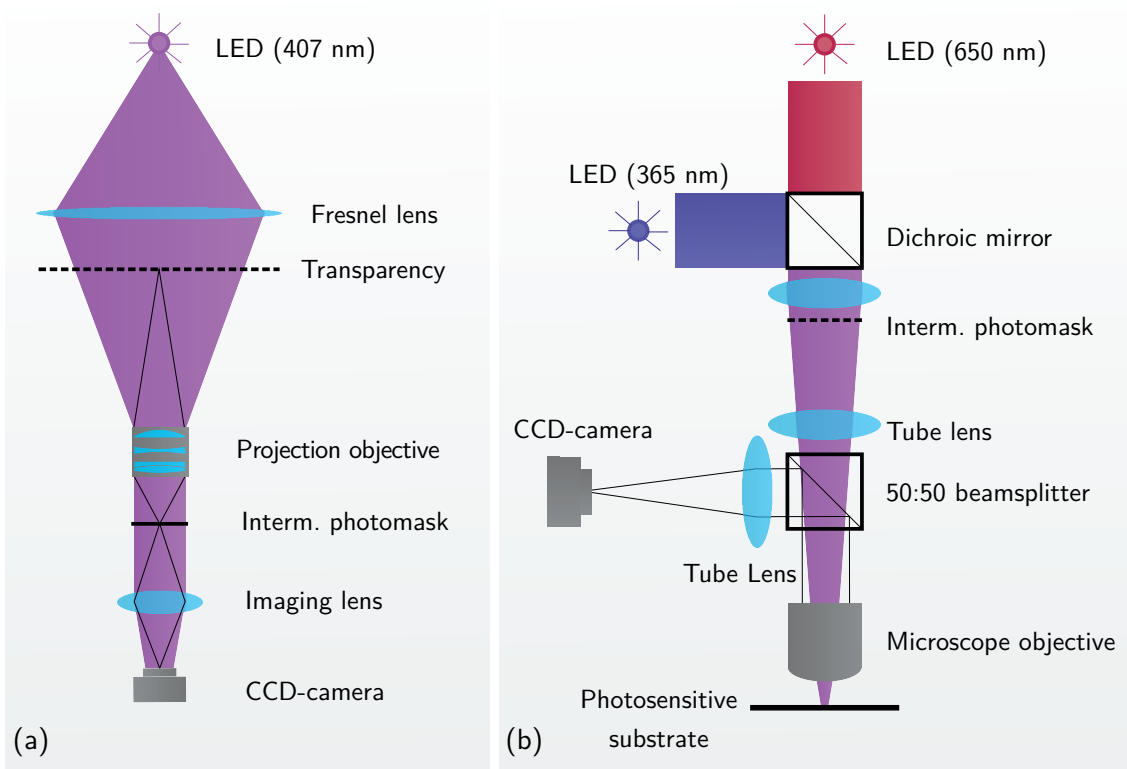
Figure 3.2: Schemes of both demagnification steps employed in the developed projection lithography process: **(a)** An illumination of a 407 nm high-power LED was used to demagnify printed transparencies onto intermediate photomasks, consisting of chromium-covered glass substrate with 25 mm diameter and 1 mm thickness which was coated with photoresist. After developing the resist, the chromium layer could be etched and the mask placed in the image plane of a microscope objective in the second demagnification step **(b)**. The demagnified image was projected onto a photosensitive monomer layer with UV radiation of a 365 nm high-power UV LED, initiating a polymerization process on the substrate. Both setups were equipped with CCD-cameras for proper focusing of the projected image. The optical imaging paths are depicted by black lines in the schemes.

plane, to image it directly onto a camera, enabling proper focusing.

Printed transparencies   Two approaches were used for the fabrication of the printed transparencies: first, a standard inkjet printer (Canon PIXMA iP4850 with nominally b/w printing-resolution of $600\,\mathrm{dpi} = 42.33\,\mathrm{\mu m}$), printing the images on standard A4 copy transparencies. In the second approach, a high resolution laser plotter (Bungard Filmstar-PLUS with nominally b/w plotting-resolution of $16\,256\,\mathrm{dpi} = 1.56\,\mathrm{\mu m}$) plotted the structures into photosensitive silver layers, embedded in polymer transparencies. The difference of both approaches were the achieved resolution of the printed structures.

To measure this, lines from 10–$1000\,\mathrm{\mu m}$ were printed and their actual width w_{print} measured and compared to the design widths w_{design}. As derived in these measurements, shown in Fig. 3.3(a), the inkjet printer was capable of printing ink droplets in a grid
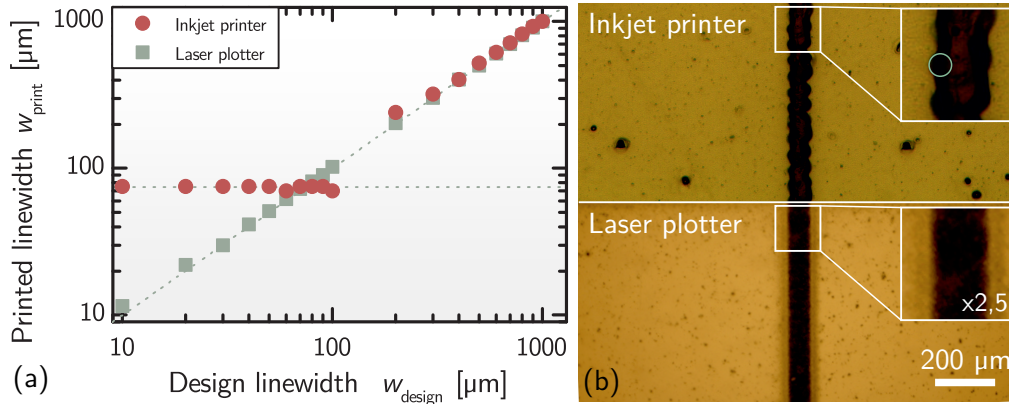
Figure 3.3: **(a)**Lines from 10–1000 µm were created in a vector graphics program and printed with an inkjet printer and laser plotter, respectively. The resulting line widths w_{print} were measured and plotted versus the design line widths w_{design}. It can be seen that the inkjet printer is only able of printing lines down to a width of 75 µm (horizontal dotted line) and a perfect correlation of designed and printed line widths starts only from 300 µm (diagonal dotted line). However, the laser plotter shows a linear behaviour over the whole range of the printed structures. **(b)** Microscope image of the smallest achievable line width of 75 µm from the inkjet printer, and its laser plotter counterpart. The actual inkjet droplet size is depicted by a green circle.

with minimum line widths of 75 µm and doing this for set line widths up to 100 µm. Furthermore, as depicted with a green circle in the upper part of Fig. 3.3(b), the size of each individual ink droplet was about 30–40 µm. Where the structural dimensions on the printed transparencies correspond perfectly with the design, this yields in an overall minimum feature size of 300 µm. Assuming a subsequent 10 x and 100 x demagnification in both lithographic steps, this already yields features of 300 nm in the final structures. Although this is sufficient to fabricate straight waveguides in dimensions, suitable for single-mode guiding of SPPs (cf. Chap. 2.7), bent waveguides were hardly achievable at all. The laser plotter, in turn, was able to fabricate structures with feature sizes down to 10 µm, yielding in theoretical sizes of 10 nm for the final structures. This is about one magnitude smaller than the diffraction limit, and thus could not be imaged. Hence, in this case, the minimum feature sizes were only determined by the imaging capabilities of the microscope objectives used.

Projection lens One aspect of the 10:1 demagnifier used was the scope of a cost efficient setup, while still maintaining appropriate optical properties. This implies that aberrations along with the costs of the lens system should be minimized. Since only one wavelength was used for irradiation, chromatic aberrations could be neglected. The simplest way to avoid the spherical aberrations is the use of an aspheric lens [82]. But to avoid field curvature, a multi lens systems has to be considered [82]. Since the cost of such a system depends to a great extent on the quantity and shape of the lenses used, the multi lens system should preferably consist of only very few lenses. A very good lens quantity to imaging
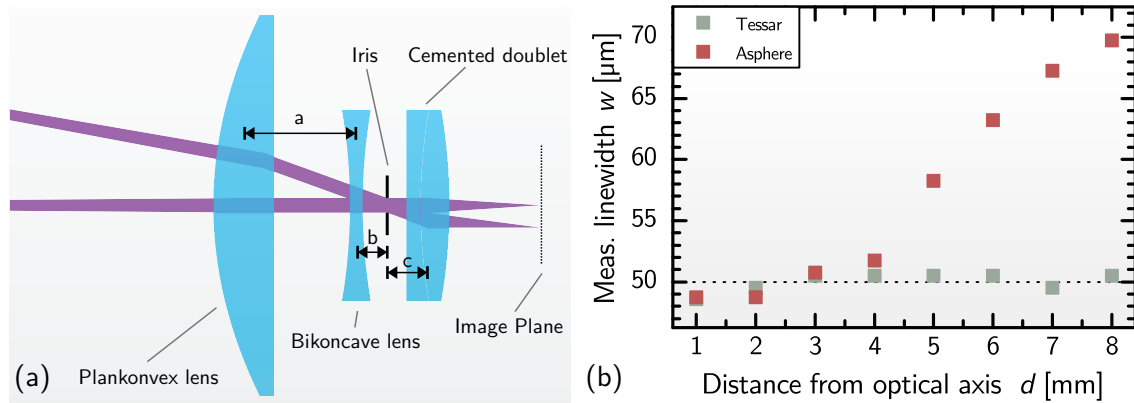
Figure 3.4: **(a)** Scheme of the home-assembled Tessar. The first lens is 2" spherical planoconvex with focal length of 75 mm, the second lens is 1" spherical biconcave with -50 mm focal length and the third lens is a 1" cemented doublet with a focal length of 40 mm. The distances a, b and c were 21 mm, 5 mm and 10 mm respectively. **(b)** Line width of an exposed test pattern in a photoresist exposed by a projection with an aspheric lens and the Tessar objective. It is clearly evident that due to the field curvature, the aspheric lens generates larger structures than a home-assembled Tessar objective for distances larger than 4 mm from the optical axis. This implies a much larger usable field of view for the Tessar objective. For eye-guidance a dotted line was added at the design line width.

performance ratio is given by a Tessar objective [82]. One key advantage in this context is that it can be assembled with standard spherical lenses and still offer very good imaging properties. For this reason, a Tessar with a demagnification ratio of 10:1 was assembled. The parameters of this objective were found by optimising them empirically with the lens design software WinLens3D Basic from Qioptiq. To achieve this, the transverse ray plot and the spot diagram were observed while changing the parameters, to minimize the ray displacement in the focal plane. The resulting parameters and a scheme of the objective can be found in Fig. 3.4(a).

To evaluate the performance of the home-assembled Tessar in comparison with an aspherical lens, a transparency with a grid of 0.5 mm thick lines, placed every 10 mm over the whole field of view, was projected with both lenses demagnified 10:1 onto a photoresist. The exposed resist was then developed and the resulting line width w measured. The result of this measurement is plotted in Fig. 3.4(b), where it is clearly visible that for lines fabricated with the aspheric lens the linewidth increases with the distance from the optical axis d. The reason for this behaviour is the field curvature, which is not corrected on the aspheric lens. The home-made Tessar objective, on the other hand, fabricates lines width with a maximum of about 1 % difference from the original structure width. However, discrepancies in this order can also be due to the exposure and development steps of the photoresist. Thus it was not expected that more sophisticated optimization or using more specialized lenses would lead to a significant enhancement of the fabrication accuracy.

Second demagnification step

In the second step, the intermediate mask was finally imaged onto a layer of photo processable dielectric material, which was the organic-inorganic hybrid photosensitive low shrinkage polymer Ormosil [83]. It has a refractive index of $n = 1.52$ in the near-infrared spectrum and is highly transparent in the optical and near-infrared range. This final demagnification was experimentally realized as shown in Fig. 3.2(b). The intermediate mask was placed in the image plane of a microscope, consisting of a microscope objective and the respective tube lens. The demagnified image, projected onto the Ormosil layer with UV radiation of a 365 nm high-power UV LED, initiated a local polymerization process. After development of the sample in isopropanol, the cross-linked material remained on the substrate, whereas the unilluminated material was rinsed out. To visualize and focus the projection of the intermediate mask, a 650 nm high-power LED was added to the setup and the projection was imaged onto the camera via a beamsplitter cube between the objective and the tube lens (the infinity space of the microscope).

Microscope objectives   The most important, though also the most expensive, part of the microscope projection photolithography (MPP) setup is the microscope objective used. To investigate the influence of its quality, one high precision objective from Carl Zeiss (100 x, 1.4 NA, see appendix A.3.1) and one more economic objective from Müller Optronics (100 x, 1.25 NA, see appendix A.3.2) were compared. Both objectives were marked as "Plan" by the manufacturers, signifying that the field curvature is minimized in both objectives. Since monochromatic light was used for polymerisation, the chromatic aberration of the objectives could be neglected.

Both objectives were installed in the MPP and different wide lines, varying in 25 nm steps from 75 nm to 975 nm, were fabricated on the sample. These structures are shown in Fig. 3.5(a), where it can be seen that the Zeiss objective was able to image lines down to nominal 75 nm, whereas the Müller objective was only capable of imaging lines with a width of 100 nm. Furthermore, it can be seen that the bigger lines fabricated with the Müller objective display larger widths than the nominal value. This is due to the relation between the amount of projected light and the structure size, which is considerably better in the case of the Zeiss objective.

Measuring the actual widths of the lines reveals, that the smallest line projected with the Zeiss objective is 85 nm wide on average, but this width varies considerably. Lines with widths above 100 nm are imaged very well with both objectives (cf. Fig. 3.5(b)).

In Fig. 3.6 grids with 500 nm ridge and groove width and a side length of 100 µm are shown. When the grid is fabricated with the Müller objective, a small defocussed area in the lower right edge is obtained, which is due to the remaining field curvature. This leads to a slightly smaller usable field of view for the Müller objective.

In conclusion, the Zeiss objective offers better imaging capabilities and the greater field of view. However, depending on the actual accuracy requirements of the current process it has to be assessed whether this benefit is in a suitable relation to the higher costs.
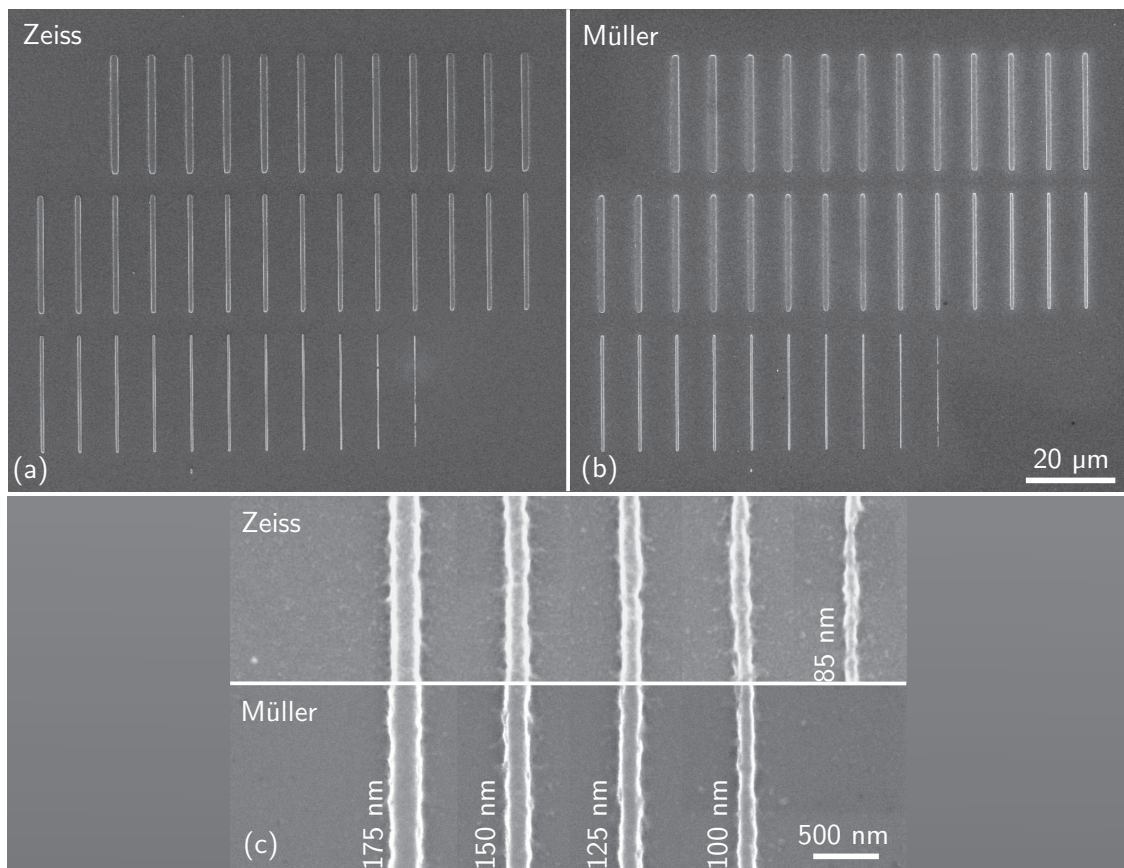
Figure 3.5: **(a)**/**(b)** Structures with widths from 75 nm to 975 nm in steps of 25 nm. The microscope objectives used were from Zeiss (a) and Müller Optronics (b), respectively. **(c)** Close up of the smallest achivable line width. The Zeiss objective was able to generate lines down to 85 nm (the nominal value on the mask was 75 nm), but with high variability, whereas the Müller objective was only capable of fabricating lines with widths greater than 100 nm. The actual line width corresponds well to the nominal value for widths above 100 nm.
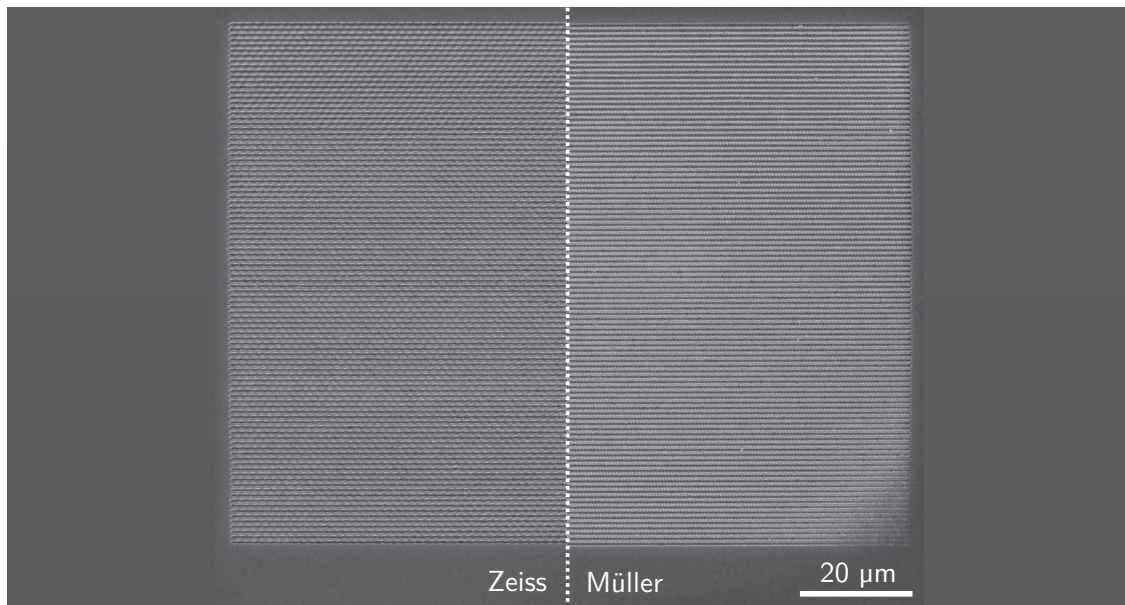
Figure 3.6: A grid with ridge and groove widths of 500 nm and side lengths of 100 µm, fabricated with the Zeiss (left) and Müller objective (right), respectively. On the lower right edge of the grid from the Müller objective, a defocusing due to the remaining field curvature of the objective is visible, reducing the effectively usable field of view for this objective.
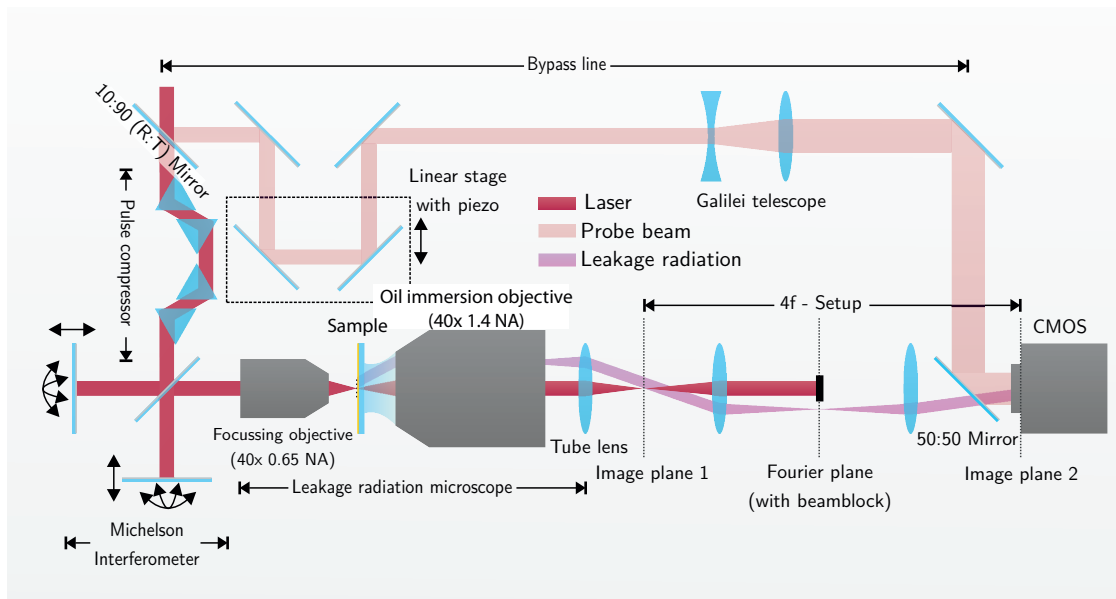
Figure 3.7: Scheme of the leakage radiation microscope with probe beam for phase resolved measurements: 10 % of the laser intensity is coupled into a bypass line before being precompressed. Precompression of the pulses was only performed in mode-locked operation of the laser source to prevent pulse spreading effects. Behind the prism pairs, the laser beam was coupled into a Michelson interferometer enabling spatial and temporal adjustment of the laser beam before being focused on the sample to excite SPPs. The propagating surface plasmon-polaritons radiate leakage radiation into the substrate which is collected with an oil immersion microscope objective (the magnification factor could be set to 40, 63, and 100 x). By means of a $4f$-setup, the excitation laser can be blocked before being imaged onto a CMOS camera. Furthermore it enables direct measurement of the angle of the leakage radiation and therefore the effective index of the propagating SPPs. The probe beam in the bypass line passes a pair of mirrors, mounted on a linear stage for adjusting the optical path length, and is coupled back into the original beam path in front of the CMOS. Thus, the probe beam and the leakage radiation will interfere directly on the CMOS.

3.3   Leakage radiation microscope

The investigation of the structures was performed with leakage radiation microscopy (LRM). The basic technique is well known and thus described in adequate detail in scientific literature [13, 43, 84–87].

As already introduced in Sect. 2.2, SPPs propagating on an air/metal interface can couple leakage radiation (LR) to substrates with higher refractive index. The angle of this radiation is larger than the angle of total internal reflection of the substrate. Thus, as can be seen in Fig. 3.7, immersion oil microscope objectives were used to image the structures and the leakage radiation simultaneously. This yields standard microscope images in which the propagating SPPs are visible. For this purpose, a CMOS camera was placed in the image plane of the microscope. The excitation of SPPs was performed
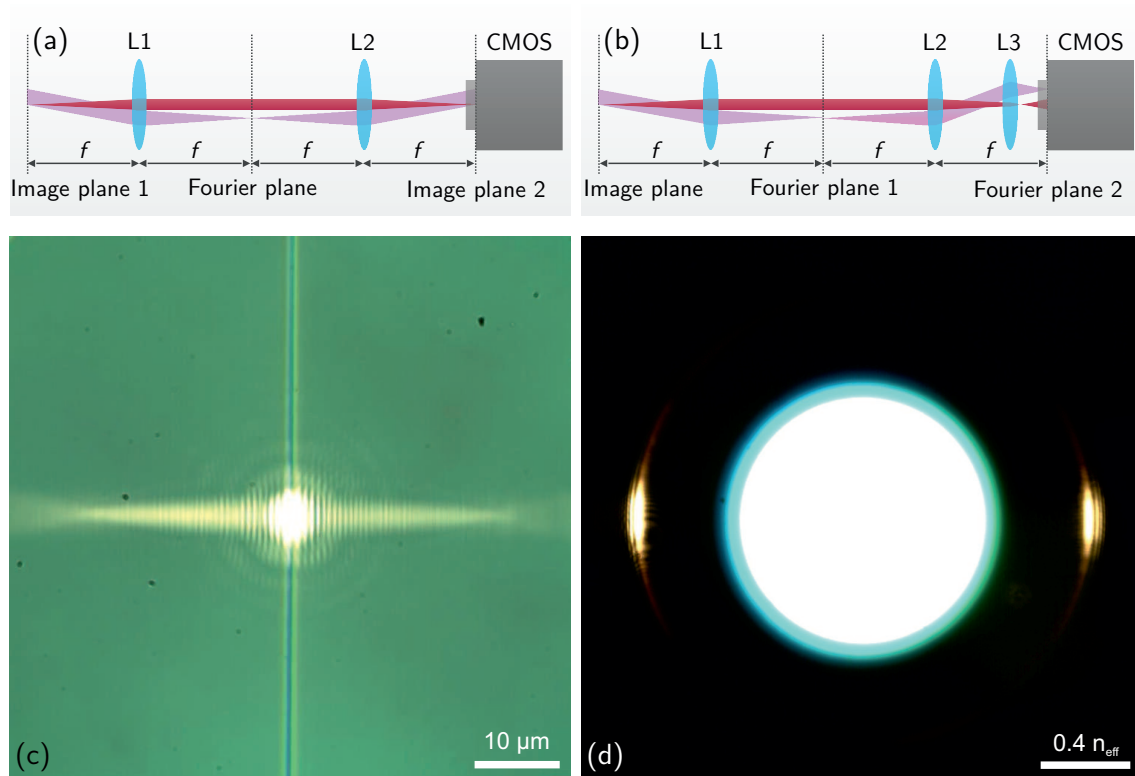
Figure 3.8: Sketch of the $4f$ imaging system with **(a)** and without **(b)** third lens, imaging the image plane **(c)** or Fourier plane **(d)**, respectively. The SPPs were excited by focusing a p-polarised laser beam on a thin dielectric ridge. While the real image from the image plane shows the excitation ridge, the exciting laser spot and the propagating SPPs, the Fourier plane shows a bright overexposed circle in the middle and two fringes left and right of the circle. The bright circle origins from the bright field illumination, where the outer boundary correlates with the numerical aperture (and thus the maximum possible focusing angle) of the focusing lens. The two fringes originate from the leakage radiation of the propagating SPPs and can be correlated to the respective angle and therefore to the effective index of the SPPs.

by focusing a p-polarised laser beam using an aspheric lens with 4 mm focal length and numerical aperture (NA) of 0.55, giving a diffraction limited focal spot diameter of 750 nm, onto sub wavelength structures as thin ridges or edges of SPP waveguides. To fulfil the requirements for proper investigation, several extensions had to be added to the basic setup, as will be discussed in the following sections.

An sample microscope image, recorded in the IP of the LRM is shown in Fig. 3.8(c). This image shows an extended gold film on top of a standard microscope cover glass. In the centre it can be seen that the laser used is directly focused on a dielectric ridge to excite SPPs. These are visible via their leakage radiation as a bright horizontal bar.
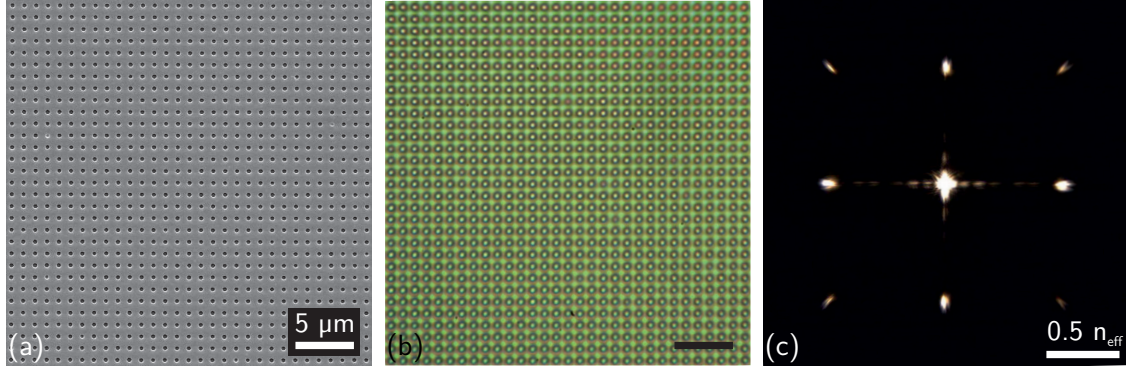
Figure 3.9: **(a)** Scanning electron microscope image of a two dimensional hole array with 1 µm grating constant d, fabricated with the MPP (cf. Sect. 3.2.1) in a photoresist on top of a standard microscope cover glass, with **(b)** its bright-field image in the LRM. **(c)** The resulting diffraction pattern in the Fourier plane of the LRM, when the hole array is irradiated homogeneously with a laser. This diffraction pattern can be correlated to the respective diffraction angles with Eq. 3.1, which in turn can be connected through Eq. 2.6 to the effective index of recorded LR in the LRM.

3.3.1 Optical Fourier transformation

As mentioned in Sect. 2.2, leakage radiation couples with a distinct angle into the substrate. A large amount of information can be deduced from this angle. To facilitate measuring it, a $4f$ imaging telescope was implemented. This consists of two additional lenses, relaying the *image plane (IP)* by a distance of twice the sum of both focal lengths, as is depicted in Fig. 3.8(a). Hence, when both lenses have the same focal length f, the total relaying distance is $4f$. The advantage of this method is that every light ray with the same angle to the optical axis is focused to the same spot in the focal plane (letter referred to as *Fourier plane (FP)*) lying $1f$ behind the first lens. This angular distribution resembles the optical Fourier transformation of the IP [43]. Since the angle of LR displays a Lorentz distribution around this distinct angle, LR appears as a bright fringe in the FP. This can be seen in Fig. 3.8(d), where the Fourier transformation recorded in the FP of a microscope image from the IP of an LRM (Fig. 3.8(c)) is shown. As described in Sect. 2.2 (especially Eq. 2.6, $k_{\mathsf{SPP}} = k_0\,n_{\mathrm{d}}\,\sin\theta_{\mathsf{SPP}} = k_0\,n_{\mathrm{eff}}$)), the angle of the leakage radiation – and thus the effective index of the SPPs – strongly depends on the thickness of the individual layers of the system investigated. Thus the thickness can be measured by evaluating the position of the bright fringes, originating from the LR, in the FP.

In addition, the NA of lenses or objectives is described by their maximum opening angle α by $\mathrm{NA} = n_{\mathrm{d}}\,\sin\left(\alpha\right)$ in a medium with refractive index n_{d}. In comparison with the effective index of SPPs, $n_{\mathrm{eff}} = n_{\mathrm{d}}\,\sin\left(\theta_{\mathsf{SPP}}\right)$, it can be seen that both quantities have the same scale in the FP. Since the bright-field illumination is focused by a lens with a distinct NA, implying a maximum angle of the focused light, the resulting light cone offers all angles between 0 and α. Therefore, bright-field illumination is focused in the FP to all points corresponding to angles between 0 and α. This is visible in the FP as a bright area.

The position of the edge of the area corresponds to the maximum opening angle α of the focusing lens used.

When a two dimensional diffraction grating is placed in the object plane of the microscope, the diffraction pattern will be imaged in the FP. Since the diffraction orders appear at angles α with

$$n \sin \alpha = \frac{\sqrt{m_x^2 + m_y^2} \, \lambda}{d}, \tag{3.1}$$

where m_i is the diffraction order in x and y direction, λ the wavelength, d the grating constant and n the refractive index, their distances to the zero order can be directly correlated to the respective angles. Thus, knowing the grating constant d, the FP can be calibrated. An exemplary two dimensional hole array with grating distance of $d = 1 \, \mu m$ is shown in Fig. 3.9(a) and Fig. 3.9(b) as a scanning electron microscope image and a bright-field microscope image directly from the LRM, respectively. The occurring diffraction pattern in the FP is shown in Fig. 3.9(c). For calibration of the FP, the visible diffraction orders were related to an angle via Eq. 3.1. If the angular metric is known for the FP, every point can be correlated to the effective index of propagating SPPs with Eq. 2.6.

3.3.2 Laser source

The laser is a titanium:sapphire oscillator, which could be set to operate in continuous wave or mode-locked operation. In the latter, about 10^5 modes were superposed yielding in a Gaussian distributed spectrum, set to 800 nm centre wavelength and 65 nm width, resulting in a Fourier-limited pulse duration of 13 fs. In this case, prism pairs were placed in front of the focusing objective in the LRM to prevent pulse spreading effects.
For cw operation, a wavelength of 800 nm was also chosen.

3.3.3 Michelson interferometer

In order to generate two phase-coupled Laser beams, eg. to excite two SPP modes inside different waveguides, two replicas of the laser beam were generated using a Michelson interferometer, as depicted in the lower left of Fig. 3.7. Both arms of the interferometer were equipped with waveplates and tiltable mirror mounts, enabling independent adaptable polarization states and spatial adjustment of both laser spots. The mirror mounts in turn were attached to translation axes for movement of the retro-reflecting mirrors parallel to the laser beam. This allows individual tuning of the optical path length of both arms and thus a time delay of the respective pulses. Optical path length difference will be referred to as phase delay φ for changes below the wavelength, which induces a time delay below one optical cycle, whereas it will be referred to as time delay σ for changes greater than the wavelength, i.e. one optical cycle. The spatial accuracy of the laser beam displacement was about 100 nm. A tuning resolution of a phase shift of $\pi/3$ could be achieved by iterative tuning of the optical path length while observing the response on the sample.
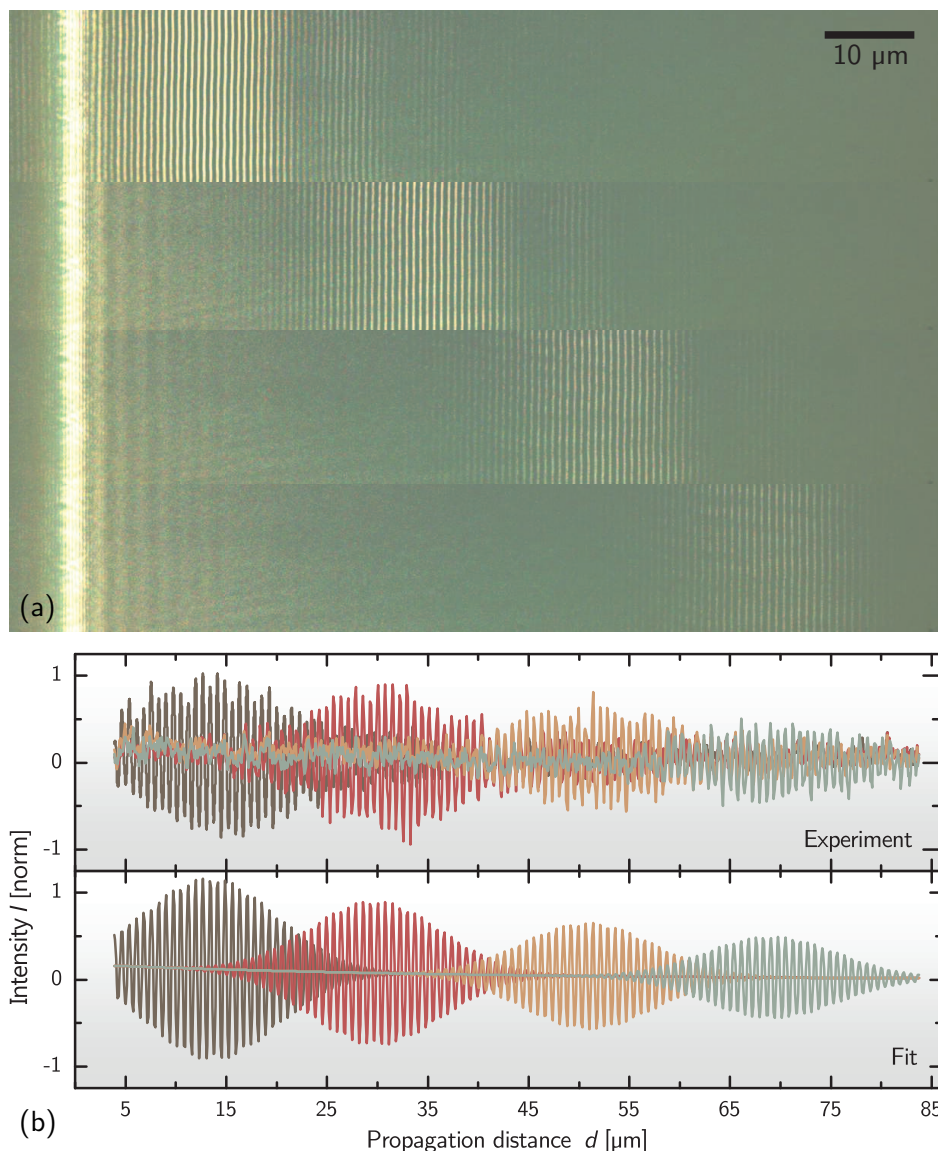
3.3.4 Time resolution

Figure 3.10: **(a)** LRM images of the interference from pulsed plane wave SPPs propagating on metal with an additional probe beam with four different probe times, corresponding to 30, 60, 90 and 120 V voltage at the piezo in the linear stage as depicted in Fig. 3.7. **(b)** Intensity profiles of the respective pulses (top) and their respective fits of Eq. 3.2 (bottom).

In order to allow phase and time resolved measurements, about 10 % of the beam intensity was coupled out to a Mach-Zehnder interferometer resembling a bypass line as a probe beam, before entering the LRM. The scheme of this technique is shown in the upper part of Fig. 3.7. The bypass offered the same optical path length as the LRM, including the 4 f-setup, and was coupled back into its beam path in front of the CMOS. For attenuation of the optical path length of the bypass line, two mirrors were mounted on a linear micrometer stage. The stage was equipped with a piezo actuator, which offered a

travelling distance of 41 µm yielding in a theoretically possible time delay of 273.5 fs. This setup offers a theoretical time resolution in the range of attoseconds for relative positioning over small distances compared to the overall travelling distance. But in practice however, the time resolution is limited by the magnification factor of the LRM, yielding in 32 nm per pixel on the CMOS. This means a time resolution of 0.1 fs for small travelling distances in one direction. A further mirror behind the linear stage in the bypass line enabled adjustment of the incident angle of the probe beam onto the CMOS, to fit it to the incident angle of the leakage radiation. For maintaining a homogeneous illumination of the whole CMOS, the probe beam was expanded with a Galilei telescope. In this configuration, the probe beam (PB) and the leakage radiation (LR) will interfere directly on the CMOS. Thus the recorded intensity resembles a time integrated superposition of the leakage radiation and the probe beam. This can be expressed as

$$I_{\mathrm{CMOS}}(x, z, t) \propto \int_0^{\tau_{\mathrm{fov}}} |E_{\mathrm{LR}}(x, z, t) + E_{\mathrm{PB}}(t)|^2 \, \mathrm{d}t \qquad (3.2)$$

where z is the SPP propagation direction and x is perpendicular to z. Because the exposure time of the CMOS is much longer than the SPP propagation time (τ_{SPP}) for the length of field of view (L_{fov}), $\tau_{\mathrm{SPP}} = L_{\mathrm{fov}}/c_{\mathrm{SPP}}$, the integral gives a time-average signal of the interference pattern.

For numerical calculations, the expressions for the respective electric fields, as introduced in Sect. 2.4, were first superposed as shown in Eq. 3.2. The square of the absolute values was than directly computed into three-dimensional (x, z, t) matrices, which were finally summarized over the time axis to conduct the time integration. This method has the advantage of utilizing the superior vector computation efficiencies of numPy (Python), Matlab or Octave [88, 89]. To conduct the calculations in this thesis, the programming language Python was chosen. As spatial steps of the matrices mentioned, the resolution of the experimental LR images taken was used. To calculate a sufficient length of the time steps, the Courant factor, normally applied at finite-difference time-domain simulations [90], was taken into account.

To demonstrate the functionality and capabilities of this method, four LRM images of ultrashort SPP plane wave pulses were recorded. For every image, the voltage of the piezo in the linear stage of the delay line (cf. Fig. 3.7) was adjusted to 30, 60, 90 and 120 V, respectively. Intensity profiles of the images were taken and fitted as described above. The images and both the experimental and the fitted intensity profiles are shown in Fig. 3.10. As a first estimate for the pulse duration, the bandwidth limited value was taken, which could be calculated from the spectral FWHM of 65 nm to be 13 fs. The group velocity was calculated from the semi-infinite approach to be $0.92 \cdot c_{\mathrm{vac}}$. The fitted pulse had a temporal FWHM of 45 fs, although this cannot be directly related to the actual pulse duration since the first-order autocorrelation function does not provide information for chirped pulses (cf. Sect. 2.6). The fitted group velocity was $(0.92 \cdot \pm 0.02) \cdot c_{\mathrm{vac}}$, which matches the calculated one perfectly.

Results and discussion of the investigation of free and confined plasmonic systems for the use as sensors and signal processing devices

The main focus of this work is the possibility of using dielectric structures for direct optical signal processing. As signal containing the information, the phase of propagating SPPs is used in the approach employed. Thus, this chapter will introduce two schemes to change the phase of SPPs due to changes of the condition to be detected. Additionally, it will address the Gouy phase shift, which is an inherent change of the phase of focused waves. Finally the signal processing dielectric waveguide structures will be introduced and discussed in addition to the ability to cascade single processing stages to more complex logic devices.

The chapter will be divided to discussing both free and confined propagating SPPs. First, phase changing effects of free SPPs as due to sensing information or the Gouy phase shift will be presented. Thereafter, a system which confines SPPs with a Bragg grating will be discussed, followed by the dielectric waveguide structures for the SPP signal processing.

4.1 Free propagating SPPs

As described in the theoretical part of this thesis, in Eq. 2.6, the propagation properties of SPPs are dependent on the media in the near vicinity. Changes to this media will lead to an alteration of the effective index n_{eff} of the propagation. Since $k_{\mathrm{SPP}} = k_0 \, n_{\mathrm{eff}}$, this will directly change the wavelength of the SPPs. Hence, when an SPP is split into two coherent parts and one part passes an area of altered effective index, it will show a relative phase shift, compared to the unaltered SPP. This phase shift can then be measured and related to the sensing information.

On the other hand, when waves in general are focused, or possess a caustic within their propagation, the finite spatial extinct in the caustic will lead to the phenomenon known as Gouy phase shift, where the focused beam will experience a longitudinal phase shift compared to a plane wave [59].
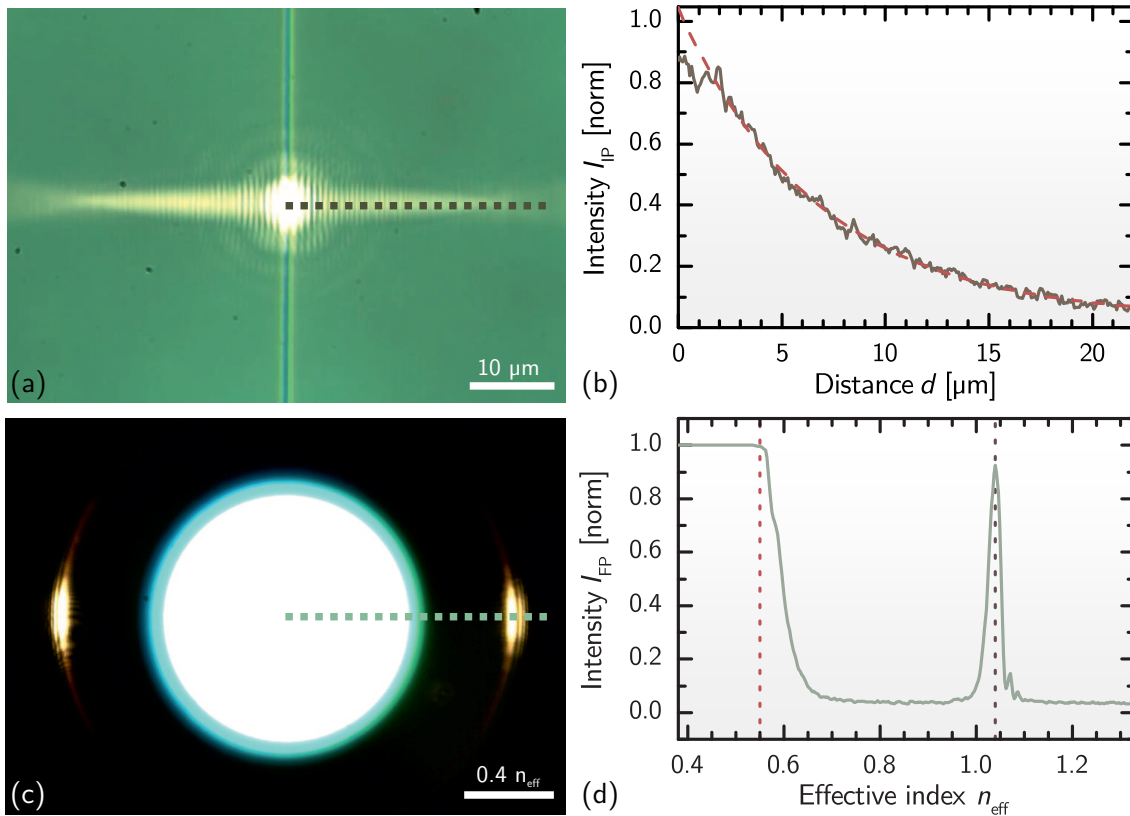
Figure 4.1: **(a)** bright-field image of a laser beam, focused onto a thin dielectric ridge beneath a thin gold film on a standard microscopic cover glass. The bright horizontal pattern is the trace of excited SPPs, imaged via their LR. **(b)** The corresponding intensity profile of the dotted line in Fig. (a) reveals the clear exponential decay of the SPP intensity during propagation, which has a propagation length of 6.8 µm, in this case. **(c)** The optical Fourier transformation of Fig. (a) (cf. Sect. 3.3.1). The light in the bright area in the centre originates from the bright-field illumination, focused with a lens with numerical aperture (NA) of 0.55 onto the sample. The fringes left and right from it stem from the LR and their position is related to the angle of the LR, which in turn is related to the effective index of the SPPs (cf. Sect. 2.2). **(d)** The corresponding intensity profile of the dotted line in (c), where the effective index of the propagating SPPs can be seen as a Lorentz shaped peak (depicted by the black dotted line), and the NA of the focusing objective is visible as the edge of the plateau (depicted by the red dotted line).

Both effects will be discussed in the following sections.

4.1.1 Effective index

A very easy approach to change the effective index of unconfined propagating SPPs on thin metal films is the coating of an additional film on top of the metal. Thus, the system already introduced consisting of glass, gold and a dielectric ridge was taken and spin coated with different layer thickness of PMMA.

The laser was then focused on top of the ridge to excite an SPP. The microscope image recorded in the LRM in this case is shown in Fig. 4.1(a). In this image, the focused laser
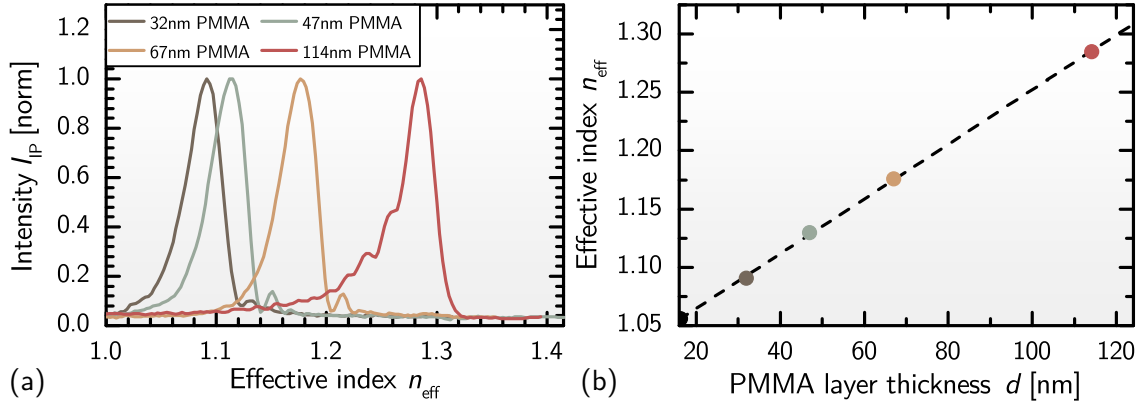
Figure 4.2: **(a)** Peaks in the FP for SPPs propagating on gold films with four PMMA layers of differing thicknesses on top. **(b)** Plot of the effective index of each peak position versus the PMMA layer thickness.

and propagating SPPs, and also the dielectric ridge for excitation of SPPs can be seen. In Fig. 4.1(b) is then shown that the intensity profile (taken at the dotted line) from the SPPs offer the expected exponential decay, depending on the propagation length (L_{SPP}). In this case $L_{\mathrm{SPP}} = 6.8\,\mu\mathrm{m}$. The optical Fourier transformation of this image is shown in Fig. 4.1(c), recorded in the FP of the LRM. In the FP, the bright-field illumination is focused to all points, corresponding to angles between 0 and the maximum opening angle α of the used focusing lens. This appears as the bright area in the centre of Fig. 4.1(c). The LR of the SPPs shows a Lorentz shaped angle distribution around θ_{SPP} (cf. Sect. 2.2), and is therefore focused to fringes in the FP. The intensity profile in Fig. 4.1(d) (taken at the dotted line in Fig. 4.1(c)), illustrates this very clearly. The SPP peak can be seen at an effective index of 1.04 (depicted with a black dotted line) and the NA of 0.55 from the focusing lens is visible as the edge of the saturated plateau at the black dotted line. As discussed in Sect. 3.3.1, the NA and the effective index of SPPs have the same scale in the FP images.

If now thin PMMA layers are spin coated on top of the system illustrated, the effective index of the SPPs increase. This becomes visible as a shift of the SPP peaks in the FP, shown in Fig. 4.2(a). This was performed with four different rotation speeds while spin coating, where the film thickness of the resulting PMMA layers was measured using the transmission spectrum and the transfer matrix method. When the effective index of the resulting SPP peak is plotted versus the respective PMMA layer thickness d, a clear linear dependency with a slope of $0.00235\,n_{\mathrm{eff}}/\mathrm{nm}$ is visible (Fig. 4.2(b)).

If it is assumed that the whole imageable NA of 1.4 of the microscope objective in the LRM is imaged on the field of view of the CMOS used, containing 2592 pixels, this already results in a sensitivity of $230\,\mathrm{pm/px}$. Therefore, this approach as demonstrated can already be used as very accurate method for determining the layer thickness of additional layers on top of plasmonic systems. Nevertheless, this way of the evaluation requires the LRM which is a rather bulky setup. How phase differences can be processed within the plasmonic system with small dielectric structures will be discussed in Sect. 4.3.1.
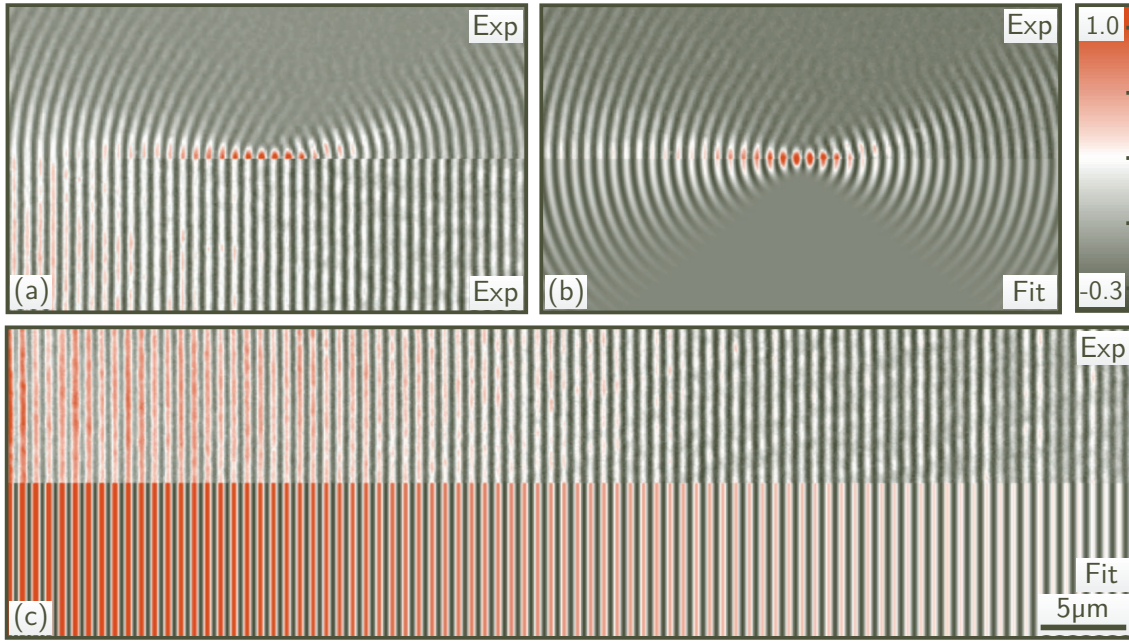
Figure 4.3: **(a)** Experimental demonstration of the spatially resolved two dimensional Gouy phase shift for SPPs. Leakage radiation images (labelled as 'Exp') for focused and plane wave SPPs are shown in the upper and lower sections, respectively. The phase resolution was achieved by interference with a probe laser beam. Regions of positive and negative interference are shown by red and olive-green. **(b)**/**(c)** Comparison of the experimentally obtained LRM images with numerical calculations, which are fitted to this experimental data (labelled as 'Fit') as discussed in Sect. 3.3.4.

4.1.2 Gouy phase shift

When waves are propagating freely as plane waves, the wave vector is very well defined by $k_{\text{wave}} = 2\pi/\lambda_{\text{wave}}$. On the other hand, this wave is mathematically defined with infinite extent, even though it might decrease due to absorption effects. This is consistent with the uncertainty relation $\Delta x \Delta k > p$ (in the case of SPPs $p = 1/2$ due to their two dimensional nature [59]). When the wave is now focused in any manner, the wave will be localised in the focus, yielding in a very well defined Δx. This causes Δk to be a distribution of certain wave vectors. In the case of defined waves, as in Gaussian beams, this can be derived mathematically. Feng and Winful stated that for Gaussian beams this distribution of wave vectors yield in a phase shift of $\pi/2$ in the focus and in the two dimensional case [59].

In the scope of this thesis, the Gouy phase shift was measured for the first time for SPPs systems at optical wavelengths. For the measurement, two phase resolved LRM images were taken, one for a plane wave and one for a focused wave. The SPPs were excited by focusing a laser beam on ridges as already described in Sect. 2.4. Phase resolution of the images was achieved by interference with an additional probe beam as described in Sect. 3.3.4. Both images were remapped to a new colour scale, visualizing the interference pattern from olive-green (negative) to red (positive). A comparison of these images is shown in 4.3(a). A perfect overlap of the wave fronts for the plane and focused SPP waves
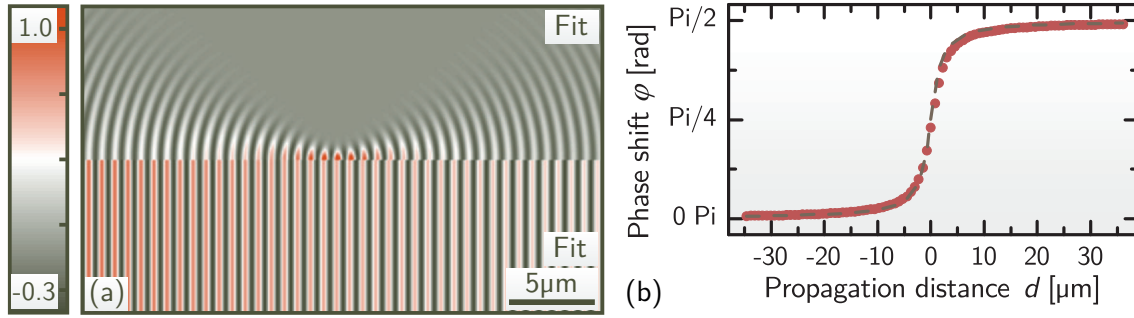
Figure 4.4: **(a)** Demonstration of the spatially resolved Gouy phase shift for SPPs, shown as a comparison of the fitted numerical interpolation of the plane and focused SPP beam, regarding to the fitting procedure explained in the text and shown in Fig. 4.3. **(b)** To phase shift converted distance of each respective wavefront maxima in Fig. (a) shown as red dots, overlayed by the theoretically expected arc tangent function as a black dotted line, as discussed in Sect. 3.3.4.

is clearly visible in front of the focus position. Behind the focus, the phase mismatch between the wave fronts corresponding to the Gouy phase shift can be observed.

Numerical calculations of Eq. 3.2 for plane SPP waves were fitted to the observed experimental interference pattern. As a fitting parameter, the complex SPP wave vector was used with an initial value given by the semi infinite approach and the Lorentz-Drude model for the dielectric function of the metal. The result of this fit is shown in Fig. 4.3(c) and demonstrates a perfect coincidence between the measured and fitted SPP plane waves. Since the numerical approach does not include terms for the beam curvature of the probe beam, the overlap between the experimental and fitted results for the whole field of view proves that beam curvature of the probe beam can be neglected. The determined SPP wave vector was further used for fitting of the experimental results for the focused SPP beam to the numerical calculations. In this case, the beam waist w_0 was the only fitting parameter. The comparison of the experimental and numerical result is shown in Fig. 4.3(b), where again a perfect conformity can be seen.

The Gouy phase shift was now determined by comparing the distances between the wave front maxima for the plane and focused SPP waves on the propagation axis, as can be found in the intersection of the upper and lower segment of Fig. 4.4(a). These distances were converted to the phase shifts in radians and are shown in Fig. 4.4(b) as red dots. The theoretically expected arc tangent function, see Eq. 2.10 in Sect. 2.4, with the Rayleigh length $z_R =1.5\,\mu m$ is shown as a dashed black curve. A perfect conformity between the measured and computed results can again be observed.
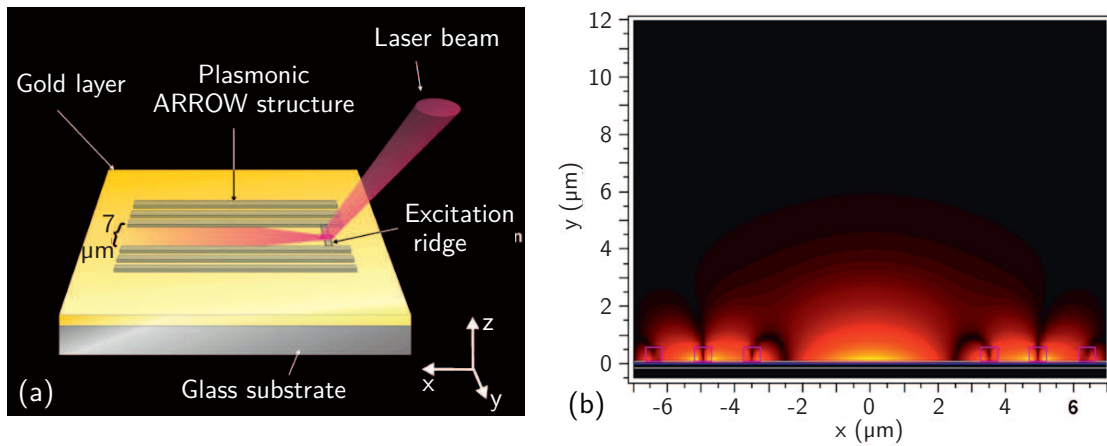
Figure 4.5: **(a)** Layout of the structure, confining SPPs with Bragg gratings by forming an ARROW like waveguide. **(b)** Mode profile in the near-infrared region of the structure mentioned.

4.2 Confinement with Bragg reflection

The results shown from free propagating SPPs have one common disadvantage: the short propagation length of only several micrometres. One approach to overcome this limitation is the confinement in special waveguide systems. This thesis contributed to the work[1] where dielectric ridges are employed to shape Bragg gratings, to create a plasmonic counterpart to an antiresonant-reflecting optical waveguide (ARROW) [65–67]. The ridges can be easily fabricated with the MPP introduced earlier. This approach is able to increase the propagation length by a factor of ten. Beside this, the scheme also offers the ability to directly access the electric field of the SPPs. However, there is the drawback that the structural dimension exceed several micrometers.

The overall composition of the structures is shown in Fig. 4.5(a). The basic system consists again of a thin gold layer over a standard microscope cover glass, on which dielectric structures were fabricated by means of the MPP. The structural dimensions were distinguished by FEM simulations to yield in single mode operation in the near-infrared region. Experimental measurements offer a propagation length of $43\,\mu$m for this ground mode [67]. As already shown in Sect. 4.1.1, a free propagating SPP in this system offers an effective index of $n_{\mathrm{SPP,free}} = 1.04$, whereas the confined mode in the ARROW waveguide offers a smaller effective index of $n_{\mathrm{SPP,wg}} = 1.01$ [67]. This is due to the confining principle: SPPs propagating on the metal surface are reflected by total internal reflection at the dielectric Bragg gratings with an angle θ, which has to be smaller than the critical angle for total internal reflection $\theta < \theta_{\mathrm{c}}$. The resulting waveguide mode is a superposition of the actual propagating waves. However, because of the intrinsic consistency, all existing waves must offer a phase difference of 0 or a multiple of $2\,\pi$. For the ground mode, this is

---

[1] [67] C. Reinhardt, A. B. Evlyukhin, W. Cheng, T. Birr, A. Markov, B. Ung, M. Skorobogatiy, and B. N. Chichkov, "Bandgap–confined large–mode waveguides for surface plasmon–polaritons," *Journal of the Optical Society of America B*, vol. 30, no. 11, p. 2898–2905, 2013.
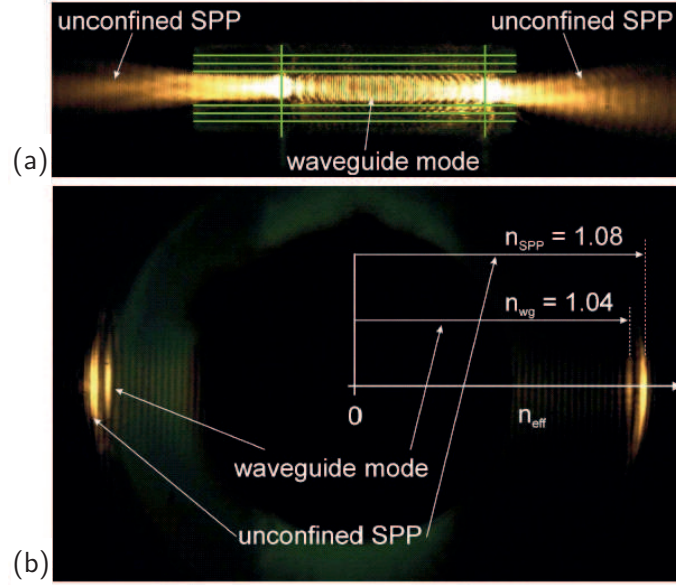
Figure 4.6: **(a)** LRM image of the ARROW structure, where the dielectric ridges are depicted by green lines. The structure was chosen to offer signals from both, the confined and unconfined SPPs. **(b)** Fourier plane of image (a), where the effective indices of the respective modes can be found.

only the case for waves propagating with an angle θ_{sm}. The resulting effective index of the ground mode is $n_{SPP,wg} = n_{SPP,free} \cos \theta_{sm}$ [64]. With this, the angle of the contributing waves can be calculated to be $13.80\,°$.

To demonstrate the sensing capabilities of this system, the same experiment as described in Sect. 4.1.1 was performed. An additional polymer layer with refractive index of 1.5 and $32\,$nm thickness was spin coated onto the whole sample. Then the LRM images shown in Fig. 4.6 were recorded, offering a clear signal for both the confined and the free propagating SPP modes. The effective indices are 1.04 and 1.08 respectively.

The difference of the effective index in the waveguide, caused by the additional polymer layer, is $\Delta n = 0.03$. The gain of the phase delay from a SPP mode while propagating the distance L, is $\Delta \varphi = k_0 \, \Delta n \, L$. This means it is $\Delta \varphi = 0.236\,$rad/µm in the considered system.

As will be discussed in Sect. 4.3, one scope of this thesis is the investigation of dielectric waveguide structures for direct processing of these phase delays within the plasmonic system. As will be shown, the signal contrast achievable in these devices was $13/\pi\,$dB/rad. With this signal contrast, a phase delay of $\Delta \varphi = 0.236\,$rad/µm implies an achievable gain of the signal contrast of $3\,$dB/µm per length of the ARROW waveguide sensing region.

If it is assumed that the ARROW waveguide would be covered with an idealized protein adlayer (as described in [16]), TMM calculations yield in $\Delta n_{protein} = 0.0035$. With respect to an assumed minimal measurable signal contrast of about $1\,$dB, this could already be recorded after $8.8\,$µm propagation distance.
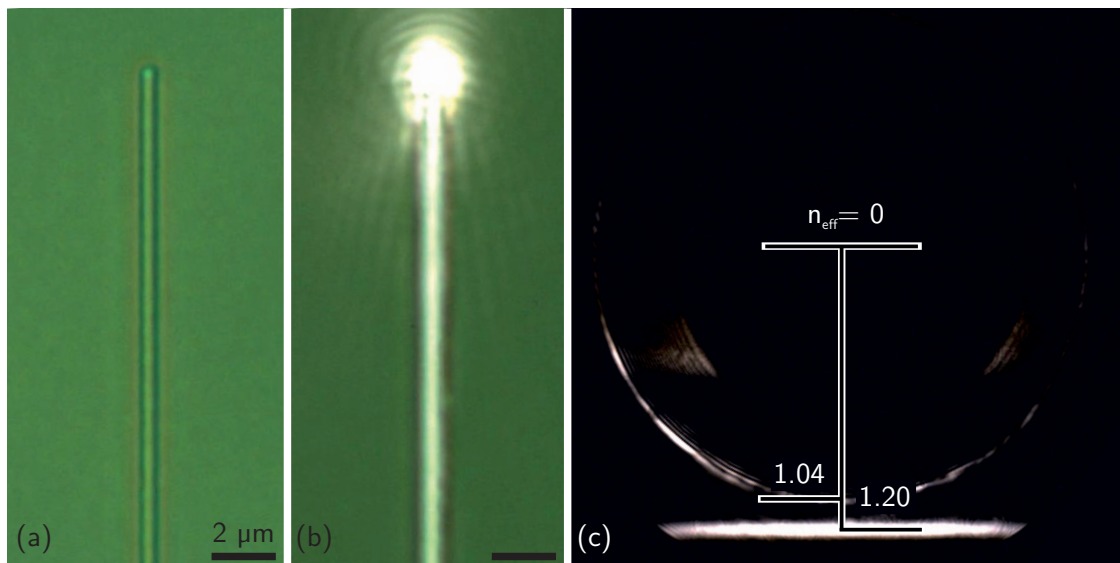
Figure 4.7: **(a)** Microscope image of a 350 nm wide, 300 nm high, dielectric ridge on top of a 50 nm thin gold layer. **(b)** The same waveguide with visible excited SPP mode within the waveguide structure. **(c)** The respective FP, where a pronounced fringe can be seen, originating from the LR of the guided SPP mode with $n_{\text{eff}} = 1.20$, and a circular intensity pattern with $n_{\text{eff}} = 1.04$, originating from free propagating SPPs. In this image, the bright-field irradiation is switched off and the excitation laser beam is blocked.

4.3   Confinement in dielectric waveguides

The approach of the ARROW waveguide described in the preceding chapter confined the SPPs to waveguide structures of several micrometers width. The advantage of this system is a longer propagation length and the accessibility of the electric field of the propagating SPPs, but with the drawback of rather large structures.

Another system to guide SPP waves is the use of dielectric-loaded waveguides. Here, dielectric ridges are placed directly on top of the thin metal layer and the SPPs are confined by the higher refractive index of the ridge [63, 64]. The advantage of this system is that the SPPs can be confined to dimensions below the wavelength, while the propagation length remains comparable to free propagating SPPs.

A demonstration of this system is shown in Fig. 4.7(a). A dielectric ridge was fabricated with the MPP directly on top of a thin metal layer over a microscope cover glass. A guided SPP mode was then excited by focusing a laser beam onto the edge of the waveguide structure, which is shown in Fig. 4.7(b). In Fig. 4.7(c), the respective Fourier plane is shown, where both a straight fringe, originating from the guided SPP mode, and a circular fringe from the free propagating SPPs, can be seen.

According to Eq. 2.14 in Sect. 2.7, the width and height of the ridge was set to be 350 nm and 300 nm, respectively, to achieve single mode guiding. The effective index obtained from FEM simulations is 1.21, which corresponds well with the fringe in Fig. 4.7(c), revealing an effective index of 1.20.
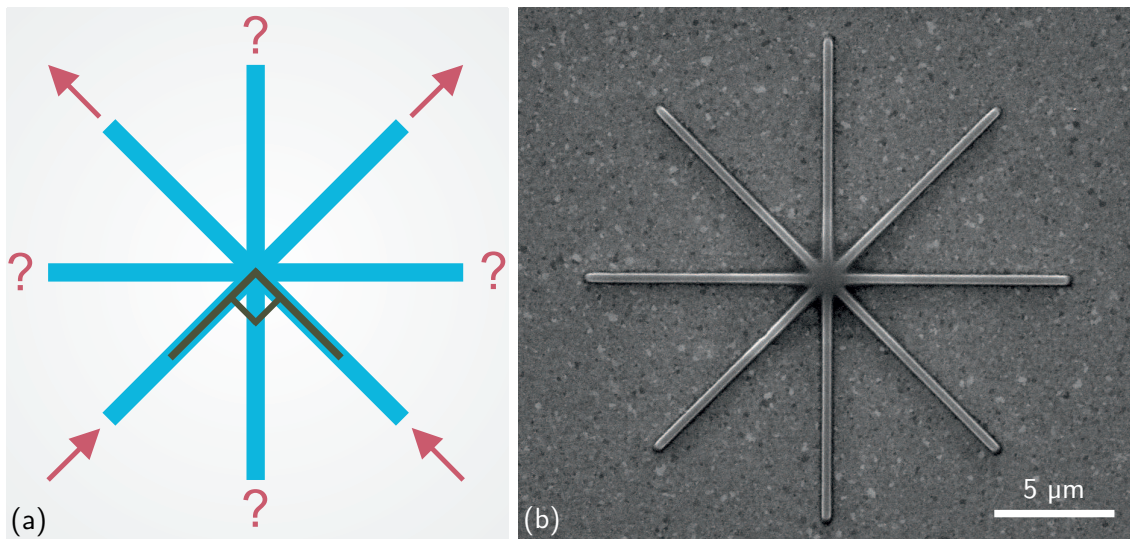
Figure 4.8: **(a)** Scheme of the structure shown, depicting the central question of how confined SPPs behave at junction points of waveguide systems when additional waveguides occur at the junction point. **(b)** Scanning electron microscope image of the multiple waveguide junction structure made from Ormosil on a thin gold layer over a standard microscopic cover glass. Every waveguide is 20 μm long, 350 nm wide and 300 nm high.

The measured propagation length is 10 μm. It must be said, that all dielectric waveguide systems shown in this thesis are not optimized for lowest possible losses but for best possible interpretability of the images made with the LRM system. Increasing the used wavelength (cf. Sect. 2.1 and Ref. [15]) or using thicker gold (cf. Ref. [91]) can enhance the propagation length drastically.

4.3.1 Crossed waveguides

One of the main goals of this thesis is the investigation of plasmonic signal processing with devices consisting of crossed waveguides, by using them as optical logic gates. To fulfil the requirements for logic gate operations, the proposed SPP devices should exhibit several basic properties as they are given in Ref. [92]. The most important conditions are cascadability, a fan-out (one logic or switching stage should provide enough output intensity to drive at least two new inputs) and avoidance of back-reflections of plasmonic signals into the input ports.

As depicted in Fig. 4.8(a), the first question in these investigations is what is happening in general when guided SPP modes are excited in two crossed dielectric ridges, while additional propagation directions are offered at the junction point by means of further waveguides.

Excitation of SPPs with two laser spots and induced switching effects

For this investigation, a star-like junction structure was generated with the MPP. A scanning electron microscope image of the resulting structure is shown in Fig. 4.8(b). The waveguides dimensions were chosen again to be 350 nm, to achieve single mode guiding in the structures, according to Sect. 2.7. As waveguide length, 20 μm was set.

For the evaluation of the behaviour of the propagating SPP modes at the junction point, they were excited at the left and right lower edges of the input waveguides, pointing diagonally upwards in the star like junction structure, as indicated in Fig. 4.9(a). Both excitation laser beams were separated by means of the Michelson interferometer as discussed in Sect. 3.3.3, enabling the tuning of the phase delay between both SPPs. The laser source was set to mode-locked operation, producing ultra short laser pulses, as described in Sect. 3.3.2.

Initially, SPP excitation in only one input waveguide was considered. At the waveguide junction, the SPPs from a single diagonal waveguide couple only to very weak extent into the horizontal waveguides, pointing to the left and to the right and in the vertical upward waveguide. This is demonstrated in Fig. 4.9(d), where only SPPs in the right upward directed input waveguide were excited. The preferred propagation of SPPs inside the waveguide is straight ahead along the diagonal direction of the input waveguide (see Fig. 4.9(d)). This straight propagation of the SPP mode is also the reason that no SPP back-reflection occurs, which will be discussed further in Sect. 4.3.1 of this work. Coupling of SPPs into the horizontal right and upward waveguides was found to be only at a very low extent.

The further obtainable intensity modulation in the vicinity of the junction point may be due to the ability of the SPP waveguide mode to couple into scattered light in the waveguide crossing. This scattered light can interfere with the leakage radiation causing the intensity modulations. The underlying effect was described by Hohenau et al. in detail in [44]. In addition, the abrupt change of refractive index at the waveguide ends causes reflections which are visible as modulations of the intensity at the waveguide ends. However, this reflected mode decays quickly and is not visible at the input ports.

When both diagonal input waveguides were excited, strong interference at the waveguide intersection point was observed when the two excited SPPs pulses perfectly overlapped in time (phase delay $|\varphi_A - \varphi_B| = 0$). The intensities of the two corresponding excitation laser beams in the Michelson interferometer were adjusted to equal values.

The variation of the phase of the excitation laser pulses in the Michelson interferometer resulted in variable interference patterns at the intersection. This in turn affects the intensity of the SPP mode excited in the upward waveguide (in the following referred to as output waveguide). LRM images of this effect are presented in Figs. 4.9(b) and 4.9(c), respectively.

When both SPPs are in phase (see Fig. 4.9(b)), interference in the intersection area leads to periodic field oscillations longitudinal to the straight upward and downward waveguides.
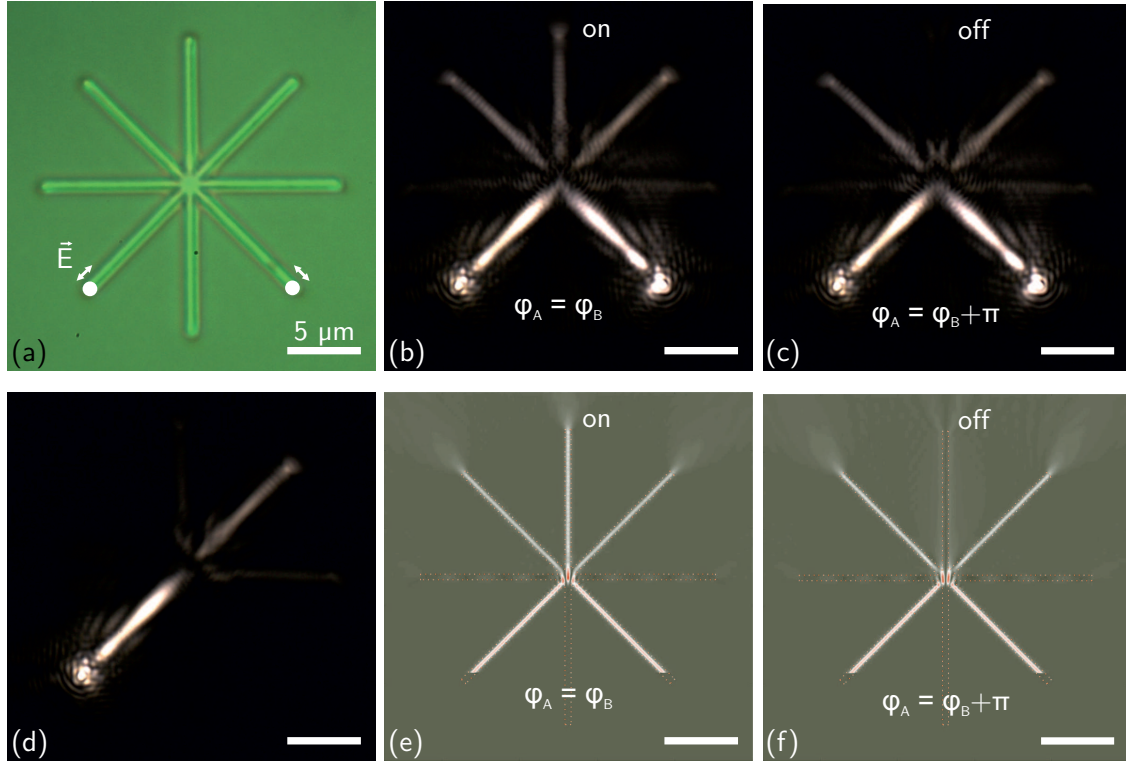
Figure 4.9: **(a)** Bright-field LRM image of the investigated waveguide structure on a thin gold layer coated standard microscopic cover glass. **(b-d)** Dark-field LRM images where in (d) SPP is excited at only one point and in (b,c) SPPs are excited coherently at two points with $0\,\pi$ phase shift (b) or $1\,\pi$ phase shift (c) between the exciting laser spots. **(e,f)** numerical FDTD simulated images, respectively.

Since the SPPs wave vectors in both input waveguides point diagonally upwards, energy coupling is better phase-matched into the output waveguide. No wave vector component points into the downward directions, therefore no SPP signal in the downward waveguide and no back-reflections into the input waveguides occur, as shown in Fig. 4.9(b).

Varying the relative phase now between SPPs such that the phase difference becomes equal to $1\,\pi$, the interference of the two modes leads to SPP field oscillations at the junction point which are perpendicular to the output waveguide. This signifies that no SPPs are excited into the upward and downward waveguides (see Fig. 4.9(c)).

The intensity contrast between the *on* and *off* states was found to be $13\,\mathrm{dB}$ in the LRM measurements. Numerical finite-difference time-domain (FDTD) simulations revealed a contrast value of $23\,\mathrm{dB}$ for ideal waveguides geometry. The difference between experimental and calculated results is due to the 8-bit limited dynamics of the CMOS camera in the LRM setup, resulting in a maximum dynamic range of 24 dB. Therefore even small amounts of scattered light can drastically reduce the measurable contrast.

In addition, for the *on* state, the signal intensity at the output waveguide exit is only $1.5\,\mathrm{dB}$ lower than the signal intensity at the exit ends of the input waveguides, both in experiments and in simulations.
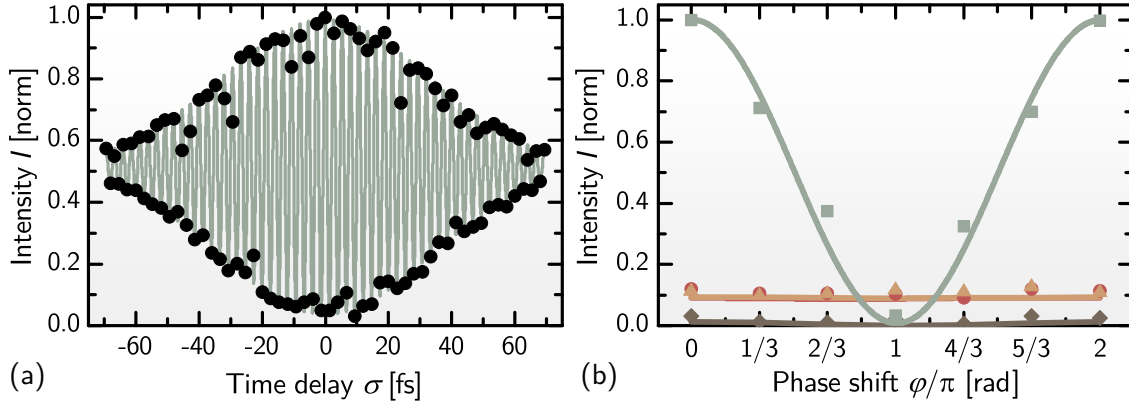
Figure 4.10: **(a)** Autocorrelation function for the experimental conditions as in Fig. 4.9: Two SPPs were exited with two fs laser pulses (Fourier-limited pulse duration 13 fs) at the lower ends of the diagonal waveguides. During the experiment, one laser pulse was fixed whereas the optical path of the second laser pulse was lengthened manually in steps of 400 nm, which corresponds to the temporal delay of 1.33 fs per step. The experimentally obtained maxima and minima of the SPP intensity in the output waveguide are shown as black dots. The theoretical autocorrelation function of the first order for gaussian pulses with an intensity FWHM of 39 fs was calculated as a green curve. **(b)** Experimental (points) and numerical simulated FDTD (lines) results of a phase sweep in steps of $\pi/3$ for the same experimental conditions as in Figs. 4.9(c,d). The green squares represent the intensity of the output waveguide. The red circles and orange triangles show the intensity in the left and right waveguides, and the olive diamonds show the intensity in the downward directed waveguide. The green, red, orange and brown lines are simulated results, respectively.

The overall losses of the SPP waveguide mode resemble $L_{\mathrm{SPP}} = 7\,\mu\mathrm{m}$. This corresponds closely to the $L_{\mathrm{SPP,free}} = 6.8\,\mu\mathrm{m}$ measured in Sect. 4.1.1 and to values in literature for this type of waveguides, e.g. $6.5\,\mu\mathrm{m}$ presented in [14].

A sweep of the time delay σ between two fs laser pulses used for the excitation of the SPPs yields dfferent intensities in the output waveguide. Every intensity maximum and minimum of a sweep over the whole pulse duration returns an intensity autocorrelation function of first order for SPPs, as described in Sect. 2.6. The resulting autocorrelation curve obtained, normalized to unity, is plotted in Fig.4.10(a) as black circles. A theoretical autocorrelation curve of the first order, corresponding to Eq. 2.12, was calculated for an assumed temporal gaussian SPP pulse with an intensity full width at half maximum (FWHM) of 39 fs. The theoretical curve was added to the experimental results as a green curve, showing a very close correspondence.

This autocorrelation proves that all measured effects are of linear nature and that non-linear processes are not involved in the switching of the output waveguides state. It should, however, be noted that the pulse duration of the autocorrelation cannot be related to the actual pulse duration, as already discussed in Sect. 2.6. Nevertheless, it is considered that the pulse duration of the excited and propagating SPPs remains ultrafast in the sub-75 fs region, since after setting the pulse delay higher than 75 fs no interference effects can be

observed.

For the region of nearly perfect temporal overlap, a more detailed investigation of the phase shift dependence of the SPP intensities in horizontal and vertical waveguides was performed. The phase φ of one excitation laser pulse was tuned in steps of $\pi/3$, whereas the phase of the other laser pulse was fixed. The experimental results of the phase variation show a clear cosine dependence of the intensity in the output waveguide, as depicted by the green squares in Fig. 4.10(b). The intensities of the left and right propagating SPPs are depicted by red circles and orange rectangles in the same figure. It can be seen that the intensity in the left and right waveguides is only dependent to a minor extent on the relative phase of the coherent SPPs in the input waveguides.

The intensity of the SPPs in the downward directed waveguide is shown by the green diamonds in Fig. 4.10(b) and it provides the lowest measured signal.

In these measurements, the background signal was subtracted in all results. The experiment was compared with a numerical FDTD simulation. The results are shown by the solid lines in Fig. 4.10(b) and correlate well with the data obtained experimentally.

Slight differences between simulated and measured intensities may be due to the finite resolution of the fabrication process, as discussed in Sect. 3.2.1. The intersections in the numerical simulations were assumed as infinitely sharp, as given by the projection mask layout.
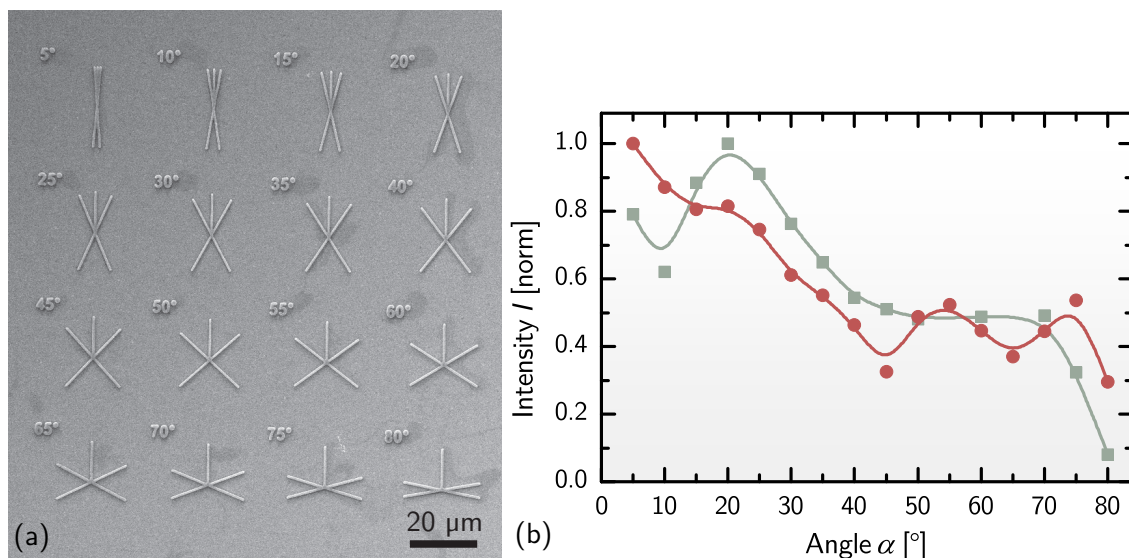
Figure 4.11: **(a)** Scanning electron microscope image of the structures used for investigations of the angle dependence between the waveguides. The diagonal waveguides are 20 µm and the vertical waveguides 10 µm long. All waveguide structures are 350 nm wide and 300 nm high. The lithographically written numbers refer to the angle between the diagonal and vertical waveguides respectively. **(b)** Comparison of numerically simulated (green squares) and experimental (red circles) results of the SPP intensities in the vertical waveguides of the structures shown in (a). The squares and circles are the measured results, whereas the lines are approximations for eye-guidance only.

Different angles between input and output waveguides

As a next step, the dependence of the output signal intensity on the angle α between input and output waveguides was investigated. New structures with two 20 µm long diagonal input waveguides and one 10 µm long vertical output waveguide, shown in Fig. 4.11, were fabricated with the MPP. The width and height of the waveguide structures were again set to 350 nm and 300 nm, respectively.

Two coherent laser pulses were focused on the lower ends of the input waveguides, while a phase difference of $0\,\pi$ was maintained between them. The SPP intensity in the output waveguide was measured. The results were again compared with numerical FDTD simulations. Both results are plotted in Fig. 4.11, indicating good correspondence between the experimental (red circles) and numerical (green squares) data. Both results were normalized to their maximum values. The obtained results clearly show that there is a strong dependence of the SPP intensity in the output waveguide on the angle between the input and output waveguides. The output signal is considerably higher in the case of smaller angles. In the simulations, a maximum of the output signal for 20° was found.

Since the basic physical phenomenon used for the switching of the intensity states is interference, it is independent of the actual intensity. The requirement of a fan-out is thus essentially determined by the technique employed to distinguish between a high and
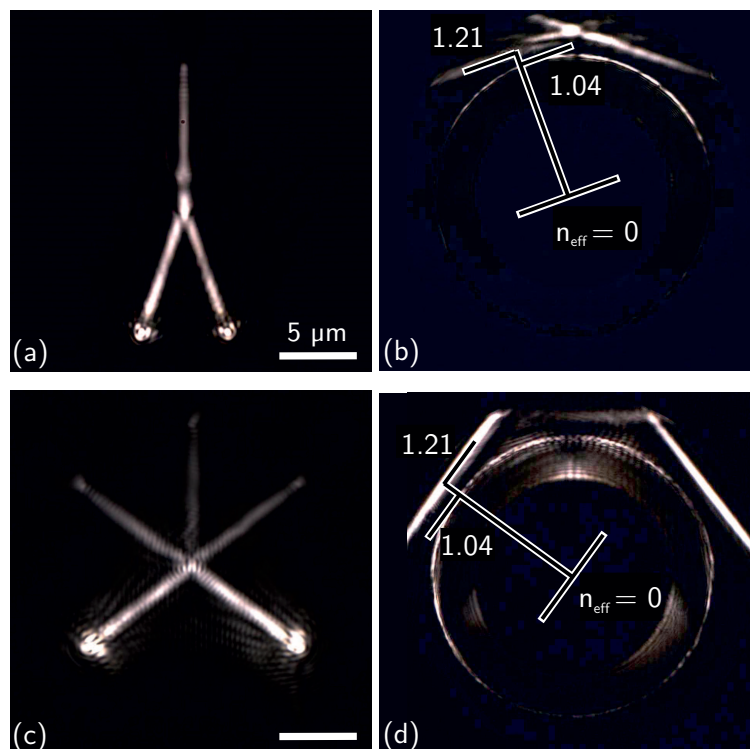
Figure 4.12: **(a,c)** Dark-field LRM images of the 20° and 55° angle structures from Fig. 4.11 with no phase difference at the inputs. **(b,d)** Corresponding images in the Fourier plane. The effective refractive index n_{eff} of the SPP mode signatures are related to the emission angle of the leakage radiation by the confined ($n_{eff} = 1.21$) and unconfined ($n_{eff} = 1.04$) SPP modes.

low state. Therefore, the optimisation of the output intensity of the crossed waveguide structures by optimizing the angle of the input waveguides adequately satisfies the demand of a fan-out.

Proof of the avoided backscattering

LRM images of the 20° and 55° structures and the corresponding Fourier transformations can be seen in Figs. 4.12(a) and 4.12(c) (image plane) and Figs. 4.12(b) and 4.12(d) (Fourier plane). It is clearly visible in the image plane (Figs. 4.12(a) and 4.12(c)), that for a 20° angle the intensity of the SPPs in the vertical output waveguide is much higher.

In the Fourier plane images shown in Figs. 4.12(b) and 4.12(d), bright circles with the effective refractive index of $n_{eff} = 1.04$ can again be seen, originating from the free propagating SPPs. Furthermore, Figs. 4.12(b) and 4.12(d) show the bright fringes with $n_{eff} = 1.21$ of the confined propagating SPP modes in the waveguide structure in the upper region. It should be noted that there is no signature of confined SPP modes in the lower region of the Fourier planes, which would have their origin in confined backward propagating SPP modes in the lower three waveguides. Thus, no signal backscattering or back-reflection in any downward direction occurs, which is one of the requirements for
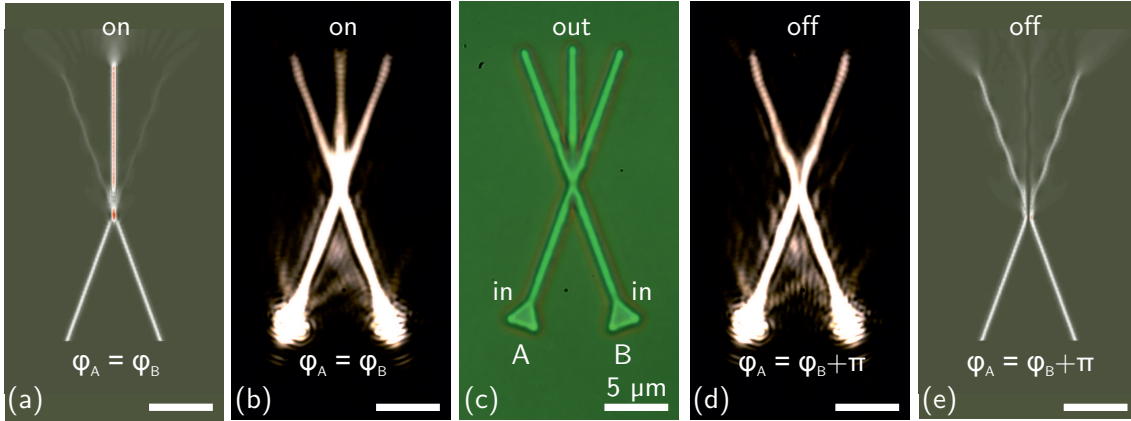
Figure 4.13: FDTD simulation **(a)**,**(e)**, dark-field LRM **(b)**,**(d)** and bright-field microscopy images**(c)** of plasmonic gate structures. The structures are made of Ormosil on a thin gold layer over a standard microscopic cover glass. The diagonal waveguides are 20 μm long. The vertical waveguide is 10 μm long. All structures are 350 nm wide and 300 nm high. The excitation laser pulses give a phase difference of $0\,\pi$ (a),(b) or $1\,\pi$ (c),(d) respectively, causing a switching of the SPP intensity in the vertical waveguide. The differences of simulated and experimental results may be due to the limited resolution of the fabrication process.

the successful operation and cascadability of logical optical elements, as discussed in the introduction of this chapter.

4.3.2 Plasmonic logic gates

Finally, the interference effect observed within the investigated structure of crossed waveguides can be considered as an ultrafast switch for SPP propagation. Furthermore, the operation of the waveguide junction shown in Fig. 4.9 already resembles a logic AND gate. Since logic gates are the building blocks of digital signal processing in electronics [26] too, and the structure already resembles a AND gate, it was chosen to use the structure as this kind of signal processing device. Since logic gates are already used in todays electronics, various cascaded systems of gates are well-known [26]. To demonstrate this cascadability, a logic half-adder will be shown in the last section of this chapter. A half-adder not only demonstrates the ability to successfully cascade these devices. As will be discussed, an optical half-adder needs one bypass waveguide, which offer an optical path length difference of $1\,\pi$. This demonstrates the very high accuracy of the fabrication approach with the MPP as well.

The extension of the crossed waveguide structures to NOT, OR, and XOR gates, as well as the mentioned AND gate operation, will be discussed in this section in detail. As a basic system, the crossed waveguide structure with an angle of $20\,°$ between the input and output waveguide (cf. Fig. 4.11(a)) was chosen. As shown in Fig. 4.13(c), the structure was extended with small tapers at the input waveguides to enhance the coupling efficiency from the laser to excited SPP modes. The excitation was performed exactly as in the
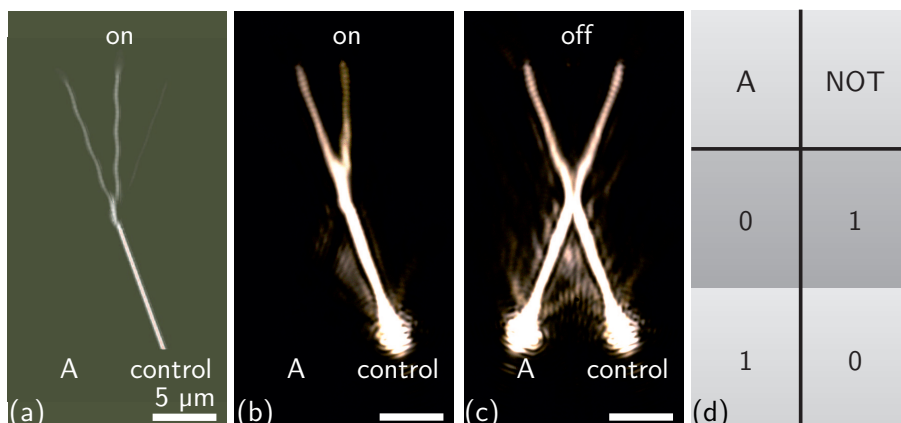
Figure 4.14: FDTD simulation of only one excitation laser pulse **(a)**. Experimental realization of a NOT gate **(b)**,**(c)** with its respective truth table **(d)**. The excitation laser pulses give a phase difference of $1\,\pi$, causing no SPP intensity in the vertical waveguide in the case of two excitation laser pulses. The differences of simulated and experimental results may be due to the limited resolution of the fabrication process.

preceding chapter. Now, the two input waveguides will be named A and B, respectively, as is indicated in 4.13(c). The upper waveguide will be again referred to as output. As before, the intensity of the output waveguide could be switched by varying the relative phase between the input waveguides, as depicted in Figs. 4.13(b,d). Thus, logic NOT, AND, OR, and XOR gate operations were achieved by adjusting this phase difference and the intensity threshold between logic *on* and *off* levels. The application of certain threshold levels is equivalent to the electronic counterparts, where only a certain voltage range is defined as *on* or *off* state of a logic element [26]. However, it should be noted that all logic gate elements were achieved with this same illustrated structure. As in the preceding chapter, numerical FDTD simulations were carried out, to compare the experimental results to theoretical expectations, as shown in Figs. 4.13(a) and 4.13(e).

Plasmonic NOT gate operation

If only one SPP mode is excited in input A, it was found, as in Sect. 4.3.1, that a part of the SPP intensity was coupled from the junction into the output waveguide, as can be seen in Figs. 4.14(a) and 4.14(b). Together with a control signal in the second input (control) waveguide this already implements a NOT gate operation, whose logic table is given in Fig. 4.14(d). The SPP state in the output waveguide can be switched from *off* to *on* state by maintaining the phase difference already discussed of $1\,\pi$ between input and control signals. The output signal remains high as long as only the control signal is present. Applying a signal to input A allows switching the output signal from *on* to *off*, as can be seen in the comparison of the Figs. 4.14(b) and 4.14(c). The intensity ratio of this two states was determined to be $8\,\mathrm{dB}$.
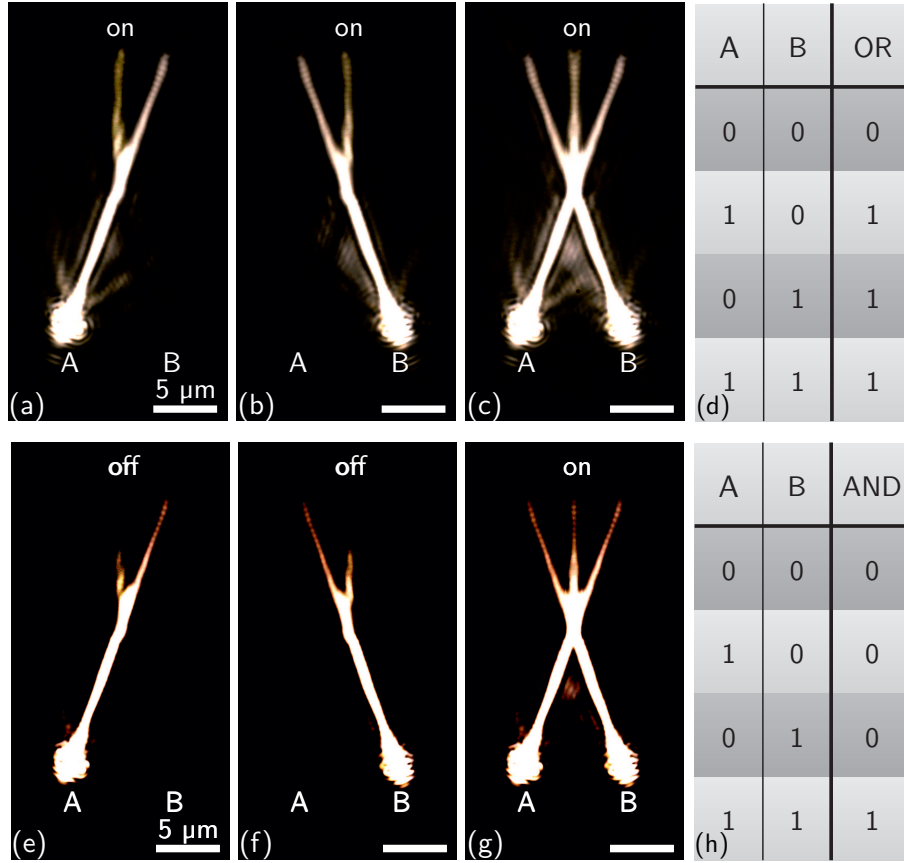
A	B	OR
0	0	0
1	0	1
0	1	1
1	1	1

A	B	AND
0	0	0
1	0	0
0	1	0
1	1	1

Figure 4.15: Experimental setup of an OR gate **(a)**-**(c)** and an AND gate **(e)**-**(g)** with the associated truth tables **(d)**,**(h)** respectively. The experimental difference between the OR and AND gates shown is only the level of the set threshold for recognition of a certain intensity as *off* state, as described in detail in Sect. 4.3.2. This difference in threshold is depicted in the use of higher camera sensitivity in the images (a)-(c), compared to the images (e)-(g). The excitation laser pulses give a phase difference of $0\,\pi$, resulting in propagating SPPs in the vertical waveguide.

Plasmonic AND and OR gate operations

The implementation of the AND and OR gate operations requires two input signals to be considered rather than one input and one control signal as in the previous case. Implementation of AND (for logic table see Fig. 4.15(h)) and OR (logic table in Fig. 4.15(d)) gates was achieved by the same interference behaviour, but with different thresholds for *on* and *off* states: in the case of one input signal, either in input A or B, a part of the SPP was coupled into the output waveguide, as is depicted in Figs. 4.15(a) and 4.15(b)). The intensity of the output waveguide was $9\,\mathrm{dB}$ higher compared to the case if no input was excited at all.

If two laser pulses with a phase difference of $0\,\pi$ were used to excite the SPP modes in the input waveguides A and B, as shown in Fig. 4.15(c), the intensity state of the output waveguide is $13\,\mathrm{dB}$ higher than in the case of no SPP excitation at both input ports.

By defining the threshold for the *on* state to be below $9\,\mathrm{dB}$, only one input signal
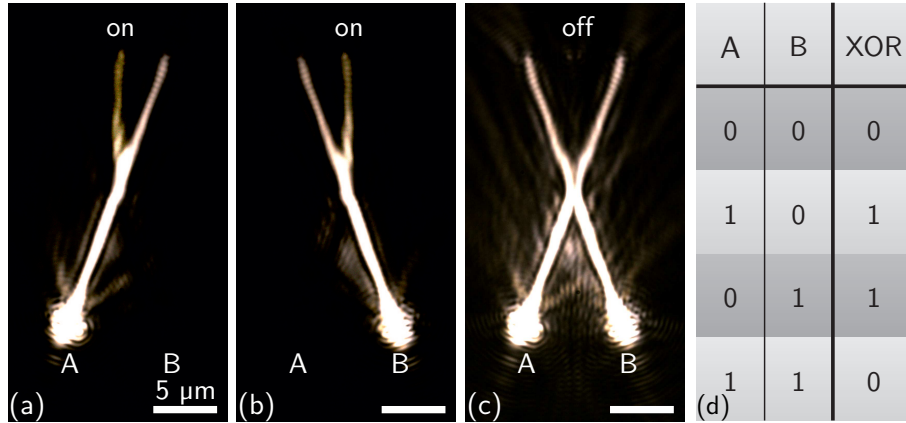
Figure 4.16: Experimental implementation of an XOR gate **(a)**-**(c)** with the associated truth table **(d)**. The excitation laser pulses give a phase difference of $1\,\pi$, causing no SPP intensity in the vertical waveguide in the case of two excitation laser pulses.

consequently results in this *on* state. And for two input signals the 13 dB output signal remains in this *on* state. This operation reveals an OR gate behaviour

If the threshold for an *on* state is now defined to be above 9 dB, it can only be reached with two excited input waveguides, leading to a 13 dB signal. One single excited input waveguide only gives a 9 dB signal, which is an *off* state by this definition. This is consistent with the truth table of an AND gate. To depict the lower threshold for AND operation, the camera sensitivity in Fig. 4.15(e)-4.15(g) was reduced, so that no output signal is visible when only one input signal is present.

Plasmonic XOR gate operation

If the phase difference between the two input signals was $1\,\pi$, as shown in Fig. 4.16(c), the intensity of the output waveguide was just about 1 dB higher in case of two excitation laser pulses compared to no input excitation at all. Thus, if the threshold for an *on* state is defined above 1 dB but below 9 dB, the truth table yields *off* for zero or two input signals respectively, and *on* only in case of one excitation laser pulse, as shown in Figs. 4.16(a)-4.16(c). This reveals an XOR gate behaviour. The logic table is shown in Fig. 4.16(d).

4.3.3 Plasmonic half-adder

As mentioned earlier, one important requirement for optical logic gates is the possibility of cascadisation of these devices [92]. This will be represented here by the combination of one AND and one XOR gate. This combination, together with a splitting element and a phase shift line, results in a half-adder [26]. The required and fabricated structure is shown in Fig. 4.17(a). The incoupling sections of the input waveguides are bent about half the intersecting angle, so that both input ports A and B point in vertical direction.

Input port A of the half-adder provided input to both gate structures via a straight

waveguide (see blue dashed line in Fig. 4.17(a)). Input port B is connected to the upper gate structure by a straight line (see orange dashed line in Fig. 4.17(a)), whereas the lower gate structure is connected with a smoothly bent delay waveguide (see red dashed line in Fig. 4.17(a)). This delay waveguide provides a longer path length than the waveguide connecting input port A with the lower gate structure (blue dashed line in Fig. 4.17(a)). In this way two SPPs, excited at the input ports, have an additional phase difference of 1π at the lower gate structure between each other. For two coherent SPPs, excited at the input ports with a phase shift of 1π, the total phase difference of the SPPs is 1π at the upper gate structure and 2π at the lower gate structure. This enables their correct operation as XOR and AND gates, respectively.

Consistent with the logic tables of the AND and XOR gates (cf. Fig. 4.15(h) and Fig. 4.16(d)), the output waveguide of the XOR gate produced *on* states when only one of the input ports A or B was excited. This output waveguide is referred to as sum (s) output. At the same time, the output port of the AND gate produced *off* states. This output waveguide is referred to as carry (c) output.

If now input ports A and B are excited simultaneously with a phase difference of 1π the XOR gate produced an *off* state in the sum output of the half-adder. However, in this case the input signals to the AND gate are both in the *on* states. Consequently the AND gate produced an *on* state in the carry output. Again it should be noted that the AND operation of this gate is assured by the presence of the delay waveguide, which has to supply a phase delay of exactly 1π, resembling an optical path length difference of exactly $\lambda/2$. Thus, the functionality of the delay waveguide depicts the very high accuracy of the microscopic projection technique used for the fabrication of the structures.

Because of the propagation losses inside the waveguides, the SPP intensities at the end of the s and c waveguides were lower compared to the single gate structures described in the preceding chapters. The signals of s and c outputs were thus measured to be 7 and 9 dB higher than the *off* state, respectively.

This structure represents a plasmonic model system for the binary addition of two one bit input signals, each to input A and input B, respectively. The *on* state of the s output provides the results for "1+0" and "0+1" operations, whereas the *on* state of the c output gives an overflow bit for the "1+1" operation.

A	B	c (AND)	s (XOR)
0	0	0	0
1	0	0	1
0	1	0	1
1	1	1	0
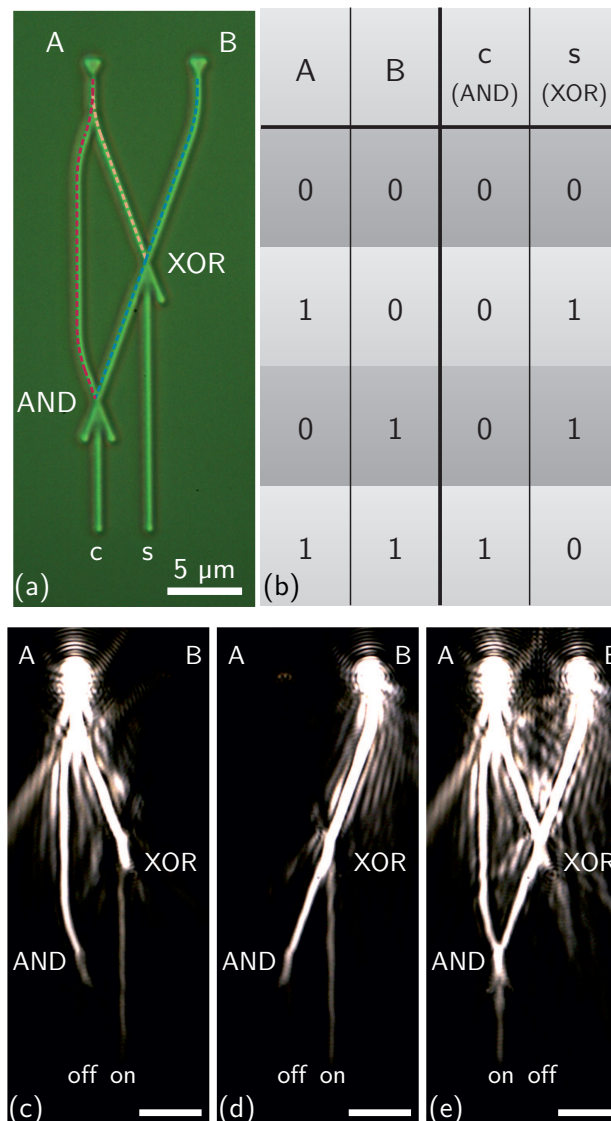
Figure 4.17: Experimental implementation of a plasmonic half-adder, generated with the combination of an XOR and an AND gate (a),(c)-(e) with the associated truth table (b). Input port B is connected with both gates by a straight waveguide (blue dashed line). Input port A is connected with the XOR gate by a straight waveguide (yellow dashed line) whereas it is connected with the AND gate by a delay waveguide (red dashed line). This delay waveguide supplies a phase shift of 1π, compared to the waveguide from the B input port to the AND gate (blue dashed line). The excitation laser pulses offer a phase difference of 1π, maintaining, in combination with the mentioned phase delay, the correct operation of both gates. This is described in detail in Sect. 4.3.3.

Summary and outlook

This thesis presented the pure optical processing of signals in dielectric plasmonic waveguides. To process the signal, logic NOT, AND, OR and XOR gate operations were employed. As structures to conduct this processing, dielectric waveguides were chosen, which are able to bind plasmonic fields to dimension below the plasmons wavelength. The functionality of the structures was investigated and furthermore the structures were successfully cascaded to a fully functional half-adder. The fabrication of all structures investigated was performed by means of a lithographic approach which was newly developed in connection with this thesis. This technique allows the fabrication of structures with resolutions below $100\,\mathrm{nm}$ with standard microscope technology. A leakage radiation microscope was used for the investigations of the surface plasmon-polaritons (SPP).

The phase of a propagating SPP mode was chosen as processed signal. In this context, two basic principles to affect the phase of propagating surface plasmon-polaritons, by means of additional thin polymer layers over of the system investigated, were presented and discussed. First for free propagating surface plasmon-polaritons on thin metal layers, and second for confined surface plasmon-polariton modes in a plasmonic counterpart to an antiresonant-reflecting optical waveguide. This waveguide offers the possibility to directly access the surface plasmon-polariton field and increase the propagation length significantly.

Additionally, the Gouy phase shift was presented as a third possibility to change the phase of surface plasmon-polaritons. This thesis thereby gives the first experimental demonstration of this phase shift in two dimensional systems for optical wavelengths. For this demonstration, the employed leakage radiation microscope was extended with an extra bypass line to enable the direct interference of the leakage radiation of the surface plasmon-polaritons with the excitation laser beam to achieve time or phase resolved measurements.

The successful processing of phase difference based signals in the dielectric waveguide structures results in a measurable signal contrast of $13/\pi\,\mathrm{dB/rad}$ in the used leakage radiation microscope. This implies a signal gain of $3\,\mathrm{dB/\mu m}$ for the antiresonant-reflecting optical waveguide experiment under consideration, if the altered guided surface plasmon-polariton mode would be processed together with an unaltered surface plasmon-polariton mode in an optical AND or OR gate. In addition, in the case of an idealized protein adlayer, a signal would be measurable in the gate output after $8.8\,\mathrm{\mu m}$ propagation length

in the antiresonant-reflecting optical waveguide.

The evaluation of the influence of free propagating surface plasmon-polaritons from an additional polymer layer over the metal revealed an increase in the effective index of the SPPs of $0.00235\,n_{\mathrm{eff}}/$nm layer thickness. This means an obtainable sensitivity of $230\,$pm layer thickness for the shift of the fringe in the Fourier plane, originating from the SPPs, of one pixel. Combined with the optical gates, a signal contrast of $1\,$dB in an AND or OR gate structure would be measured for $1.31\,$nm additional layer thickness on the metal, when the altered and unaltered SPPs each propagate $10\,\mu$m on the metal.

The Gouy phase shift would result in a signal contrast of $6.5\,$dB when processed in an AND or OR gate together with an unfocussed surface plasmon-polariton beam.

The leakage radiation microscope used to perform the measurements in this thesis, and the plasmonic systems investigated were designed to achieve the best interpretability of the results. They were not optimized to obtain the best intensity contrasts or longest propagation lengths of the surface plasmon-polaritons investigated. Additionally, the system for the optical signal processing was placed in a bulky leakage radiation microscope. So a future investigation could use smaller and more specialized lasers for the excitation of modes in the input waveguides and optical diodes to measure the intensity in the waveguides. This could not only reduce the size of the whole system but also increase the sensitivity. The use of specialized electronics however would still implement optical signal processing with electronic front and backends. Another option could therefore be to combine the optical processing directly with new concepts to excite and measure laser or surface plasmon-polariton modes directly within the waveguides as proposed in [93–95].

Time resolved leakage radiation microscope measurements could be used in the future to investigate –for example– the response of spherical nanoparticles [96,97] on the metal layer, when irradiated with surface plasmon-polaritons. Furthermore, these particles could be placed at the junction point of the crossed waveguide structures to investigate the possibility of sensing directly within the plasmonic logic gate.

Bibliography

[1] R. W. Wood, "On a remarkable case of uneven distribution of light in a diffraction grating spectrum," *Philosophical Magazine Series 6*, vol. 4, no. 21, pp. 396–402, 1902.

[2] R. W. Wood, "Diffraction gratings with controlled groove form and abnormal distribution of intensity," *Philosophical Magazine Series 6*, vol. 23, no. 134, pp. 310–317, 1912.

[3] L. Rayleigh, "On the Dynamical Theory of Gratings," *Proceedings of the Royal Society of London. Series A*, vol. 79, no. 532, pp. 399–416, 1907.

[4] U. Fano, "The theory of anomalous diffraction gratings and of quasi-stationary waves on metallic surfaces (Sommerfeld's waves)," *Journal of the Optical Society of America*, vol. 31, no. 3, pp. 213–222, 1941.

[5] A. Otto, "Excitation of nonradiative surface plasma waves in silver by the method of frustrated total reflection," *Zeitschrift für Physik*, vol. 216, no. 4, pp. 398–410, 1968.

[6] E. Kretschmann and H. Raether, "Radiative Decay of Non Radiative Surface Plasmons Excited by Light," *Zeitschrift für Naturforschung A*, vol. 23, no. 12, pp. 2135–2136, 1968.

[7] W. L. Barnes, A. Dereux, and T. W. Ebbesen, "Surface plasmon subwavelength optics," *Nature*, vol. 424, no. 6950, pp. 824–830, 2003.

[8] H. Wei, Z. Li, X. Tian, Z. Wang, F. Cong, N. Liu, S. Zhang, P. Nordlander, N. J. Halas, and H. Xu, "Quantum dot-based local field imaging reveals plasmon-based interferometric logic in silver nanowire networks," *Nano Letters*, vol. 11, no. 2, pp. 471–475, 2011.

[9] S. I. Bozhevolnyi, V. S. Volkov, E. Devaux, J.-Y. Laluet, and T. W. Ebbesen, "Channel plasmon subwavelength waveguide components including interferometers and ring resonators," *Nature*, vol. 440, no. 7083, pp. 508–511, 2006.

[10] S. I. Bozhevolnyi and J. Jung, "Scaling for gap plasmon based waveguides," *Optics express*, vol. 16, no. 4, pp. 2676–2684, 2008.

[11] E. Verhagen, J. A. Dionne, L. Kuipers, H. A. Atwater, and A. Polman, "Near-field visualization of strongly confined surface plasmon polaritons in metal- insulator- metal waveguides," *Nano letters*, vol. 8, no. 9, pp. 2925–2929, 2008.

[12] E. Verhagen, M. Spasenović, A. Polman, and L. K. Kuipers, "Nanowire plasmon excitation by adiabatic mode transformation," *Physical Review Letters*, vol. 102, no. 20, p. 203904, 2009.

[13] C. Reinhardt, R. Kiyan, A. Seidel, S. Passinger, A. L. Stepanov, A. B. Evlyukhin, and B. N. Chichkov, "Focusing and manipulation of surface plasmon polaritons by laser fabricated dielectric structures," *Plasmonics: Nanoimaging, Nanofabrication, and Their Applications III*, vol. 6642, pp. 664205–664205–11, 2007.

[14] J. Grandidier, S. Massenot, G. C. Des Francs, A. Bouhelier, J. C. Weeber, L. Markey, a. Dereux, J. Renger, M. U. González, and R. Quidant, "Dielectric-loaded surface plasmon polariton waveguides: Figures of merit and mode characterization by image and Fourier plane leakage microscopy," *Physical Review B - Condensed Matter and Materials Physics*, vol. 78, no. 24, pp. 245419–245419–9, 2008.

[15] A. Seidel, C. Reinhardt, T. Holmgaard, W. Cheng, T. Rosenzveig, K. Leosson, S. I. Bozhevolnyi, and B. N. Chichkov, "Demonstration of Laser-Fabricated DLSPPW at Telecom Wavelength," *IEEE Photonics Journal*, vol. 2, no. 4, pp. 652–658, 2010.

[16] P. Berini, R. Charbonneau, and N. Lahoud, "Long-range surface plasmons on ultrathin membranes," *Nano Letters*, vol. 7, no. 5, pp. 1376–1380, 2007.

[17] P. Berini, "Long-range surface plasmon polaritons," *Advances in Optics and Photonics*, vol. 1, no. 3, pp. 484–588, 2009.

[18] V. S. Volkov, Z. Han, M. G. Nielsen, K. Leosson, H. Keshmiri, J. Gosciniak, O. Albrektsen, and S. I. Bozhevolnyi, "Long-range dielectric-loaded surface plasmon polariton waveguides operating at telecommunication wavelengths," *Optics Letters*, vol. 36, no. 21, pp. 4278–4280, 2011.

[19] S. A. Maier, P. G. Kik, H. A. Atwater, S. Meltzer, E. Harel, B. E. Koel, and A. A. G. Requicha, "Local detection of electromagnetic energy transport below the diffraction limit in metal nanoparticle plasmon waveguides.," *Nature materials*, vol. 2, no. 4, pp. 229–232, 2003.

[20] A. B. Evlyukhin and S. I. Bozhevolnyi, "Surface plasmon polariton guiding by chains of nanoparticles," *Laser Physics Letters*, vol. 3, no. 8, pp. 396–400, 2006.

[21] A. B. Evlyukhin, C. Reinhardt, E. Evlyukhina, and B. N. Chichkov, "Asymmetric and symmetric local surface-plasmon-polariton excitation on chains of nanoparticles.," *Optics letters*, vol. 34, no. 14, pp. 2237–2239, 2009.

[22] D. Van Orden, Y. Fainman, and V. Lomakin, "Optical waves on nanoparticle chains coupled with surfaces," *Optics letters*, vol. 34, no. 4, pp. 422–424, 2009.

[23] S. I. Bozhevolnyi, J. Erland, K. Leosson, P. M. W. Skovgaard, and J. M. Hvan, "Waveguiding in surface plasmon polariton band gap structures," *Physical Review Letters*, vol. 86, no. 14, pp. 3008–3011, 2001.

[24] T. Søndergaard and S. I. Bozhevolnyi, "Vectorial model for multiple scattering by surface nanoparticles via surface polariton-to-polariton interactions," *Physical Review B*, vol. 67, no. 16, pp. 165405–165405–8, 2003.

[25] A. Markov, C. Reinhardt, B. Ung, A. B. Evlyukhin, W. Cheng, B. N. Chichkov, and M. Skorobogatiy, "Photonic bandgap plasmonic waveguides.," *Optics letters*, vol. 36, no. 13, pp. 2468–2470, 2011.

[26] T. Schenk and U. Tietze, *Halbleiterschaltungstechnik*, vol. 12. Springer, 1993.

[27] S.-K. Kwong, G. A. Rakuljic, and A. Yariv, "Real time image subtraction and exclusive or operation using a self-pumped phase conjugate mirror," *Applied physics letters*, vol. 48, pp. 201–203, 1986.

[28] Y. Fainman, C. C. Guest, and S. H. Lee, "Optical digital logic operations by two-beam coupling in photorefractive material.," *Applied optics*, vol. 25, no. 10, pp. 1598–1603, 1986.

[29] M. Ogusu, S.-I. Tanaka, and K. Kuroda, "Optical logic operations using three-beam phase-conjugate interferometry," *Japanese Journal of Applied Physics*, vol. 29, no. 7, pp. L1265–L1267, 1990.

[30] V. Almeida, C. Barrios, R. Panepucci, and M. Lipson, "All-optical control of light on a silicon chip," *Nature*, vol. 431, no. 7012, pp. 1081–1084, 2004.

[31] Y. Zhang, Y. Zhang, and B. Li, "Optical switches and logic gates based on self-collimated beams in two-dimensional photonic crystals.," *Optics express*, vol. 15, no. 15, pp. 9287–9292, 2007.

[32] Q. Xu and M. Lipson, "All-optical logic based on silicon micro-ring resonators," *Optics express*, vol. 15, no. 3, pp. 924–929, 2007.

[33] J. Zhang, K. F. MacDonald, and N. I. Zheludev, "Controlling light-with-light without nonlinearity," *Light: Science & Applications*, vol. 1, no. 7, p. e18, 2012.

[34] X. Fang, M. L. Tseng, J. Y. Ou, K. F. Macdonald, D. P. Tsai, and N. I. Zheludev, "Ultrafast all-optical switching via coherent modulation of metamaterial absorption," *Applied Physics Letters*, vol. 104, no. 14, pp. 141102–141102–4, 2014.

[35] X. Fang, K. F. MacDonald, and N. I. Zheludev, "Controlling light with light using coherent metadevices: all-optical transistor, summator and invertor," *Light: Science & Applications*, vol. 4, no. 5, p. e292, 2015.

[36] D. Tsiokos, E. Kehayas, K. Vyrsokinos, T. Houbavlis, L. Stampoulidis, G. T. Kanellos, N. Pleros, G. Guekos, and H. Avramopoulos, "10-Gb/s All-Optical Half-Adder With Interferometric," *IEEE Photonics Technology Letters*, vol. 16, no. 1, pp. 284–286, 2004.

[37] S. C. Xavier, K. Arunachalam, E. Caroline, and W. Johnson, "Design of two-dimensional photonic crystal-based all-optical binary adder," *Optical Engineering*, vol. 52, no. 2, pp. 025201–025201–6, 2013.

[38] P. Phongsanam and S. Mitatha, "All-Optical Adder / Substractor using Dark-Bright Soliton Conversion Control," in *2012 9th International Conference on Electrical Engineering/Electronics, Computer, Telecommunications and Information Technology*, pp. 1–4, 2012.

[39] M. Nady, K. F. A. Hussein, and A.-E.-H. A. Ammar, "Ultrafast All-Optical Full Adder Using Quantum-Dot Semiconductor Optical Amplifier-Based Mach-Zehnder Interferometer," *Progress In Electromagnetics Research B*, vol. 54, pp. 69–88, 2013.

[40] S. Kaur, R.-S. Kaler, and T.-S. Kamal, "All-Optical Binary Full Adder Using Logic Operations Based on the Nonlinear Properties of a Semiconductor Optical Amplifier," *Journal of the Optical Society in Korea*, vol. 19, no. 3, pp. 222–227, 2015.

[41] H. Wei, Z. Wang, X. Tian, M. Käll, and H. Xu, "Cascaded logic gates in nanophotonic plasmon networks," *Nature communications*, vol. 2, no. 387, pp. 1–5, 2011.

[42] H. Raether, *Surface plasmons on smooth surfaces*. Springer, 1988.

[43] A. Drezet, A. Hohenau, D. Koller, A. Stepanov, H. Ditlbacher, B. Steinberger, F. R. Aussenegg, A. Leitner, and J. R. Krenn, "Leakage radiation microscopy of surface plasmon polaritons," *Materials Science and Engineering B*, vol. 149, no. 3, pp. 220–229, 2008.

[44] A. Hohenau, J. R. Krenn, A. Drezet, O. Mollet, S. Huant, C. Genet, B. Stein, and T. W. Ebbesen, "Surface plasmon leakage radiation microscopy at the diffraction limit," *Optics Express*, vol. 19, no. 25, pp. 25749–25762, 2011.

[45] A. D. Rakic, A. B. Djurisic, J. M. Elazar, and M. L. Majewski, "Optical properties of metallic films for vertical-cavity optoelectronic devices.," *Applied Optics*, vol. 37, no. 22, pp. 5271–5283, 1998.

[46] P. B. Johnson and R. W. Christy, "Optical Constants of the Noble Metals," *Physical Review B*, vol. 6, no. 12, pp. 4370–4379, 1972.

[47] S. Babar and J. H. Weaver, "Optical constants of Cu, Ag, and Au revisited," *Applied Optics*, vol. 54, no. 3, pp. 477–481, 2015.

[48] C. J. Powell, "Analysis of Optical-and Inelastic-Electron-Scattering Data. II. Application to Al," *JOSA*, vol. 60, no. 1, pp. 78–93, 1970.

[49] E. Le Ru and P. Etchegoin, *Principles of surface enhanced Raman spectroscopy.* Elsevier B.V., 2009.

[50] H. Ehrenreich and H. R. Philipp, "Optical properties of Ag and Cu," *Physical Review*, vol. 128, no. 4, p. 1622, 1962.

[51] H. Ehrenreich, H. R. Philipp, and B. Segall, "Optical properties of aluminum," *Physical Review*, vol. 132, no. 5, p. 1918, 1963.

[52] E. Kretschmann, "Die Bestimmung optischer Konstanten von Metallen durch Anregung von Oberflächenplasmaschwingungen," *Zeitschrift für Physik*, vol. 241, no. 4, pp. 313–324, 1971.

[53] M. C. Troparevsky, A. S. Sabau, A. R. Lupini, and Z. Zhang, "Transfer-matrix formalism for the calculation of optical response in multilayer systems: from coherent to incoherent interference.," *Optics express*, vol. 18, no. 24, pp. 24715–24721, 2010.

[54] L. G. Gouy, "Sur une propriété nouvelle des ondes lumineuses," *Comptes Rendus des Seances de L'Académie des Sciences*, vol. 1, pp. 1251–1253, 1890.

[55] L. G. Gouy, "Sur la propagation anomale des ondes," *Ann. Chim. Phys*, vol. 24, pp. 145–213, 1891.

[56] R. Kiyan, C. Reinhardt, S. Passinger, A. L. Stepanov, A. Hohenau, J. R. Krenn, and B. N. Chichkov, "Rapid prototyping of optical components for surface plasmon polaritons," *Optics Express*, vol. 15, no. 7, pp. 4205–4215, 2007.

[57] A. B. Evlyukhin, S. I. Bozhevolnyi, A. L. Stepanov, R. Kiyan, C. Reinhardt, S. Passinger, and B. N. Chichkov, "Focusing and directing of surface plasmon polaritons by curved chains of nanoparticles.," *Optics express*, vol. 15, no. 25, pp. 16667–16680, 2007.

[58] H. G. Kraus, "Huygens–Fresnel–Kirchhoff wave-front diffraction formulation: paraxial and exact Gaussian laser beams," *Journal of the Optical Society of America A*, vol. 7, no. 1, pp. 47–65, 1990.

[59] S. Feng and H. G. Winful, "Physical origin of the Gouy phase shift.," *Optics letters*, vol. 26, no. 8, pp. 485–487, 2001.

[60] G. Merziger and T. Wirth, *Repetitorium der höheren Mathematik.* Hannover: Binomi, 2006.

[61] J.-C. Diels and W. Rudolph, *Ultrashort laser pulse phenomena.* Academic press, 2006.

[62] Y. Gorodetski, T. Chervy, S. Wang, J. A. Hutchison, A. Drezet, C. Genet, and T. W. Ebbesen, "Tracking surface plasmon pulses using ultrafast leakage imaging," *Optica*, vol. 3, no. 1, pp. 48–53, 2016.

[63] D. Marcuse, *Theory of dielectric optical waveguides.* Academic Press, 1974.

[64] B. E. A. Saleh and M. C. Teich, *Fundamentals of Photonics.* Wiley, 2006.

[65] M. A. Duguay, Y. Kokubun, T. L. Koch, and L. Pfeiffer, "Antiresonant reflecting optical waveguides in SiO2-Si multilayer structures," *Applied Physics Letters*, vol. 49, no. 1, pp. 13–15, 1986.

[66] H. A. Jamid and M. N. Akram, "Analysis of antiresonant reflecting optical waveguide gratings by use of the Method of Lines," *Applied Optics*, vol. 42, no. 18, pp. 3488–3494, 2003.

[67] C. Reinhardt, A. B. Evlyukhin, W. Cheng, T. Birr, A. Markov, B. Ung, M. Skorobogatiy, and B. N. Chichkov, "Bandgap-confined large-mode waveguides for surface plasmon-polaritons," *Journal of the Optical Society of America B*, vol. 30, no. 11, pp. 2898–2905, 2013.

[68] T. Holmgaard and S. I. Bozhevolnyi, "Theoretical analysis of dielectric-loaded surface plasmon-polariton waveguides," *Physical Review B*, vol. 75, no. 24, pp. 245405–245405–12, 2007.

[69] M. N. O. Sadiku, *Numerical Techniques in Electromagnetics with MATLAB, Third Edition.* 2009.

[70] C. Lemke, C. Schneider, T. Leißner, D. Bayer, J. W. Radke, A. Fischer, P. Melchior, A. B. Evlyukhin, B. N. Chichkov, and C. Reinhardt, "Spatiotemporal characterization of SPP pulse propagation in two-dimensional plasmonic focusing devices," *Nano letters*, vol. 13, no. 3, pp. 1053–1058, 2013.

[71] C. Lemke, T. Leißner, A. Evlyukhin, J. Radke, A. Klick, J. Fiutowski, J. Kjelstrup-Hansen, H.-G. Rubahn, B. N. Chichkov, and C. Reinhardt, "The interplay between localized and propagating plasmonic excitations tracked in space and time," *Nano letters*, vol. 14, no. 5, pp. 2431–2435, 2014.

[72] A. Taflove and S. C. Hagness, *Computational electrodynamics.* Artech house, 2005.

[73] G. Boole, *The mathematical analysis of logic.* Philosophical Library, 1847.

[74] D. B. Hall, P. Underhill, and J. M. Torkelson, "Spin Coating of Thin and Ultrathin Polymer Films," *Polymer Engineering and Science*, vol. 38, no. 12, pp. 2039–2045, 1998.

[75] A. A. Tracton, *Coatings technology handbook.* CRC press, 2005.

[76] R. Srivastava and B. C. Yadav, "Nanolithography: Processing Methods for Nanofabrication Development," *Imperial Journal of Interdisciplinary Research*, no. 6, pp. 275–284, 2016.

[77] B. D. Gates, Q. Xu, M. Stewart, D. Ryan, C. G. Willson, and G. M. Whitesides, "New Approaches to Nanofabrication: Molding, Printing, and Other Techniques," *Chemical Reviews*, vol. 105, no. 4, pp. 1171–1196, 2005.

[78] L. Pavesi and D. J. Lockwood, *Silicon Photonics III: Systems and Applications.* 2016.

[79] A. Pimpin and W. Srituravanich, "Reviews on micro- and nanolithography techniques and their applications," *Engineering Journal*, vol. 16, no. 1, pp. 37–55, 2012.

[80] H. Kawata, J. M. Carter, A. Yen, and H. I. Smith, "Optical projection lithography using lenses with numerical apertures greater than unity," *Microelectronic Engineering*, vol. 9, no. 1-4, pp. 31–36, 1989.

[81] J. C. Love, D. B. Wolfe, H. O. Jacobs, and G. M. Whitesides, "Microscope projection photolithography for rapid prototyping of masters with micron-scale features for use in soft lithography," *Langmuir*, vol. 17, no. 19, pp. 6005–6012, 2001.

[82] D. Malacara-Hernández and Z. Malacara-Hernández, *Handbook of optical design.* CRC Press, 2016.

[83] A. Ovsianikov, J. Viertl, B. Chichkov, M. Oubaha, B. MacCraith, I. Sakellari, A. Giakoumaki, D. Gray, M. Vamvakaki, M. Farsari, and C. Fotakis, "Ultra-low shrinkage hybrid photosensitive material for two-photon polymerization microfabrication," *ACS Nano*, vol. 2, no. 11, pp. 2257–2262, 2008.

[84] C. Reinhardt, R. Kiyan, S. Passinger, a. L. Stepanov, a. Ostendorf, and B. N. Chichkov, "Rapid laser prototyping of plasmonic components," *Applied Physics A*, vol. 89, no. 2, pp. 321–325, 2007.

[85] C. Reinhardt, A. Seidel, A. B. Evlyukhin, W. Cheng, and B. N. Chichkov, "Mode-selective excitation of laser-written dielectric-loaded surface plasmon polariton waveguides," *Journal of the Optical Society of America B*, vol. 26, no. 12, pp. B55–B60, 2009.

[86] C. Reinhardt, A. Seidel, A. Evlyukhin, W. Cheng, R. Kiyan, and B. Chichkov, "Direct laser-writing of dielectric-loaded surface plasmon-polariton waveguides for the visible and near infrared," *Applied Physics A*, vol. 100, no. 2, pp. 347–352, 2010.

[87] N. Sardana, T. Birr, S. Schlenker, C. Reinhardt, and J. Schilling, "Surface plasmons on ordered and bi-continuous spongy nanoporous gold," *New Journal of Physics*, vol. 16, no. 6, pp. 063053–063053–11, 2014.

[88] X. Cai, H. P. Langtangen, and H. Moe, "On the performance of the Python programming language for serial and parallel scientific computations," *Scientific Programming*, vol. 13, no. 1, pp. 31–56, 2005.

[89] J. C. Chaves, J. Nehrbass, B. Guilfoos, J. Gardiner, S. Ahalt, A. Krishnamurthy, J. Unpingco, A. Chalker, A. Warnock, and S. Samsi, "Octave and python: High-level scripting languages productivity and performance evaluation," in *HPCMP Users Group Conference, 2006*, pp. 429–434, IEEE, 2006.

[90] U. S. Inan and R. A. Marshall, *Numerical Electromagnetics: The FDTD Method.* Cambridge: Cambirdge University Press, 2011.

[91] A. Kolomenski, A. Kolomenskii, J. Noel, S. Peng, and H. Schuessler, "Propagation length of surface plasmons in a metal film with roughness.," *Applied optics*, vol. 48, no. 30, pp. 5683–5691, 2009.

[92] D. A. B. Miller, "Are optical transistors the logical next step?," *Nature Photonics*, vol. 4, no. 1, pp. 3–5, 2010.

[93] P. Bollgruen, U. Gleissner, T. Wolfer, C. Megnin, D. Mager, L. Overmeyer, J. G. Korvink, and T. Hanemann, "Ink-jet printed fluorescent materials as light sources for planar optical waveguides on polymer foils," *Optical Engineering*, vol. 55, no. 10, p. 107107, 2016.

[94] Y. Wang and L. Overmeyer, "Chip-Level Packaging of Edge-Emitting Laser Diodes onto Low-Cost Transparent Polymer Substrates Using Optodic Bonding," *IEEE Transactions on Components, Packaging and Manufacturing Technology*, vol. 6, no. 5, pp. 667–674, 2016.

[95] S. Döring, T. Otto, M. Cehovski, O. Charfi, R. Caspary, W. Kowalsky, and T. Rabe, "Highly sensitive wide range organic photodiode based on zinc phthalocyanine: C60," *physica status solidi (a)*, vol. 213, no. 9, pp. 2387–2391, 2016.

[96] U. Zywietz, C. Reinhardt, A. B. Evlyukhin, T. Birr, and B. N. Chichkov, "Generation and patterning of Si nanoparticles by femtosecond laser pulses," *Applied Physics A*, vol. 114, no. 1, pp. 45–50, 2014.

[97] U. Zywietz, A. B. Evlyukhin, C. Reinhardt, and B. N. Chichkov, "Laser printing of silicon nanoparticles with resonant optical electric and magnetic responses.," *Nature communications*, vol. 5, no. 3402, pp. 1–7, 2014.

Appendix

A.1 Maple code for the transfer matrix method

$n_0 := 1 :$

$n_1 := \mathrm{sqrt}\left(\dfrac{1}{2} \cdot \left(\mathrm{sqrt}(er^2 + eim^2) + er\right)\right) + I \cdot \mathrm{sqrt}\left(\dfrac{1}{2} \cdot \left(\mathrm{sqrt}(er^2 + eim^2) - er\right)\right)$

$$\dfrac{1}{2}\sqrt{2\sqrt{er^2+eim^2}+2\,er} + \dfrac{1}{2}\,I\sqrt{2\sqrt{er^2+eim^2}-2\,er} \tag{1}$$

$er := -12.01 :$

$eim := 0.475 :$

$n_2 := 1.46 :$

$k0 := \dfrac{2 \cdot \mathrm{Pi}}{\mathrm{lambda}} :$

$\mathrm{lambda} := 0.5461 :$

$with(LinearAlgebra) :$

$U(i, j, \mathrm{theta}) := \dfrac{1}{t(i, j, \mathrm{theta})} \cdot Matrix([\,[\,1, r(i, j, \mathrm{theta})\,], [\,r(i, j, \mathrm{theta}), 1\,]\,])$

$$(i, j, \theta) \to \dfrac{Matrix([\,[\,1, r(i, j, \theta)\,], [\,r(i, j, \theta), 1\,]\,])}{t(i, j, \theta)} \tag{2}$$

$U(i, j, \mathrm{theta})$

$$\begin{bmatrix} \dfrac{1}{t(i,j,\theta)} & \dfrac{r(i,j,\theta)}{t(i,j,\theta)} \\[2ex] \dfrac{r(i,j,\theta)}{t(i,j,\theta)} & \dfrac{1}{t(i,j,\theta)} \end{bmatrix} \tag{3}$$

$t(i, j, \mathrm{theta}) := \dfrac{2 \cdot n_i \cdot n_j \cdot kx(i, \mathrm{theta})}{n_j^2 \cdot kx(i, \mathrm{theta}) + n_i^2 \cdot kx(j, \mathrm{theta})}$

$$(i, j, \theta) \to \dfrac{2\,n_i\,n_j\,kx(i, \theta)}{n_j^2\,kx(i, \theta) + n_i^2\,kx(j, \theta)} \tag{4}$$

$r(i, j, \mathrm{theta}) := \dfrac{n_j^2 \cdot kx(i, \mathrm{theta}) - n_i^2 \cdot kx(j, \mathrm{theta})}{n_j^2 \cdot kx(i, \mathrm{theta}) + n_i^2 \cdot kx(j, \mathrm{theta})}$

$$(i, j, \theta) \to \dfrac{n_j^2\,kx(i, \theta) - n_i^2\,kx(j, \theta)}{n_j^2\,kx(i, \theta) + n_i^2\,kx(j, \theta)} \tag{5}$$

$kx(i, \mathrm{theta}) := \mathrm{sqrt}\left(k0^2 \cdot n_i^2 - kz(\mathrm{theta})^2\right)$

$$(i, \theta) \to \sqrt{k0^2\,n_i^2 - kz(\theta)^2} \tag{6}$$

$kz(\mathrm{theta}) := n_2 \cdot k0 \cdot \sin\left(\dfrac{\mathrm{theta} \cdot \mathrm{Pi}}{180}\right)$

$$\theta \to n_2\,k0\,\sin\left(\dfrac{1}{180}\,\theta\,\pi\right) \tag{7}$$

$P(i, \mathrm{theta}, d) := Matrix([\,[\exp(-I \cdot \mathrm{phi}(i, \mathrm{theta}, d)), 0], [0, \exp(I \cdot \mathrm{phi}(i, \mathrm{theta}, d))]\,])$

$$(i, \theta, d) \rightarrow Matrix\left(\left[\left[e^{-I\phi(i, \theta, d)}, 0\right], \left[0, e^{I\phi(i, \theta, d)}\right]\right]\right) \tag{8}$$

$phi(i, \text{theta}, d) := kx(i, \text{theta}) \cdot d$
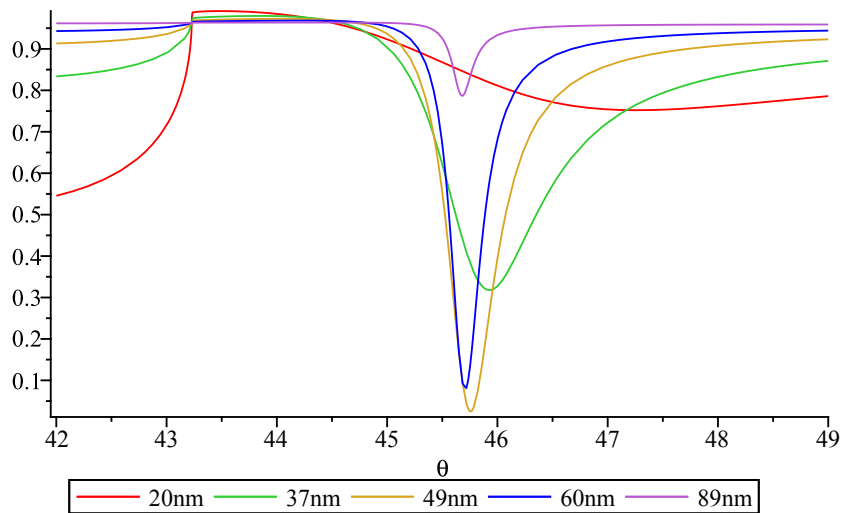
$$(i, \theta, d) \rightarrow kx(i, \theta)\, d \tag{9}$$

$M(\text{theta}, d) := Multiply(\, U(2, 1, \text{theta}), Multiply(P(1, \text{theta}, d), U(1, 0, \text{theta})))$

$$(\theta, d) \rightarrow LinearAlgebra\text{:-}Multiply\big(\, U(2, 1, \theta), LinearAlgebra\text{:-}Multiply(P(1, \theta, d), U(1, 0, \theta)))\big) \tag{10}$$

$R(\text{theta}, d) := \left| \dfrac{M(\text{theta}, d)_{2, 1}}{M(\text{theta}, d)_{1, 1}} \right|^2$

$$(\theta, d) \rightarrow \left| \dfrac{M(\theta, d)_{2, 1}}{M(\theta, d)_{1, 1}} \right|^2 \tag{11}$$

$plot(\,[\,R(\text{theta}, 0.0200), R(\text{theta}, 0.0370), R(\text{theta}, 0.0490), R(\text{theta}, 0.0600), R(\text{theta}, 0.089)\,], \text{theta} = 42\,..49\,)$

A.2 Expression of complex values with Euler's formula

In general, Euler's formula represents complex values $z = a + \mathrm{i}\,b$ as a point in the complex plane with its radius $|z| = \sqrt{a^2 + b^2}$ and angle $\varphi = \arctan{(b/a)}$ by $z = |z|\exp{(\mathrm{i}\arctan{(b/a)})}$.

To put

$$f(z)_{\mathrm{3D}} = \frac{1}{1 - \mathrm{i}\frac{z}{z_{\mathrm{R}}}}$$

into the form of $a + \mathrm{i}\,b$, it can simply be extended to

$$\frac{1\left(1 + \frac{\mathrm{i}\,z}{z_{\mathrm{R}}}\right)}{\left(1 - \frac{\mathrm{i}\,z}{z_{\mathrm{R}}}\right)\left(1 + \frac{\mathrm{i}\,z}{z_{\mathrm{R}}}\right)}.$$

Multiplication results in

$$\frac{1 + \frac{\mathrm{i}\,z}{z_{\mathrm{R}}}}{1 + \left(\frac{z}{z_{\mathrm{R}}}\right)^2},$$

with $a = 1/(1 + (z/z_{\mathrm{R}})^2)$ and $b = (z/z_{\mathrm{R}})/(1 + (z/z_{\mathrm{R}})^2)$. Thus

$$\arctan\left(\frac{b}{a}\right) = \arctan\left(\frac{\frac{\frac{z}{z_{\mathrm{R}}}}{1 + \left(\frac{z}{z_{\mathrm{R}}}\right)^2}}{\frac{1}{1 + \left(\frac{z}{z_{\mathrm{R}}}\right)^2}}\right)$$

$$= \arctan\left(\frac{z}{z_{\mathrm{R}}}\right)$$

and

$$\sqrt{a^2 + b^2} = \sqrt{\left(\frac{1}{1 + \left(\frac{z}{z_{\mathrm{R}}}\right)^2}\right)^2 + \left(\frac{\frac{z}{z_{\mathrm{R}}}}{1 + \left(\frac{z}{z_{\mathrm{R}}}\right)^2}\right)^2}$$

$$= \sqrt{\left(1 + \left(\frac{z}{z_{\mathrm{R}}}\right)^2\right)\frac{1}{\left(1 + \left(\frac{z}{z_{\mathrm{R}}}\right)^2\right)^2}}$$

$$= \frac{1}{\sqrt{1 + \left(\frac{z}{z_{\mathrm{R}}}\right)^2}}.$$

This gives Euler's formula

$$f(z)_{\mathrm{3D}} = \frac{1}{1 - \frac{\mathrm{i}\,z}{z_{\mathrm{R}}}} = \frac{1}{\sqrt{1 + \left(\frac{z}{z_R}\right)^2}}\exp\left(\mathrm{i}\arctan\left(\frac{z}{z_{\mathrm{R}}}\right)\right)$$

A.3 Stock prices of microscope objectives in October 2016

A.3.1 Zeiss 100 x Oil immersion 1.4 NA

Carl Zeiss Microscopy GmbH, Deutschland > Objektiv-Assistent > Liste der Objekt... Seite 1 von 2

ZEISS

We make it visible.

Impressum | Datenschutz | Geschäftsbedingungen | Carl Zeiss | Carl Zeiss International

Mikroskopie & Imaging | Online-Shop   Carl Zeiss Microscopy GmbH, Deutschland

Startseite   Warenkorb   Mein Konto   Kontakt   Partner   Community

Benutzer
> Tobias Birr
Benutzer-ID: DE17177

> Einkaufslisten: 0
> Online-Bestellungen: 0
Preise zzgl. MwSt.
Abmelden

Anwendungen
> Bio-Med. Anwendungen
> Materialanwendungen
Mikroskope
> Aufrechte Mikroskope
> Inverse Mikroskope
> Stereomikroskope
> Zoom-Mikroskope
> Digitalmikroskope
Computer
> Computer
Software
> AxioVision Software
> ZEN Software
Zubehör
> Zubehör
Werkzeuge
> Kamera-Assistent
> Filter-Assistent
■ Objektiv-Assistent

Suchen

Carl Zeiss Microscopy GmbH
Königsallee 9-21
37081 Göttingen
Deutschland

info.microscopy.de@zeiss.com
0180 333 6 334 (Festnetz 12
Cent/Min.; Mobil max. 42 Cent/Min.)

Besuchen Sie uns auf:
Facebook
Twitter
YouTube

Die Lieferung erfolgt frei Haus.
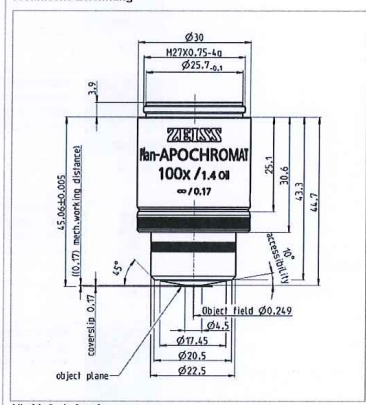
© 2006-2016 Carl Zeiss

Objektiv-Assistent
→ English

→ Objektiv-Assistent → Liste der Objektive   Drucken

Objektiv-Daten

Broschüre: Objektive von Carl Zeiss (5 MB)

Objektivklasse: Plan-Apochromat SF25
Beste Ebnung, beste Korrektur, konfokale Mikroskopie

Objektiv Plan-Apochromat 100x/1,4 Oil M27
420790-9901-000
in Warenkorb

→ Transmissionskurve

Objektiv Plan-Apochromat 100x/1,4 Oil M27
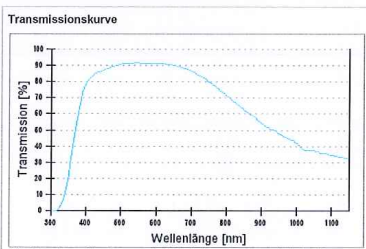Es ist leider kein Produktfoto vorhanden.

Objektiv Plan-Apochromat 100x/1,4 Oil M27 (a=0,17mm), inkl. Immersol 518 F, Öler 20ml und Deckgläser, hoch präzise, D=0,17mm, Schachtel mit 100 Stück

Preis	€ 4 767,00
Maßstabszahl	100x
Numerische Apertur	1,4
Arbeitsabstand [mm]	0,17
Deckglasdicke [mm]	0,17
Gewindetyp	M27x0,75
Immersion	Öl
Sehfeld [mm]	25
Abgleichlänge [mm]	45,06
Großer Arbeitsabstand (LD)	
Korrektionsring (Corr)	
Iris (Iris)	
Optisches System	Infinity Color Corrected System (ICS)
Ebnung	★★★★★
Farbkorrektur	★★★★★
Biomedizinische Anwendungen	
Fluoreszenz	■
- Multichannel	★★★★★
- Ultraviolett-Transmission	★★★
- Infrarot-Transmission	★★★★
Hellfeld (B)	■
Differentieller Interferenzkontrast (DIC)	
High Contrast DIC (HC DIC)	
PlasDIC-Kontrast	
Phasenkontrast (PH)	
VAREL-Kontrast	
Hoffman Modulation Contrast (HMC)	
Polarisationskontrast (POL)	
Material- (Auflicht) Anwendungen	
Hellfeld (B)	
Hellfeld/Dunkelfeld (BD)	
Auflicht-DIC (RL DIC)	
High Contrast DIC (HC DIC)	
DIC mit zirkular-polarisiertem Licht (C-DIC)	
Totalinterferenz-Kontrast (TIC)	
Polarisationskontrast (POL)	
Optionen	
Definite Focus.2	★★★
Konfokale Mikroskopie	■
- Ultraviolet	★★★
- VIS (sichtbares Licht)	★★★★★
NLO-IR / 2 Photon	★★

Technische Zeichnung

ZEISS Plan-APOCHROMAT 100x / 1.4 Oil ∞ / 0.17

Alle Maße in [mm]

Transmissionskurve

Transmission [%] — Wellenlänge [nm]

Bitte beachten Sie, dass es sich hierbei um durchschnittliche Werte handelt. Auf Grund von Produktionstoleranzen kann es zu Abweichungen bis zu ca. 5% kommen.

Carl Zeiss Microscopy GmbH, Deutschland > Objektiv-Assistent > Liste der Objekt... Seite 2 von 2

Total Internal Reflection Fluorescence (TIRF)	
ApoTome	■
Mikrodissektion	

Passendes Zubehör für
420790-9901-000 Objektiv Plan-Apochromat 100x/1,4 Oil M27

Den Inhalt des Warenkorbs können Sie:
+ online bestellen
+ als Fax-Bestellung drucken
+ als schriftliches Angebot anfordern
+ als Einkaufsliste speichern

Sonstiges Zubehör

Objektivring ACR für Objektivhülse zylindrisch kurz
Artikelnummer: 424508-0000-000
Objektivring ACR für Objektivhülse zylindrisch kurz

€ 79,00 | Kompatibilität | in Warenkorb

Immersionsmittel

Immersionsöl Immersol 518 F fluoreszenzfrei, Flasche 100 ml
Artikelnummer: 444962-0000-000
Immersionsöl Immersol 518 F fluoreszenzfrei, Flasche 100 ml (ISO 8036-1/2, ne=1,518 (23°C), halogenfrei)

€ 174,00 | Kompatibilität | in Warenkorb

Immersionsöl Immersol 518 F fluoreszenzfrei, Flasche 250 ml
Artikelnummer: 444963-0000-000
Immersionsöl Immersol 518 F fluoreszenzfrei, Flasche 250 ml (ISO 8036-1/2, ne=1,518 (23°C), halogenfrei)

€ 349,00 | Kompatibilität | in Warenkorb

Immersionsöl Immersol 518 F fluoreszenzfrei, Flasche 500 ml
Artikelnummer: 444964-0000-000
Immersionsöl Immersol 518 F fluoreszenzfrei, Flasche 500 ml (ISO 8036-1/2, ne=1,518 (23°C), halogenfrei)

€ 623,00 | Kompatibilität | in Warenkorb

Immersionsöl Immersol 518 F fluoreszenzfrei, Öler 20 ml
Artikelnummer: 444960-0000-000
Immersionsöl Immersol 518 F fluoreszenzfrei, Öler 20 ml (ISO 8036-1/2, ne=1,518 (23°C), halogenfrei)

€ 44,00 | Kompatibilität | in Warenkorb

Reinigungspapier (300 Blatt)
Artikelnummer: 462975-0000-000
Reinigungspapier (300 Blatt)

€ 34,00 | Kompatibilität | in Warenkorb

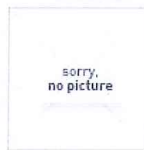## A.3.2   Müller Optronics 100 x Oil immersion 1.25 NA

Objektiv 100x E-Plan / unendlich / NA 1.25 / 0.17 ÖL | Plan Achrom. Objektive | O...   Seite 1 von 2

Diese Seite benötigt Cookies. Sind Sie mit der Nutzung von Cookies einverstanden?   Ja

Nein

< Übersicht | Plan Achrom. Objektive

Objektiv 100x E-Plan / unendlich / NA 1.25 / 0.17 ÖL

sorry,
no picture

119,95 € *

inkl. MwSt. zzgl. Versandkosten

Sofort versandfertig, Lieferzeit ca. 1-3 Werktage

| 1 | ∨ | | In den Warenkorb | > |

♥ Merken

Artikel-Nr.:   30004056

Beschreibung

Produktinformationen "Objektiv 100x E-Plan / unendlich / NA 1.25 / 0.17 ÖL"

Weiterführende Links zu "Objektiv 100x E-Plan / unendlich / NA 1.25 / 0.17 ÖL"

> Fragen zum Artikel?
> Weitere Artikel von Mueller

Kunden haben sich ebenfalls angesehen   +

Objektiv 100x E-Plan / unendlich / NA 1.25 / 0.17 ÖL | Plan Achrom. Objektive | O...   Seite 2 von 2

sorry, no picture	sorry, no picture	sorry, no picture	sorry, no picture
Objektiv 60x E-Plan /	Objektiv 100x Plan /	Objektiv 40x E-Plan /	MNC-01 Vergleichsmikrc
99,95 € *	109,95 € *	89,95 € *	3.699,00 € *

Zuletzt angesehen

sorry, no picture	sorry, no picture
Objektiv 100x E-Plan / unendlich /	Objektiv 60x E-Plan / unendlich /

* Alle Preise inkl. gesetzl. Mehrwertsteuer zzgl. Versandkosten und ggf. Nachnahmegebühren, wenn nicht anders beschrieben

Müller
Germany

https://www.mueller-optronic.com/de/mikroskop-zubehoer/objektive/plan-achrom.-ob...   19.10.2016

Liste der Publikationen

Im Rahmen dieser Arbeit entstandene Publikationen:

Geprüfte Publikationen als Erstautor

- <u>T. Birr</u>, U. Zywietz, P. Chhantyal, B. N. Chichkov, and C. Reinhardt, "Ultrafast surface plasmon-polariton logic gates and half-adder," *Optics Express*, vol. 23, no. 25, pp. 31755–31765, 2015.

- <u>T. Birr</u>, U. Zywietz, T. Fischer, P. Chhantyal, A. B. Evlyukhin, B. N. Chichkov, and C. Reinhardt, "Ultrafast surface plasmon-polariton interference and switching in multiple crossing dielectric waveguides," *Applied Physics B*, vol. 122, no. 6, p. 164, 2016.

- <u>T.Birr</u>, T. Fischer, A. B. Evlyukhin, U. Zywietz, B. N. Chichkov, and C. Reinhardt, "Phase-Resolved Observation of the Gouy Phase Shift of Surface Plasmon Polaritons," *ACS Photonics*, vol. 4, no. 4, pp. 905–908, 2017.

Geprüfte Publikationen als Koautor

- C. Reinhardt, A. B. Evlyukhin, W. Cheng, <u>T. Birr</u>, A. Markov, B. Ung, M. Skorobogatiy, and B. N. Chichkov, "Bandgap-confined large-mode waveguides for surface plasmon-polaritons," *Journal of the Optical Society of America B*, vol. 30, no. 11, pp. 2898–2905, 2013.

- U. Zywietz, C. Reinhardt, A. B. Evlyukhin, <u>T. Birr</u>, and B. N. Chichkov, "Generation and patterning of Si nanoparticles by femtosecond laser pulses," *Applied Physics A*, vol. 114, no. 1, pp. 45–50, 2014.

- N. Sardana, <u>T. Birr</u>, S. Schlenker, C. Reinhardt, and J. Schilling, "Surface plasmons on ordered and bi-continuous spongy nanoporous gold," *New Journal of Physics*, vol. 16, no. 6, p. 63053, 2014.

Buchkapitel

- C. Reinhardt, V. F. Paz, L. Zheng, K. Kurselis, <u>T. Birr</u>, U. Zywietz, B. Chichkov, K. Frenner, and W. Osten, "Design and fabrication of near- to far-field transformers by sub-100 nm two-photon polymerization," in Optically Induced Nanostructures: Biomedical and Technical Applications, K. König and A. Ostendorf, Eds. Walter de Gruyter GmbH & Co KG, 2015, pp. 73–92.

Auszeichnungen

- "Posterpreis des NanoDay 2015 vom Laboratorium für Nano- und Quantenengineering Hannover" für das Poster "*Ultrafast Surface Plasmon-Polariton Logic Gates and Half-Adder*"

Curriculum vitae

Persönliche Daten

NAME	Tobias Birr
ANSCHRIFT	Mettlerkampsweg 18
	20535 Hamburg
GEBURTSDATUM	10.10.1986
NATIONALITÄT	Deutsch

Schulbildung

2006	Abitur, Wirtschaftsgymnasium Gropiusring in Hamburg

Universitätsausbildung

10/2007 − 09/2010	Universität Hamburg
	Bachelorstudium in Physik
	Bachelorprüfung am 24.09.2010
04/2010 − 09/2010	Bachelorarbeit mit dem Titel "Im Templat synthetisierte
	magnetische Nanokapseln"
	Universität Hamburg, Institut für Angewandte Physik
10/2010 − 09/2012	Leibniz Universität Hannover
	Masterstudium in Technischer Physik
	Masterprüfung am 26.09.2010
10/2011 − 08/2012	Masterarbeit mit dem Titel "Goldnanopartikel induzierte
	Laserperforation/ -transfektion"
	Laser Zentrum Hannover e.V.
11/2012 − 03/2017	Leibniz Universität Hannover
	Promotionsstudent in Physik
	Promotion mit dem Titel "Investigation of plasmonic structures
	for use as sensors and signal processing devices"
	Laser Zentrum Hannover e.V.

Berufserfahrung

11/2012 − 10/2016	Wissenschaftlicher Mitarbeiter am Laser Zentrum Hannover e. V.

Danksagung

An dieser Stelle möchte ich mich bei all denjenigen bedanken, die wesentlich zum Gelingen dieser Arbeit beigetragen haben:

- Ich danke Prof. Priv.-Doz. Dr. Carsten Reinhardt für die hervorragende Betreuung und Unterstützung, und die unzähligen gewinnbringenden Gespräche und Reflexionen über den Verlauf und den Fortschritt dieser Arbeit.

- Ich danke Prof. Dr. Boris N. Chichkov für die ebenfalls hervorragende Betreuung, für die unzähligen Motivationen, und für seine geduldigen Versuche die Sackgassen frühzeitig zu erkennen und den Fokus dieser Arbeit auf das Wesentliche zu lenken.

- Natürlich danke ich auch Urs Zywietz. Ohne die erfrischenden Gespräche (sowohl wissenschaftlicher als auch nicht-wissenschaftlicher Natur) mit ihm, ohne die gemeinsamen Arbeiten im Labor und ohne das gemeinschaftliche Entwickeln der MPP wäre diese Arbeit nicht realisierbar gewesen.

- Ich danke meinem Schwiegervater Paul Crocker für das Übernehmen des Lektorats dieser Arbeit. Ohne ihn wären viele Worte und ganze Sätze in dieser Arbeit ohne Sinn geblieben.

- Ich danke Tim Fischer und Dr. Andrey B. Evlyukhin für die unbeirrbare Unterstützung im Verständnis der theoretischen Beschreibung der beschriebenen Phänomene in dieser Arbeit.

- Ich danke Parva Chhantyal, Lei Zheng, Ayman El-Tamer, Kestutis Kurselis, Dr. Roman Kyian und Dr. Ulf Hinze für die unzähligen Male an Unterstützung und kollegialen Gesprächen im Verlauf dieser Arbeit.

- Darin eingeschlossen danke ich sowohl allen oben Genannten, als auch allen anderen Kolleg*Innen in der NT, dem LZH, der HSN und bei PlanOS für die unglaublich gute Arbeitsatmosphäre in meiner Zeit in Hannover.

- Neben der Arbeit danke ich meiner Familie, meinen Freunden, und den Leuten bei Dreisechzehn – Stadtkirche Hannover und Serve the City Hannover für den sinnvollen und wohltuenden Ausgleich.

Zuletzt danke ich über allem stehend meiner Ehefrau Esther Birr. Ich danke ihr für die vorbehaltlose Liebe, für den Rückhalt und für die Motivation die ich durch sie erfahren habe.